J. Mech. Phys. Solids 215 (2026) 106697

Contents lists available at ScienceDirect

Journal of the Mechanics and Physics of Solids

journal homepage: www.elsevier.com/locate/jmps

Nonreciprocal transition waves in active lattices

Yao Zhang [a,b], Chengxuan Zhai [a,b], Zhanfeng Li [c], Jiahao Li [d], Guangjin Mou [e], Lizichen Chen [f], Yangkun Du [f], Michel Destrade [g], Changguo Wang [a,b,*], Yafei Wang [a,b,*]

[a] National Key Laboratory of Science and Technology on Advanced Composites in Special Environments, Harbin Institute of Technology, Harbin, 150001, China
[b] Center for Composite Materials and Structures, Harbin Institute of Technology, Harbin, 150001, China
[c] School of Civil Engineering and Transportation, South China University of Technology, Guangzhou, 510641, China
[d] Department of Modern Mechanics, University of Science and Technology of China, Hefei, 230027, China
[e] Department of Civil and Environmental Engineering, The Hong Kong University of Science and Technology, 999077, Hong Kong, China
[f] State Key Laboratory of Fluid Power and Mechatronic Systems and Department of Engineering Mechanics, Zhejiang University, Hangzhou, 310027, China
[g] School of Mathematical and Statistical Science, University of Galway, University Road, Galway, Ireland

A R T I C L E I N F O

Keywords:
Nonreciprocal transition waves
Mechanical metamaterials
Self-resetting active bistable lattices
Fast-slow dynamics
Singular perturbation analysis
Nonreciprocal energy transmission

A B S T R A C T

Active systems, such as contraction of muscle fibers and action potential propagation in neural networks, exhibit efficient directional transport of information and energy. Bringing these biological principles into engineered systems can overcome the limitations of passive metamaterials in tunability after fabrication, spontaneous reset, and the realization of dynamical nonreciprocity. However, a unified and transparent analytical framework for reversible nonreciprocal wave propagation governed by coupled fast-slow dynamics remains absent. We develop a mechanical lattice composed of active bistable elements incorporating a displacement-driven slow recovery variable to emulate biologically inspired recovery processes and capture the evolution of active stiffness. Discrete and continuum models are derived to describe the lattice dynamics. Building on continuum descriptions, we employ singular perturbation and matched asymptotic expansions, complemented by machine learning, to enable analytical characterization. Then we define a metric of nonreciprocal energy transport and map the key parameters to quantify how system parameters jointly control wave speed and propagation direction. Nonlinear results reveal that forward and backward transition waves propagate at markedly different steady speeds, demonstrating pronounced nonreciprocity. The key mechanism arises from the coupling between fast excitation and slow recovery, which produces a refractory effect that resets the energy landscape and therefore breaks time reversal symmetry in a geometrically symmetric structure. During the evolution of active stiffness, an intermediate phase emerges and co-propagates with the mechanical wave and selectively suppresses returning waves under appropriate timing conditions. Consequently, reversible and tunable nonreciprocal transition waves are achieved. We obtain bidirectional wave solutions, along with analytical expressions for wave speed, width and energy flux as well as their conditions of validity. Theoretical predictions agree closely with numerical simulations and

* Corresponding authors.
E-mail addresses: wangcg@hit.edu.cn (C. Wang), yafeiwang@hit.edu.cn (Y. Wang).

https://doi.org/10.1016/j.jmps.2026.106697
Received 24 March 2026; Received in revised form 18 May 2026; Accepted 30 May 2026
Available online 1 June 2026

demonstrate that the nonreciprocity depends on the recovery rate in a nonlinear manner. This study provides a general theoretical framework and practical design guidelines for bioinspired intelligent metamaterials that enable reversible directional energy routing, signal isolation, and mechanical logic, and it also informs the design of field controlled phase change materials and multiphysics devices.

1. Introduction

Understanding how ordered structures and spatiotemporal patterns emerge in complex systems remains a central scientific challenge (Greilich et al., 2025; Tian and Gong, 2025; Zhou and Wang, 2024; Zhang et al., 2024). In contrast to linear media that obey the principle of superposition, many systems can host energy in highly localized, particle like packets that propagate without change of shape. These self-sustained wave packets are termed solitary waves, and those with elastic scattering are classified as solitons (Zhang and Rudykh, 2024; Ziv and Shmuel, 2020; Silling, 2016; Yasuda et al., 2019; Gao et al., 2024). Among the many families of solitons, transition waves, i.e., elastic topological solitons, represent a canonical class distinguished by their role as smooth transition structures between two spatial regions associated with inequivalent degenerate ground states. Since their discovery, solitons have attracted sustained attention across physics, mathematics, and mechanics. From the KdV equation describing shallow water waves to constitutive models for biological tissues, soliton theory offers a unified mathematical framework spanning scales from molecular motion to macroscopic biomechanics (Zhou and Wang, 2023; Tang et al., 2024; Zhang et al., 2023). The hallmarks of solitons are their resilience to dispersion during propagation and their persistence of shape after collisions. Transition waves (elastic topological solitons) interpolate continuously between different states, creating a robust interface whose existence and stability stem from the topology of the underlying potential landscape. This inherent topological protection makes them promising carriers of information and energy in mechanical settings (Zhang et al., 2019; Zhou and Wang, 2023).

Bistability, characterized by two stable equilibria separated by an energy barrier, provides a broad physical and mechanical basis for the emergence of transition waves. Transition waves in bistable media therefore propagate as traveling elastic topological solitons with distinctive dynamics. These concepts have been applied to model and interpret a range of biophysical processes (see Fig. 1(a)-(c)), including muscle fiber contraction (Caruel et al., 2015; Caruel and Truskinovsky, 2017; Givli and Bhattacharya, 2009), cytoskeletal remodeling (Bernitt et al., 2017; Pierre, 2020), and nerve impulse propagation. Rapid advances in mechanical metamaterials have created new opportunities for studying transition waves through architected control of macroscopic response. Guided by geometric nonlinearity, researchers have realized bistable building blocks based on buckled beams, shear units, and origami inspired modules. When arranged into one-, two- or three-dimensional lattices, these assemblies display strong nonlinear behavior and can store and release substantial elastic energy (Choi et al., 2025; Zhang et al., 2025; Li et al., 2025a; Liu et al., 2019, 2023; Roller et al., 2024; Tang et al., 2025; Wang et al., 2024a; Xiu et al., 2025; Zhou et al., 2022).

In passive bistable media, the propagation of transition waves has been investigated in depth. A canonical model treats the architecture as rigid masses coupled by nonlinear springs whose force-displacement relation is nonmonotonic. When the system resides in a high energy metastable configuration, a local disturbance can trigger the first unit to switch to the low energy state. The released potential energy is transmitted to neighboring units through coupling, initiating a self-sustained front. This front propagates at an approximately constant speed and progressively converts the structure to the low energy configuration (Deng et al., 2020, 2025; Jin et al., 2020; Nadkarni et al., 2016a; Pal and Sitti, 2023; Raney et al., 2016; Zareei et al., 2020). Theoretical descriptions introduce a traveling wave ansatz that reduces governing partial differential or discrete difference equations to ordinary differential equations. This reduction enables analytical or semi-analytical expressions for the wave speed and profile. (Comte et al., 1999; Deng et al., 2020; Nadkarni et al., 2014; Remoissenet and Peyrard, 1984; Slepyan et al., 2005; Vasios et al., 2021). Experiments with carefully designed specimens have provided strong validation of these predictions. Such studies deepen the understanding of nonlinear lattice dynamics and inform the development of functional materials and devices, including high efficiency impact energy absorbers, passive mechanical logic elements, and acoustic diodes. Despite substantial progress, passive bistable media exhibit intrinsic limitations. The chief constraint is the unidirectional irreversibility and narrow functionality of wave propagation. Because energy release follows the second law of thermodynamics, once a wave has traversed the structure, the system relaxes to a low energy ground state and loses functional activity. Restoring functionality typically requires external mechanical resetting of the entire structure or selected regions. This requirement is impractical for applications that demand rapid and repeated responses (Nadkarni et al., 2014). A further limitation is that key response characteristics, such as wave speed and energy dissipation rate, are fixed by material and geometric parameters after fabrication. These properties cannot be adjusted during operation (Raney et al., 2016). These limitations motivate the exploration of approaches that introduce active control, so that the energy can be injected in a programmable and timely manner, thereby endowing the system with dynamically reconfigurable behavior.

Active matter consists of dynamic assemblies of units that continuously consume energy and sustain nonequilibrium states, often converting environmental energy into mechanical motion or other forms of ordered behavior (Binysh et al., 2022; Da Rocha et al., 2022; Kulkarni, 2023; Wang et al., 2024c). In the field of bio-inspired engineering, researchers have introduced active mechanisms into bistable metamaterials, establishing the field of active bistable systems (Wu et al., 2024; Zhang and Rudykh, 2024; Zhou et al., 2022). A defining feature is the ability to modulate the energy wells through external stimuli. Examples include molecular motors powered by ATP hydrolysis, light-induced protein conformational changes, or chemical energy driving shape memory materials. Real time tunability overcomes the constraints of passive platforms and enables reversible propagation of phase transition waves. By regulating energy input with precision, the structure can switch between two stable states in a controlled manner, imparting

Nomenclature

$i = 1, \dots, N$	Mass index in the discrete lattice.
N	Number of masses (sites) in the lattice.
x_i	Reference position of site i in the lattice.
a	Lattice spacing (distance between adjacent sites).
L_{sys}	Total lattice length.
t	Time variable.
z	Traveling-wave coordinate.
$H(\cdot)$	Heaviside step function.
$\dot{(\cdot)}$	First partial derivative with respect to time t (overdot notation).
$(\cdot)'$	Derivative with respect to the traveling coordinate z.
$\mathcal{O}(\cdot)$	Landau order notation in asymptotics.
$u_i(t)$	Displacement of site i.
$s_i(t)$	Active stiffness (slow recovery variable) at site i.
$\nabla_d(\cdot)$	Discrete forward difference operator.
$\Delta_d(\cdot)$	Discrete Laplacian (second difference).
u^L, u^M, u^R	Left/right stable states and the unstable saddle of the on-site potential.
m	Mass of each site.
k	Nearest-neighbor spring stiffness.
η	Linear viscous damping coefficient.
A_0, A_1	Passive stiffness parameters of the on-site element.
B_0, B_1	Target values controlling the active stiffness level.
L	Half distance between the two stable displacements ($2L$ total span).
δ	Potential-shape parameter governing well asymmetry/curvature.
ξ	Recovery rate of the active stiffness.
ε	Small parameter marking fast-slow time-scale separation.
$\mathcal{U}_i(u_i; s_i)$	On-site potential energy at site i.
$f_i(u_i; s_i)$	On-site restoring force (derivative of the on-site potential).
$\mathscr{L}$	Lagrangian of the discrete lattice.
T	Kinetic energy.
V_{spr}	Nearest-neighbor spring interaction energy.
V_{on}	On-site bistable potential energy.
$\mathscr{R}$	Rayleigh dissipation functional.
$\Delta\mathcal{U}$	Energy gap between right and left minima at a site.
E_k	Kinetic energy density transported at the wave front.
x	Spatial coordinate in the continuum model.
$u(x,t)$	Continuum displacement field.
$s(x,t)$	Continuum active-stiffness field (slow recovery variable).
$(\cdot)_x$	First partial derivative with respect to x.
$\rho = m/a$	Linear mass density.
$k' = ka$	Continuum spring modulus.
$\eta' = \eta/a$	Continuum viscous coefficient.
X, T, U, S	Characteristic length, time, displacement, and stiffness scales.
$\bar{x}, \bar{t}, \bar{u}, \bar{s}$	Nondimensional coordinate, time, displacement, and active stiffness.
$\bar{A}_0, \bar{A}_1$	Nondimensional passive stiffness parameters.
$\bar{B}_0, \bar{B}_1$	Nondimensional active-stiffness targets.
$\zeta = T\xi$	Dimensionless recovery rate of the active stiffness.
$\bar{L}_{sys}$	Nondimensional domain length.
$\bar{c}_f, \bar{c}_b$	Nondimensional forward and backward wave speeds.
$\bar{c}_f^0$, $\lvert\bar{c}_b^0\rvert$	Leading-order (asymptotic) forward/backward speeds.
λ_f, λ_b	Inverse widths of forward and backward fronts.
λ_f^0, λ_b^0	Leading-order inverse widths from asymptotic analysis.
Θ_f, Φ_f	Auxiliary combinations in forward speed selection formulas.
Θ_b, Φ_b	Auxiliary combinations in backward speed selection formulas.
R	Length of the initially excited region used to launch a front.
N_{rel}	Nonreciprocity metric based on wave speeds.
N_{width}	Nonreciprocity metric based on wave widths.
$\Delta\bar{E}$	Nonreciprocal energy-transport difference (nondimensional).

bioinspired adaptability and intelligent responses (Roh et al., 2025; Song et al., 2025; Worrell et al., 2018). This strategy opens avenues for next generation smart materials with potential in micro and nanorobotics, adaptive structures, and biomedical engineering.

The sarcomere in muscle is a typical example of the active bistable structure (see Fig. 1(a)-(c)) (Caruel et al., 2015). At the onset of sarcomere contraction, active elements consume energy to generate the primary driving force. As the deformation increases, the passive force rises while the active force decreases. This interplay enables a bistable mechanism governed by the combined action of active and passive forces throughout the process. Such systems are widespread in nature, from molecular motors and ciliary arrays to collective cell migration, and they exhibit distinctive nonequilibrium dynamics (Gerwien et al., 2019). The introduction of activity also introduces significant dynamical complexity. Accurate modeling requires multivariable coupling that augments mechanical displacement with additional variables representing active processes, such as active stress or active stiffness (Li et al., 2025b; Sun et al., 2025; Xing et al., 2024; Zhang and Rudykh, 2025). The resulting governing equations are strongly nonlinear. A prominent characteristic is the separation of time scales. Because mechanical displacement and unit flipping occur on a fast scale that can reach the millisecond range, whereas the evolution of active variables and the remodeling of the energy landscape proceed on a slow scale determined by the rate of the energy injection (Angeli et al., 2004; Göktepe et al., 2014). This coupling of fast and slow dynamics creates deep analogies with biological excitable media. The FitzHugh-Nagumo model, which combines a fast membrane potential with a slow gating variable to capture action potential generation and the refractory period, serves as a useful conceptual template. An active bistable lattice can be viewed as a mechanical counterpart of this excitable recoverable dynamics (FitzHugh, 1955, 1961). The complex behavior arises from strong nonlinear interactions between fast and slow variables, yielding rich dynamical regimes and posing significant challenges for theoretical analysis. This analogy offers a fresh perspective on the mechanics of living systems and guides the design of new classes of intelligent materials.

The intrinsic coupling introduced by a slow recovery variable furnishes a new physical paradigm for realizing nonreciprocal wave propagation. Nonreciprocity denotes wave behavior that differs for forward and backward transmission and it underpins advanced platforms for multi-directional asymmetric information flow and directional energy transport (Wang et al., 2025; Shaat and Park, 2023; Tang et al., 2024). Conventional passive metamaterials primarily exploit carefully designed structural asymmetry to break spatial inversion symmetry, thereby realizing a static, geometry-dependent form of nonreciprocity. In contrast, active metamaterials enable a dynamic form of nonreciprocity that arises from the breaking of time-reversal symmetry. This behavior is fundamentally rooted in nonlinear interactions between fast and slow dynamical processes (Li et al., 2018, 2020; Librandi et al., 2021; Nassar et al., 2020). When a forward traveling front sweeps the medium, it triggers a rapid mechanical response and simultaneously drives an associated slow variable away from equilibrium. As this slow variable relaxes over a finite time, a nonequilibrium region forms in the wake that retains a memory of recent activity. A backward-propagating wave initiated during this relaxation stage encounters a medium reshaped by the evolving energy landscape rather than its initial state. This history dependent interaction leads to a pronounced difference between backward and forward propagation speeds, even when the geometric layout is perfectly symmetric (Wang et al., 2024d; Tang et al., 2024).

This intrinsic arrow of time, established by the recovery dynamics of the slow variable, is conceptually analogous to the directional control of contraction-relaxation signal transmission in sarcomeres. In muscle fiber contraction, a refractory period governed by ion-channel gating ensures robust unidirectional propagation of contraction and relaxation signals along the muscle fibers, respectively (Beck et al., 2008; Rubin and Wechselberger, 2008). The proposed dynamic mechanism provides a mechanical realization of this biological principle. Most importantly, it frees nonreciprocal function from dependence on complex static geometry and enables real time in situ programmability. Control over the kinetics of the slow recovery variable allows continuous tuning of both the magnitude and the direction of nonreciprocity, opening a path to reconfigurable and environment-responsive intelligent nonreciprocal devices.

Existing theories in mechanics and materials struggle to unify activity, reversibility, nonreciprocity, and coupling between fast and slow dynamics. For an active bistable lattice described by a two-variable coupled framework, the propagation of reversible nonreciprocal transition waves still lacks analytical clarity. Here, we introduce a slow recovery variable, governed by a recovery law with a time constant that describes the recovery process, where the displacement determines the target stiffness. This law is isomorphic to muscle activation dynamics in biomechanics and encodes a memory wake and a transiently inexcitable zone that modulate macroscopic transport direction. Building on this framework, we construct a lattice of masses connected by linear springs, with each mass anchored through passive and active bistable elements in parallel. By employing singular perturbation analysis to address the multiscale nonlinearity induced by fast-slow coupling, we derive bidirectional wave solutions, obtain analytical expressions for wave speed, width, and their domains of validity, and ultimately couple these solutions with a machine learning model. The results quantify how speed depends on passive and active stiffness parameters as well as on dimensionless recovery rate of active stiffness. A quantitative metric for nonreciprocal energy transport is established, demonstrating that even in geometrically symmetric media, reversible and tunable directional energy routing and signal isolation can be achieved by adjusting the timescale and coupling strength of the slow recovery variable. The theory provides explicit design principles and parameter maps for bioinspired active metamaterials.

The paper is organized as follows. Section 2 introduces the mathematical model of the active bistable lattice, specifies the form of its energy and the self-resetting mechanism. Section 3 numerically solves the discrete model to visualize reversible and nonreciprocal transition waves, revealing an intermediate phase during the evolution of active stiffness. Section 4 develops the continuum governing equations and enables nonreciprocal transition waves with adjustable return positions and the capability of multiple propagations. Section 5 employs singular perturbation analysis to derive traveling wave solutions in both directions, coupled with machine learning. Section 6 investigate nonreciprocal energy transmission and the influence of key parameters. The final section concludes the study and discusses potential applications in active metamaterials.

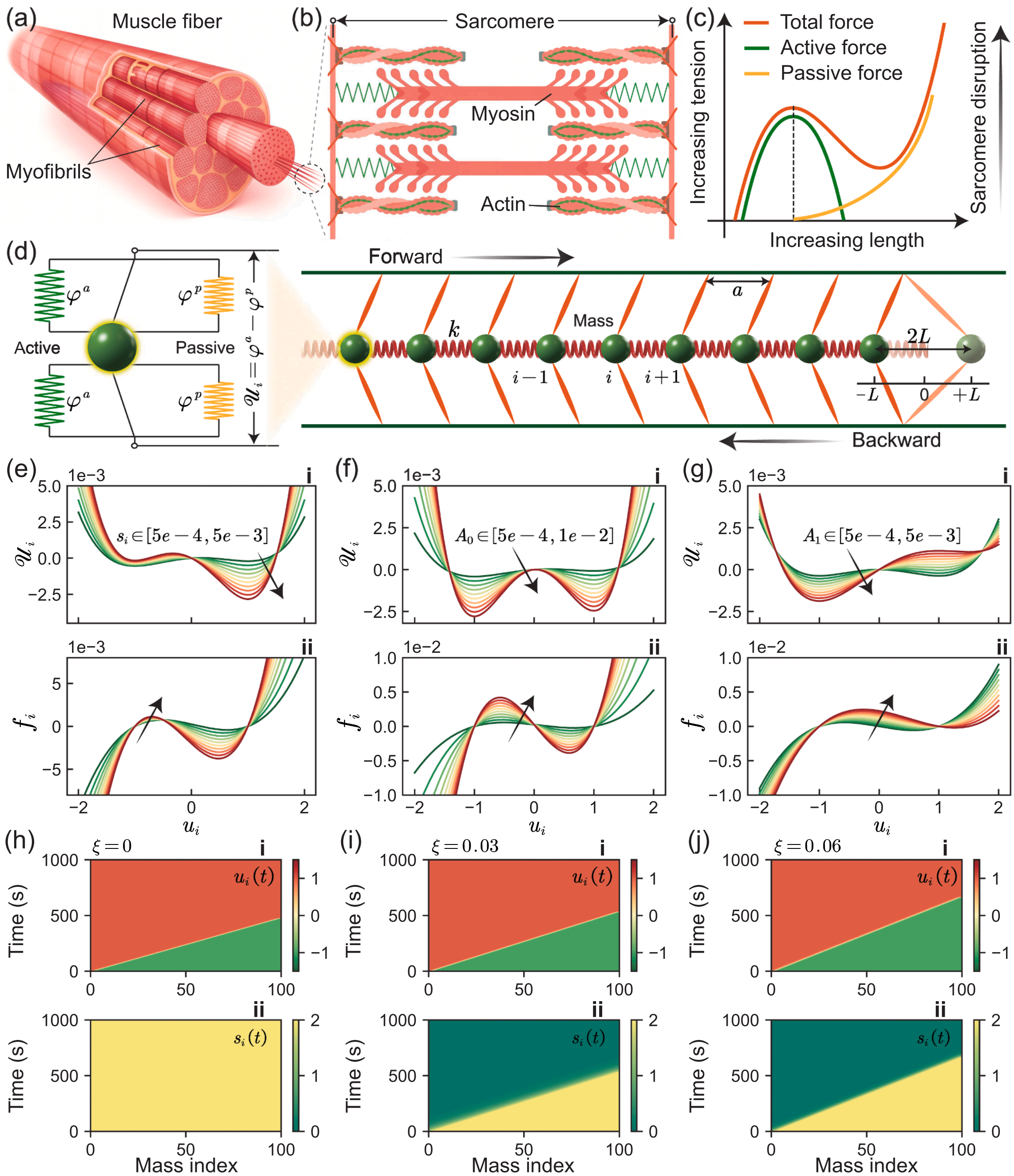

Fig. 1. The active self-resetting bistable lattice with tunable energy landscape capable of propagating transition waves, inspired by sarcomere dynamics. (a) Schematic of a muscle fiber composed of myofibrils. (b) Myofibrillar structure showing periodic arrangement of actin and myosin filaments regulated by biological energy fields, maintaining stability before and after contraction. (c) Force-deformation relationship in a sarcomere, where active and passive forces establish bistable states under biological energy field influence. (d) Bistable lattice consisting of active units connected by elastic elements (stiffness k), with stable state separation $2L$. The force-displacement response combines active potential φ_a (field-driven) and passive potential φ_p (intrinsic stiffness). (e)-(g) Dependence of potential energy $\mathscr{U}_i$ and force f_i on displacement u_i for s_i (e) varied from 5e-4 to 5e-3 $\mathrm{g \cdot m^{-2} \cdot s^{-2}}$, A_0 (f) varied from 5e-4 to 1e-2 $\mathrm{g \cdot m^{-2} \cdot s^{-2}}$, and A_1 (g) varied from 5e-4 to 5e-3 $\mathrm{g \cdot m^{-2} \cdot s^{-2}}$, where the energy landscape of the active bistable lattice is reset as s_i increases. Active stiffness modulation transforms the energy landscape, creating asymmetric potential distributions that induce nonreciprocity. (h)-(j) Transition wave propagation for $\xi = 0$ (h), $\xi = 0.03$ (i), and $\xi = 0.06\ \mathrm{s^{-1}}$ (j). The system sustains transition waves without energy injection at $\xi = 0\ \mathrm{s^{-1}}$, while active control enables transition wave propagation of u_i and s_i at higher ξ values. Parameters: $m = 1$ g, $k = 1\ \mathrm{g \cdot s^{-2}}$, $\eta = 1\ \mathrm{g \cdot s^{-1}}$, $N = 101$, $a = 0.002$ m, $B_n = 2\ \mathrm{g \cdot m^{-2} \cdot s^{-2}}$ $(n = 0, 1)$, $L = 1$ m, $\delta = 2$.

2. Active bistable system and slow-recovery dynamics

We consider a one-dimensional periodic lattice of N identical point masses m with lattice spacing a. Each mass i undergoes longitudinal motion $u_i(t)$ and is coupled to its nearest neighbors by linear springs with stiffness k. In addition, each mass is attached to two rigid walls through a pair of bistable elastic elements arranged in parallel (see Fig. 1(d)). The on-site element comprises a passive component and an active component with instantaneous potential energies φ^p and φ^a, respectively. This construction is motivated by the fact that many biophysical systems alter their energy landscapes under the interference of injected energy. For example, muscle realizes contraction and relaxation through the biologically powered automatic regulation of the binding degree between myosin heads and actin (see Fig. 1(a) and (b)). At its core, this mechanism represents a balance between the active force determined by biological energy and the passive force of the structure at different stages. Such a balance can give rise to bistable energy landscapes in many biological structures, including sarcomeres (see Fig. 1(c)). The variable affected by the injected energy is denoted by $s_i(t)$. We define $s_i(t)$ as the active stiffness, in order to represent the active component of the system stiffness coupled to the mechanical displacement $u_i(t)$. Altogether, we arrive at a two-variable coupled model for $u_i(t)$ and $s_i(t)$. The physical basis and implications of $s_i(t)$ are discussed in Appendix A.

The total on-site potential is denoted $\mathcal{U}_i(u_i; s_i)$. To obtain a bistable nonlinear potential with tunable asymmetry, we model the restoring force as the derivative of a quartic potential (Veenstra et al., 2024; Khajehtourian and Kochmann, 2021),

$$f_i(u_i; s_i) = \partial_{u_i}\mathcal{U}_i(u_i; s_i) = (u_i^2 - L^2)(s_i + A_0)u_i + L\delta^{-1}(u_i^2 - L^2)(s_i - A_1), \tag{1}$$

with constants $L > 0$ and $\delta > 0$. For brevity, the derivation of Eq. (1) is given in Appendix A.

We refer to $A_0 > 0$ and $A_1 > 0$ as passive stiffness, which represent the intrinsic structural stiffness of the bistable units, in contrast to active stiffness.

The FitzHugh-Nagumo model (FitzHugh, 1955, 1961) is a phenomenological model originally developed for neuronal excitability. Within this framework, we adopt its abstract representation of universal fast-activation and slow-recovery cycles observed in excitable biological systems. This formalism naturally extends to describe the rapid contraction and subsequent slow recovery of sarcomeres in muscle fibers, where rapid mechanical activation is succeeded by a slower metabolic restoration phase. We posit that the active stiffness $s_i(t)$ evolves on a slow time scale according to

$$\dot{s}_i = \varepsilon\,(a_0 - a_1 u_i - b s_i), \qquad 0 < \varepsilon \ll 1,\ a_0 > 0, a_1 > 0, b > 0, \tag{2}$$

where the small parameter ε encodes the separation of timescales ensuring recovery is slower than excitation. The coupling term $a_1 u_i$ linearly links recovery dynamics to the fast deformation variable u_i. The constants a_0, a_1, and b govern respectively the baseline recovery level, sensitivity to fast deformation, and rate of return to equilibrium.

Note that the displacement $u_i(t)$ is treated as a fast variable, whereas the active stiffness $s_i(t)$ is defined as a slow recovery variable. This formulation adapts the FitzHugh-Nagumo framework to our bistable mechanical system, where the variation of active stiffness phenomenologically represents the internal restorative state analogous to that of a muscle fiber following contraction. Rewriting Eq. (2) as $\dot{s}_i = -(\varepsilon b)\big(s_i - (a_0/b - (a_1/b)u_i)\big)$ shows that s_i relaxes exponentially toward the deformation-dependent target $s_\infty(u_i) = a_0/b - (a_1/b)\,u_i$ at rate εb. Making the identifications $\xi = \varepsilon b$, $B_0 = a_0/b$, and $B_1/L = a_1/b$ leads to the slow-recovery law used here,

$$\dot{s}_i = -\xi\big(s_i - B_0 + B_1 L^{-1} u_i\big). \tag{3}$$

where ξ denotes the recovery rate of the active stiffness $s_i(t)$. The derivation of Eq. (3) can be found in Appendix A. Note that Eqs. (1) and (3) define a phenomenological model that simulates the evolution of sarcomeres during muscle fiber contraction and the associated dynamical characteristics of slow recovery. The assumed dynamical form of the phenomenological equations has already been extensively applied to describing the dynamical processes of active structures (Göktepe et al., 2014).

For any fixed s_i the stationary points of $\mathcal{U}_i$ satisfy $f_i(u_i; s_i) = 0$ which, according to Eq. (1), gives the three roots

$$u^L = -L, \qquad u^R = L, \qquad u^M = \left(A_1 - s_i\right)\left(A_0 + s_i\right)^{-1} L\delta^{-1}. \tag{4}$$

In the parameter regime of interest the points u^L and u^R are local minima and u^M is a local maximum, hence each site admits two stable equilibria.

To probe directional transport, we set $(u^{f|b}_{i,\text{init}}, s^{f|b}_{i,\text{init}}) = (u^{L|R}, B_0 \pm B_1)$, such that $s^{f|b}_{i,\text{init}} \gtrless A_1$, respectively, where the symbol $\gtrless$ compactly denotes $>$ for the forward case and $<$ for the backward case, and superscripts $f|b$ and $L|R$ indicate forward/backward and left/right states, respectively. The corresponding initial energy difference at site i is given by

$$\Delta\mathcal{U}^{f|b}_{i,\text{init}} = \mathcal{U}_i(u^R; s^{f|b}_{i,\text{init}}) - \mathcal{U}_i(u^L; s^{f|b}_{i,\text{init}}) \gtrless 0. \tag{5}$$

which sets opposite energetic preferences for switching during forward and backward excitations.

Eq. (3) defines the recovery mechanism of the slow variable in the coupled fast-slow system. The displacement executes an excitable excursion under external or neighbor-induced stimuli, while s_i evolves slowly over the time scale $O(\xi^{-1})$, driven by its coupling to the local displacement u_i. As a traveling front passes, s_i changes the magnitude in a history dependent manner, thereby reshaping the local potential $\mathcal{U}_i$. Consequently the pair $(\mathcal{U}_i, s_i)$ left behind a front depends on the propagation direction and on the sequence of prior switches at the same spatial location. The mapping $\mathcal{R} : (u_i, s_i) \mapsto (-u_i, s_i)$ does not leave the coupled dynamics invariant because $\dot{s}_i$ depends affinely on u_i. Hence the initial energy landscape for a right-going excitation is not the reflection of that for a left-going excitation. This lack of time reversal symmetry yields direction-dependent thresholds and wave speeds that are controlled by the parameters A_0, A_1, B_0, B_1 and the recovery rate ξ. Moreover, the variation of the parameters leads to a further increase or decrease in this asymmetry (see Fig. 1(e)-(g)).

Fig. 1 illustrates the composition of the active bistable lattice inspired by sarcomere dynamics and its capability to sustain propagating transition waves (see Movie 1). In this lattice, the potential energy of each bistable element is regulated by the active and passive stiffness parameters, enabling a tunable energy landscape. In addition, the active bistable lattice exhibits an energy self-resetting mechanism. The slow evolution of the active stiffness under energy injection enables changes in the positions corresponding to the high and low stable states of the active elements. Specifically, Fig. 1(a)-(c) depict the morphology and composition of a sarcomere, the fundamental unit of a muscle fiber, whose contraction exhibits bistability under the regulation of active elements. In the early stage of contraction, energy injection strengthens the active force relative to the passive force; as the deformation increases, the passive force becomes dominant, gradually driving the system toward the next stable state. In Fig. 1(d), we present the active bistable lattice inspired by this mechanism along with its fundamental unit. As shown in Fig. 1(e)i, as the active stiffness s_i increases from 5e-4 $\mathrm{g \cdot m^{-2} \cdot s^{-2}}$ to 5e-3 $\mathrm{g \cdot m^{-2} \cdot s^{-2}}$, the potential energy at $u_i = L$ gradually becomes lower than that at the $u_i = -L$, eventually differing by nearly a factor of 25. In Fig. 1(f)i, as the passive stiffness parameter A_0 increases from 5e-4 $\mathrm{g \cdot m^{-2} \cdot s^{-2}}$ to 1e-2 $\mathrm{g \cdot m^{-2} \cdot s^{-2}}$, the potential energy of the entire unit decreases except at $u_i = 0$, where it remains unchanged. Throughout this process, the potential energy at $u_i = -L$ consistently remains 1.5 times that at $u_i = L$. Fig. 1(g)i shows that as A_1 increases from 5e-4 $\mathrm{g \cdot m^{-2} \cdot s^{-2}}$ to 5e-3 $\mathrm{g \cdot m^{-2} \cdot s^{-2}}$, the potential energy difference between $u_i = L$ and $u_i = -L$ increases by a factor of 11. Meanwhile, as shown in Fig. 1(e)-(g), the lattice remains bistable within the above parameter ranges. We find that as s_i increases from 5e-4 $\mathrm{g \cdot m^{-2} \cdot s^{-2}}$ to 5e-3 $\mathrm{g \cdot m^{-2} \cdot s^{-2}}$, the positions corresponding to the high and low stable states of the active elements also switch. This switching underlies the ability of the active bistable lattice to support bidirectional transition wave propagation in the absence of external forces. The active stiffness s_i evolves slowly through energy injection, and the slow-recovery process enables self-resetting of the energy landscape after completion of the transition wave propagation.

Across a broad parameter space, the proposed active bistable two-variable coupled model can achieve both reciprocal and nonreciprocal dynamics through the tuning of stiffness parameters. It simultaneously maintains a stable bistable potential landscape which supports the propagation of transition waves. The fundamental driving force of nonreciprocity originates from the difference in the initial energy landscapes along the two directions. This asymmetry in the energy landscape is realized by the two-variable coupled model, thereby endowing the system with a time reversal asymmetry. In Fig. 1(h), we verify the capability of an inactive bistable system to stably propagate transition waves. Next, we introduce the slow recovery variable $s_i(t)$ in Fig. 1(i) and assign it a recovery rate ξ of 0.03 $\mathrm{s^{-1}}$. The result shows that the active bistable lattice is capable of stably propagating transition waves. We observe that the onset of variation in the active stiffness $s_i(t)$ is synchronized with the displacement variable $u_i(t)$, while its overall duration is extended. This is because, in our two-variable coupled model, s_i is designated as a slow recovery variable and is regulated by ξ. In Fig. 1(j), we increase the recovery rate to 0.06 $\mathrm{s^{-1}}$. The transition wave propagates smoothly through the system, and it is clearly observed that the transition duration of s_i is shorter than that when $\xi = 0.03\ \mathrm{s^{-1}}$. In summary, the proposed two-variable coupled active bistable lattice is capable of supporting stable transition waves both before and after energy injection. By tuning the slow-variable parameters, the energy landscape can be reset, thereby imparting the system with nonreciprocal dynamical characteristics.

Next, we analyze the bidirectional propagation patterns of nonreciprocal transition waves using a numerical model and examine how the pair $\left(B_0, B_1\right)$, together with ξ, governs the reversible propagation of nonreciprocal waves in the active bistable lattice. At the same time, the possibility of realizing the modulation and controlled propagation of nonreciprocal transition waves is explored through the active self-resetting system. We analyze the existence and admissibility of nonreciprocal traveling wave solutions of the two-variable coupled model. Finally, we quantify the induced energy flux asymmetry implied by Eq. (5), and explore how the tunable pair (ζ, δ) governs reversible nonreciprocal propagation in the active bistable lattice.

3. Discrete theory of the active bistable system

In what follows, the discrete lattice model is adopted as the primary description of the lattice dynamics and serves as the benchmark for the continuum formulation, asymptotic analysis, and machine-learning surrogate. To analyze wave propagation in the active bistable lattice, we next formulate the discrete equations of motion. Throughout this section indices run as $i = 1, \dots, N$.

Defining the forward difference $(\nabla_d u)_i = u_{i+1} - u_i$ and the discrete Laplacian $(\Delta_d u)_i = u_{i+1} - 2u_i + u_{i-1}$, the discrete Lagrangian is

$$\mathscr{L} = T - V_{\mathrm{spr}} - V_{\mathrm{on}} = \sum_{i=1}^{N} \frac{m}{2}\dot{u}_i^2 - \sum_{i=1}^{N-1} \frac{k}{2}(\nabla_d u)_i^2 - \sum_{i=1}^{N} \mathscr{U}_i(u_i; s_i), \tag{6}$$

where T denotes the kinetic energy, V_{spr} the nearest neighbor spring interaction and V_{on} the on-site bistable contribution.

Energy dissipation occurs in many biological structures and artificially engineered materials during deformation (Raney et al., 2016). To incorporate nonconservative effects of the bistable lattice, we consider a linear viscous damping with coefficient η. Then, the Rayleigh dissipation is given by

$$\mathscr{R} = \sum_{i=1}^{N} \frac{\eta}{2}\dot{u}_i^2, \qquad \eta > 0. \tag{7}$$

Hence the Euler-Lagrange equation reads

$$\frac{\mathrm{d}}{\mathrm{d}t}\left(\partial_{\dot{u}_i}\mathscr{L}\right) - \partial_{u_i}\mathscr{L} = -\partial_{\dot{u}_i}\mathscr{R}. \tag{8}$$

Substituting the Eqs. (6) and (7) into Eq. (8) (see Appendix A), we arrive at the discrete equation of motion,

$$m\ddot{u}_i + \eta\dot{u}_i = k(\Delta_d u)_i - f_i(u_i; s_i), \qquad i = 1, 2, \dots, N, \tag{9}$$

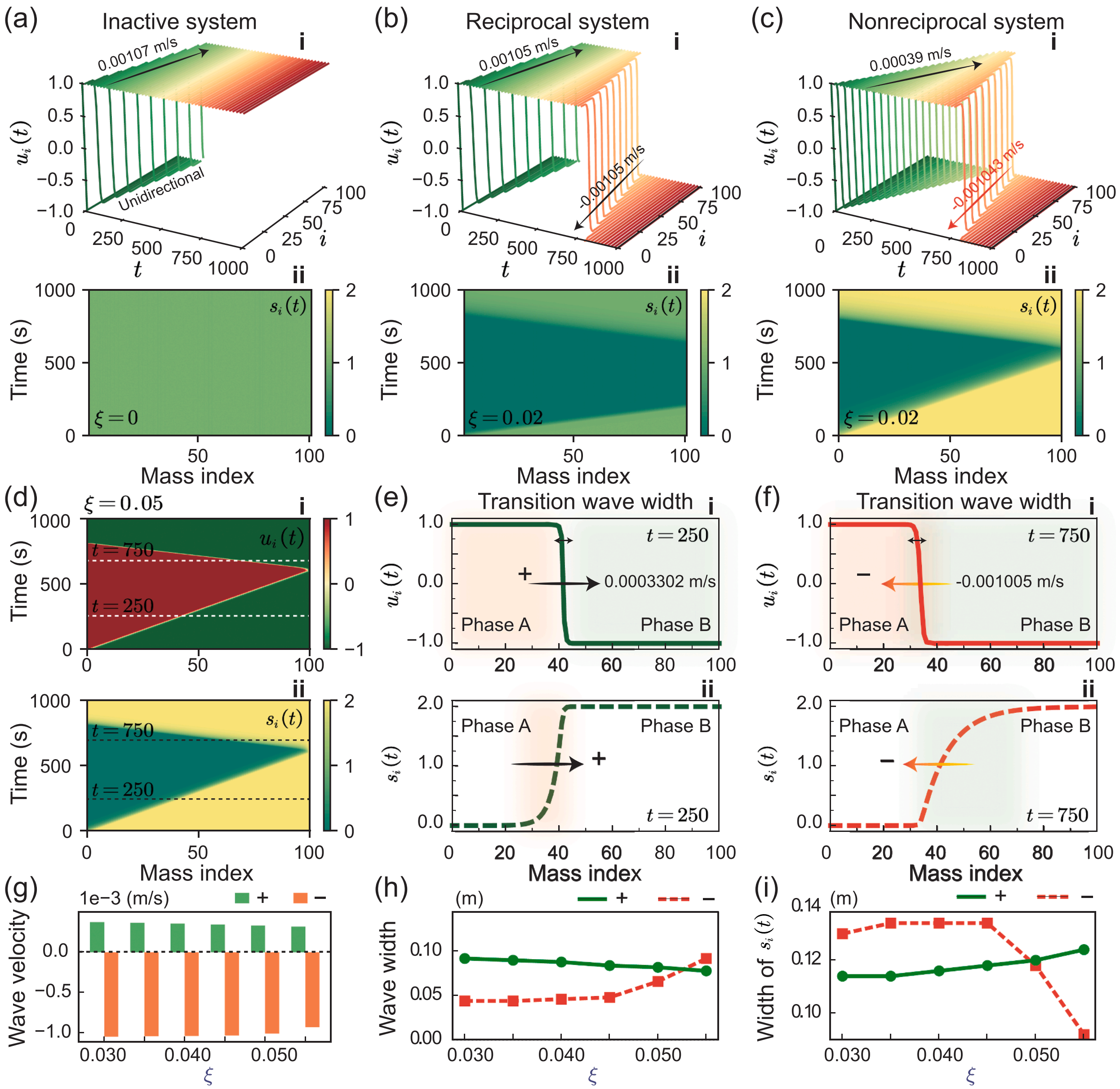

Fig. 2. Tuning and quantitative analysis of nonreciprocity in active self-resetting bistable lattices. (a)-(c) Spatiotemporal evolution of $u_i(t)$ and $s_i(t)$ for inactive (a), reciprocal (b), and nonreciprocal (c) systems. Control of $s_i(t)$ enables unidirectional waves (a), constant-speed bidirectional waves (b), and asymmetric bidirectional waves (c) without external resetting forces. (d)-(f) Spatiotemporal dynamics at $\xi = 0.05\ \mathrm{s}^{-1}$ (d) with snapshots at $t = 250$ s (e) and $t = 750$ s (f), revealing distinct waveforms, speeds (forward 3.302e-4 m/s, backward 1.005e-4 m/s), and widths for forward versus backward propagation. (g) Wave speed versus ξ showing nonlinear decrease for both directions. (h) and (i) Mechanical wave width (u_i) (h) and active wave width (s_i) (i) versus ξ, exhibiting nonlinear variation with opposite trends for forward and backward waves. Parameters: $m = 1$ g, $k = 1\ \mathrm{g \cdot s^{-2}}$, $\eta = 1\ \mathrm{g \cdot s^{-1}}$, $N = 101$, $a = 0.002$ m, $2A_n = B_n = 2\ \mathrm{g \cdot m^{-2} \cdot s^{-2}}$ $(n = 0, 1)$, $L = 1$ m, $\delta = 2$.

Eq. (9) together with the slow-recovery law Eq. (3) extend the conservative lattice dynamics by a linear viscous term and by a first order relaxation for s_i. For numerical study we adopt a symmetric parameter reduction with $A_0 = A_1 = A$, $B_0 = B_1 = B/2$, and $B/A = 2$, which preserves the qualitative physics. Forward propagation is initiated by setting $u_1(0) = L$, $u_i(0) = -L$ for $i > 1$, and $s^f_{i,\mathrm{init}} = B$ for all $i = 1, 2, \ldots, N$. Backward propagation is prepared by the mirrored state $u_N(0) = -L$, $u_i(0) = L$ for $i < N$, with $s^b_{i,\mathrm{init}} = 0$.

As shown in Fig. 2, we present the spatiotemporal dynamics of nonlinear transition waves in the symmetric (after self-resetting) active bistable lattice under forward and backward initializations (see Movie 2). In the bidirectionally reversible system, we find that the active wave (evolution of the active stiffness $s_i(t)$) propagates through the system at the same speed as the mechanical wave. In contrast to the mechanical transition wave, such an active wave propagates on a slower time scale than the switching of individual units occurs. Specifically, Fig. 2(a) shows that the single-variable discrete model of the inactive bistable lattice supports only unidirectional transition waves propagating at speed below 1 m/s, such as speed 0.00107 m/s. After introducing the slow recovery variable $s_i(t)$, the two-variable coupled active bistable lattice is capable of propagating bidirectional reciprocal transition waves with specific speeds such as 0.00105 m/s in Fig. 2(b). Moreover, the nonreciprocal mechanical response of the active system following excitation is shown in Fig. 2(c). When $A_0 = A_1 = 1\ \mathrm{g} \cdot \mathrm{m}^{-2} \cdot \mathrm{s}^{-2}$, $B_0 = B_1 = 1\ \mathrm{g} \cdot \mathrm{m}^{-2} \cdot \mathrm{s}^{-2}$, the nonreciprocal behavior arises and the forward-backward speed difference is nearly twice the forward wave speed.

At the beginning, all units are placed in the lower-energy equilibrium u^L (Phase A) except the leftmost one which is set in the higher-energy state u^R (Phase B). When the system is released at $t = 0$ this unstable configuration evolves into a forward-propagating transition wave traveling with constant speed $c_f > 0$. At a later time $t = t_{\mathrm{back}}$, the mirrored configuration is released from the opposite boundary and a backward-propagating wave emerges with velocity $c_b < 0$. The observation that $c_f < |c_b|$ demonstrates a pronounced nonreciprocal behavior even though the lattice is geometrically symmetric and no external forcing is applied. This outcome is consistent with the theoretical model and highlights the role of the coupled slow recovery variable in breaking spatiotemporal reversal symmetry. Fig. 2(c) also illustrates the evolution of the active stiffness $s_i(t)$. As the displacement front advances, s_i develops a broad co-propagating profile referred to as intermediate phase. Unlike the rapid switch of u_i, the change of s_i occurs on a slower timescale determined by the recovery dynamics. This leads to a persistent intermediate pattern that trails behind the mechanical front. The coexistence of a fast displacement front and a slow recovery profile resembles the behavior of classical excitable systems such as the FitzHugh-Nagumo model. We, therefore, are able to distinguish between the mechanical transition wave, by identifying abrupt changes in displacement and the active wave, by the trailing evolution of s_i. Both of them propagate with identical velocity, forming a coupled wave pair.

To further investigate the nonreciprocity of forward and backward transitional waves, we shorten the time interval between them and illustrate the spatiotemporal evolution of $u_i(t)$ and $s_i(t)$ in Fig. 2(d). Additionally, we extract the waveforms of the forward and backward waves at $t = 250$ s and $t = 750$ s in Fig. 2(e) and (f), respectively. We find that the forward and backward waves differ not only in wave speed but also significantly in wave width, with such differences being even more pronounced in the active waves. The differentiation in wave width between mechanical and active waves indicates that, at any instant, the number of units affected by the mechanical wave is significantly smaller than that affected by the active wave. This observation corresponds to the results shown in Fig. 2(c) and (d), as reflected in the extent of the intermediate phase. Fig. 2(e) and (f) also provides a spatial perspective of the phase distribution during wave propagation. The lattice is partitioned into three distinct regions: the original Phase A or B, the fully switched Phase B or A, and the intermediate phase. This three-phase organization records the history of wave passage and generates a direction-dependent reshaping of the energy landscape, which underlies the intrinsic nonreciprocal response of the system.

In Fig. 2(g), as ξ increases from 0.03 s^{-1} to 0.055 s^{-1}, we find that in the two-variable coupled nonreciprocal discrete model, both the forward and backward wave speeds exhibit a nonlinear decreasing trend while remaining below 1 m/s. Meanwhile, the ratio of the absolute values of the backward to forward wave speeds remains nearly constant at approximately 3.04. Fig. 2(h) shows that, as ξ increases from 0.03 s^{-1} to 0.055 s^{-1}, the width of the forward mechanical wave decreases nonlinearly, while that of the backward mechanical wave increases nonlinearly. However, the relationship between the wave width and the parameter ξ shows opposite trends for the forward and backward waves as shown in Fig. 2(i). This is because the forward and backward wave propagations are respectively dominated by the active and passive restoring forces, which result from the initial conditions of the discrete model (according to Eq. (5)). At the same time, we observe that when ξ ranges from 0.03 s^{-1} to 0.055 s^{-1}, the width of the mechanical waves lies between 0.04 m and 0.09 m, whereas the width of the active waves lies between 0.09 m and 0.139 m. This further indicates that the intermediate state of s_i is prevalent in the two-variable coupled model across various recovery rates. The results indicate that the nonreciprocity of wave propagation in the system is indeed closely linked to the energy injection rate (i.e., the recovery rate of s_i), further highlighting the advantages of the two-variable coupled system.

In summary, in the geometrically symmetric system with self-resetting energy landscape, we realize the propagation of passive unidirectional transition waves, active reciprocal transition waves, and active nonreciprocal transition waves. We further quantify the forward and backward wave speeds and widths of the nonreciprocal transition waves, and find that both vary nonlinearly with the parameter ζ.

4. Continuum description of nonreciprocal dynamics

To derive analytical results for the active bistable lattice, the discrete model is converted into a continuous approximation. By assuming that the width of the transition wave is much larger than the lattice constant a, it is reasonable to take $N \to \infty$ with the total length $L_{\mathrm{sys}} = Na$ fixed. We set $x_i = ia$ and identify $u_i(t) \to u(x,t)$ and $s_i(t) \to s(x,t)$. For fixed t, a Taylor expansion of $u(\cdot,t)$ about the reference position $x = ia$ to the points $x = (i \pm 1)a$ yields

$$u\Big|_{x=(i\pm1)a} = u(ia) \pm a\,u_x\Big|_{x=ia} + \frac{a^2}{2}\,u_{xx}\Big|_{x=ia} + \mathcal{O}(a^3), \tag{10}$$

where u_x denotes the first partial derivative of $u(x,t)$ with respect to x.

Equivalently, noting $u_{i\pm1} = u(x_i \pm a, t)$ and setting $x = x_i$, we obtain

$$u_{i\pm1} \;\to\; u(x,t) \pm a\,u_x(x,t) + \frac{a^2}{2}\,u_{xx}(x,t), \tag{11}$$

where the truncation error in Eqs. (10) and (11) is $\mathcal{O}(\varepsilon^3)$ in nondimensional terms.

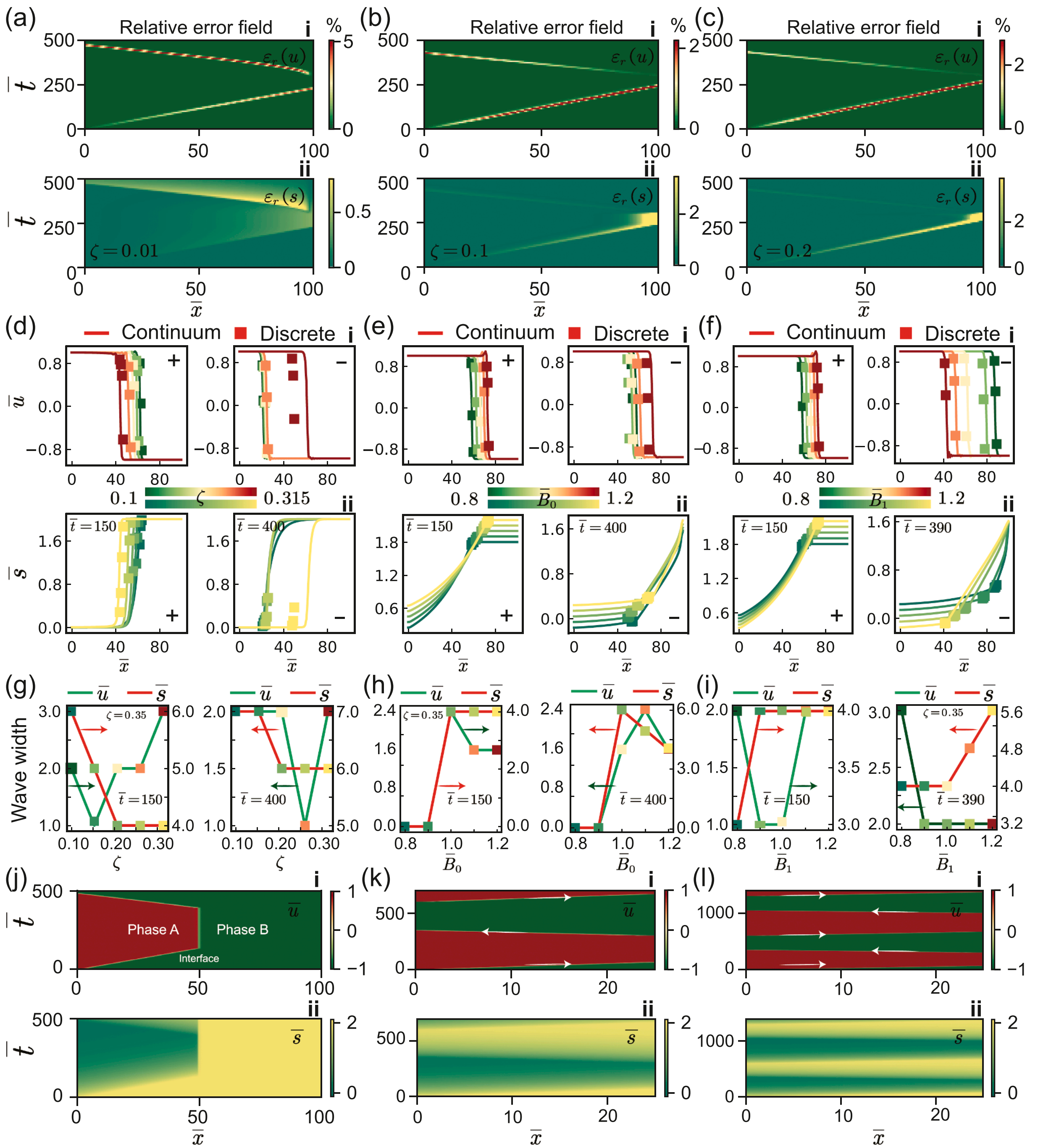

Fig. 3. Numerical results of the continuum model: analysis of the relative error field for the two-variable coupled dimensionless continuum model, variations of waveform, wave speeds and wave width with ζ, $\bar{B}_0$ and $\bar{B}_1$, and propagation of multiple controllable transition waves. (a)-(c) Relative error fields in $\bar{x}-\bar{t}$ coordinates for $\zeta = 0.01$ (a), $\zeta = 0.1$ (b), and $\zeta = 0.2$ (c). The continuous model shows reasonable agreement with $\bar{u}_i(t)$ errors remaining small, while $\bar{s}_i(t)$ errors reflect increased sensitivity to backward wave initiation timing at larger ζ. (d)-(f) Waveform and wave speed analysis of forward and backward transition waves at varying $\zeta = 0.1 \sim 0.315$ (d), $\bar{B}_0 = 0.8 \sim 1.2$ (e), and $\bar{B}_1 = 0.8 \sim 1.2$ (f). (g)-(i) Mechanical and active wave widths versus ζ (g), $\bar{B}_0$ (h), and $\bar{B}_1$ (i) for both models when $\zeta = 0.35$. Nonlinear variations demonstrate tunable nonreciprocity. (j) Controllable return position of backward transition waves, showing programmable stopping of forward waves and on-demand initiation of backward waves. (k) and (l) Multiple realizations of bidirectional transition waves, demonstrating two (k) or more (l) cycles with selectable return positions and stable repeated propagation.

To obtain a properly scaled continuum limit with $\mathcal{O}(1)$ macroscopic coefficients, we introduce the macroscopic scalings $\rho = m/a$, $k' = ka$, and $\eta' = \eta/a$. Substituting the Eq. (11) into Eq. (9), we obtain the continuum equations as (see Appendix B)

$$\rho\,\ddot{u} - k'\,u_{xx} + \eta'\,\dot{u} + a^{-1}(u^2 - L^2)\big((s + A_0)u + (s - A_1)L\delta^{-1}\big) = 0, \tag{12}$$

and

$$\dot{s} + \xi\,(s - B_0 + B_1 L^{-1} u) = 0. \tag{13}$$

Note that Eq. (13) represents the continuous form of Eq. (3) with $u_i \to u$ and $s_i \to s$.

Furthermore, by introducing the dimensionless variables and parameters $\bar{x} = x/X$, $\bar{t} = t/T$, $\bar{u} = u/U$, $\bar{s} = s/S$, $\bar{A}_n = A_n/S$, $\bar{B}_n = B_n/S$ $(n = 0, 1)$, where $X^2 = k'T^2/\rho$, $T = \rho/\eta'$, $U = L$, and $S = a\eta'^2/(\rho U^2)$, we yield the nondimensional forms of Eqs. (12) and (13) as

$$\ddot{\bar{u}} - \bar{u}_{\bar{x}\bar{x}} + \dot{\bar{u}} + (\bar{u}^2 - 1)\big((\bar{s} + \bar{A}_0)\bar{u} + (\bar{s} - \bar{A}_1)\delta^{-1}\big) = 0, \tag{14}$$

and

$$\dot{\bar{s}} + \zeta\,(\bar{s} - \bar{B}_0 + \bar{B}_1 \bar{u}) = 0, \qquad \zeta = T\xi, \tag{15}$$

where $\bar{A}_n$ $(n = 0, 1)$ denote the dimensionless passive stiffnesses and $\bar{B}_n$ determine the steady-state level of the active stiffness. Moreover, ζ serves as a prefactor, indicating the dimensionless rate at which $\bar{s}$ recovers. The derivation related to Eqs. (14) and (15) is given in Appendix B. The system is initialized such that $\bar{u}(\bar{x}, 0) = 1$ for $0 \leqslant \bar{x} < R \ll \bar{L}_{sys}$ and $\bar{u}(\bar{x}, 0) = -1$ otherwise, where R denotes the length of the initially excited region used to launch the front. The active stiffness is prescribed as $\bar{s}(\bar{x}, 0) = \bar{B}_0 + \bar{B}_1 > A_1 > 0$.

Fig. 3 summarizes the numerical results, including waveforms, wave speeds and wave widths, obtained from the two-variable coupled dimensionless continuum model. It also demonstrates the agreement between the continuum and discrete models, thereby validating the effectiveness of the continuum model. Specifically, we solve the continuum model using the semi-implicit Crank-Nicolson numerical method (Srivastava and Tamsir, 2012) based on finite differences. The relative error field defined by $\varepsilon_r = |f_c - f_d| \,/\, |f_d|$ between the dimensionless continuum model and the discrete model is presented in Fig. 3(a)-(c), where f_c and f_d represent the numerical results of the continuous and discrete models, respectively. The results confirm the accuracy and validity of the continuum model described by Eqs. (14) and (15).

As shown in Fig. 3(a)-(c)i, the error observed in the displacement variation field arises from the intrinsic differences between the discrete and continuum models. Therefore the error is mainly concentrated near the mechanical transition front. In contrast, the error in the active stiffness field shown in Fig. 3(a)-(c)ii primarily originates from the inconsistency in the slow variation of $s_i(t)$ after the continuum approximation. Both types of errors remain within a reasonable range and exhibit excellent agreement with the theoretical model. Moreover, with the increase of the dimensionless recovery rate ζ from 0.01 to 0.2, we observe a pronounced growth of the relative error field near the end of the lattice. This deviation primarily arises from the mismatch between the slow evolution of $s_i(t)$ and the initiation time of the backward wave, which results in a slight system desynchronization. A detailed analysis of this phenomenon is provided in Appendix H. Therefore, we focus on the set of parameters ζ, $\bar{B}_0$ and $\bar{B}_1$ that influence the active stiffness.

In Fig. 3(d), we present the waveforms and their positions at $\bar{t} = 150$ (forward wave) and $\bar{t} = 400$ (backward wave) as the dimensionless recovery rate ζ increases from 0.1 to 0.315. We find that both the forward and backward waves lag in position when $\zeta = 0.315$, indicating the slowest propagation speeds. But this lag is substantially more pronounced for the backward wave. This indicates that the dimensionless recovery rate ζ of $s_i(t)$ influences the forward and backward wave speeds to different extents. The difference constitutes one of the sources of nonreciprocity in the two-variable coupled model. As shown in Fig. 3(e), as $\bar{B}_0$ increases from 0.8 to 1.2, the forward wave speed gradually increases whereas the backward-wave speed gradually decreases, and these distinct trends make the nonreciprocity of the active bistable lattice more pronounced. We also find that increasing $\bar{B}_1$ promotes the wave speeds In Fig. 3(f). Both the forward and backward wave speeds grow as $\bar{B}_1$ increases from 0.8 to 1.2, with the backward wave exhibiting a larger increase. This indicates that the larger the coefficient $\bar{B}_1$ of the first-order term of the dimensionless displacement variable $\bar{u}$ in Eq. (15), the stronger the system's nonreciprocity. Fig. 3(g) shows that as ζ increases from 0.1 to 0.15, the width difference between the forward mechanical wave at $\bar{t} = 150$ and the backward mechanical wave at $\bar{t} = 400$ gradually decreases from 1 to 0. As ζ further increases to 0.315, this width difference gradually rises to 0.5 and then remains stable. In Fig. 3(h), we find that when $\bar{B}_0$ ranges from 0.8 to 1 ($\zeta = 0.35$), the widths of the forward and backward mechanical waves are identical. When $\bar{B}_0$ increases to 1.2, the width difference grows from 0 to 0.8. As $\bar{B}_1$ increases from 0.8 to 0.9 ($\zeta = 0.35$), the width difference between the forward and backward mechanical waves decreases from 1.3125 to 0.3125 in Fig. 3(i). During the increase of $\bar{B}_1$ to 1, the width difference remains constant; as $\bar{B}_1$ continues to increase, the width difference rises again to 1 (corresponding to $\bar{B}_0 = 1.2$). Based on the above analysis of the active bistable lattice dynamics, we find that the ranges of ζ, $\bar{B}_0$, and $\bar{B}_1$ influence the propagation speeds and widths of transition waves. Thus these three parameters constitute key factors in determining the system's nonreciprocity in the two-variable coupled model.

For better characterizing the spatiotemporal dynamics of the bistable lattice, we employ the continuum model and control the initiation time of the backward wave to achieve the optimal outcome in the subsequent analysis (see Movie 3). By using numerical methods, we achieve the forward stopping and backward initiation of transition waves at the intermediate position $\bar{x} = 50$ in the active bistable lattice in Fig. 3(j). The implementation of this case provides a foundation for realizing arbitrary return positions in the lattice. As shown in Fig. 3(k) and (l), building on the controllable return positions, we achieve multiple back-and-forth propagations of transition waves within 25 units over the time intervals from $\bar{t} = 0$ to $\bar{t} = 700$ and 1400, respectively. Taken together, both variables transition from phase A to B and then return by waves that travel at uniform velocities $\bar{c}_f$ and $\bar{c}_b$, establishing robust nonreciprocity quantified by $\bar{c}_f - |\bar{c}_b|$. In this section, unless otherwise specified, the following dimensionless parameter values are used by default: $\zeta = 0.01$, $\delta = 2$ and $\bar{A}_n = \bar{B}_n = 1$ $(n = 0, 1)$.

When the recovery rate ζ is sufficiently small, both the shape and the width of the nonreciprocal transition waves converge to steady values as illustrated in Fig. 3. Guided by this observation and in the large system limit $\bar{L} \to \infty$, we introduce the traveling wave coordinate

$$z = H(\bar{x})\big(\bar{x} - \bar{c}_f \bar{t}\big) + \big(1 - H(\bar{x})\big)\big(|\bar{c}_b|\bar{t} - \bar{x}\big), \tag{16}$$

where $H(\cdot)$ denotes the Heaviside step function, i.e. $H(x) = 1$ for $x > 0$ and $H(x) = 0$ for $x < 0$. This representation enables a unified analysis of forward- and backward-propagating waves.

5. Asymptotic multiscale theory for nonreciprocal active waves

We develop a unified matched-asymptotic framework to describe forward- and backward-propagating transition waves in an active bistable lattice. The analysis exploits the intrinsic separation of fast and slow scales. A narrow inner front region is resolved, where the mechanical variable $\bar{u}$ switches over a spatial scale $z \sim \mathcal{O}(1)$. And a broad outer recovery region is identified, where the active variable $\bar{s}$ relaxes on a scale $z \sim \mathcal{O}(\zeta^{-1})$. Asymptotic matching of these two layers yields uniformly valid composite profiles. The analysis also determines direction-dependent speed selection to first order in the small parameter ζ. In principle, higher-order corrections (e.g., $\mathcal{O}(\zeta^2)$) could be derived. However, such terms would lead to prohibitively cumbersome expressions. More importantly, the regular perturbation framework still has difficulty enforcing a globally smooth connection between the inner front and the outer recovery region. The separately constructed inner and outer solutions typically exhibit a finite mismatch, particularly in the far recovery zone. This discrepancy arises because the active stiffness retains a long-range memory of the loading history.

Rather than pursuing analytically unwieldy higher-order corrections, we adopt a hybrid strategy. The first-order matched-asymptotic analysis provides an accurate and physically interpretable description of the inner front and the leading-order wave speed. A machine-learning surrogate is then introduced to account for the residual mismatch in the outer region. This surrogate completes the waveform and restores global continuity. The resulting framework preserves the physical insight of the asymptotic analysis while achieving the numerical accuracy of a data-driven model.

5.1. *Matching and boundary-layer structure of forward waves*

We study a forward-propagating traveling wave with coordinate $z = \bar{x} - \bar{c}_f \bar{t}$ and speed $\bar{c}_f \in (0, 1)$. Introducing the traveling-wave variables $\bar{u}_f(z) = \bar{u}(\bar{x}, \bar{t})$ and $\bar{s}_f(z) = \bar{s}(\bar{x}, \bar{t})$, and substituting them into Eqs. (14) and (15)(see Appendix C), we obtain the reduced system for the forward front. Specifically, the governing equations take the form

$$\bar{u}_f'' - \bar{c}_f(\bar{c}_f^2 - 1)^{-1}\bar{u}_f' + (\bar{c}_f^2 - 1)^{-1}(\bar{u}_f^2 - 1)\big((\bar{s}_f + \bar{A}_0)\bar{u}_f + (\bar{s}_f - \bar{A}_1)\delta^{-1}\big) = 0, \tag{17}$$

and

$$\bar{s}_f' + \zeta\, \bar{c}_f^{-1}(\bar{B}_0 - \bar{B}_1\bar{u}_f - \bar{s}_f) = 0. \tag{18}$$

subject to the heteroclinic boundary condition $\bar{u}_f(\pm\infty) = \mp 1$ and $\bar{s}_f(+\infty) = \bar{B}_0 + \bar{B}_1$.The evolution of the active stiffness is governed by a first-order balance involving the small parameter ζ.

For $\zeta \ll 1$, the problem is singularly perturbed, and we seek regular expansions of fields and speed:

$$\bar{u}_f = \bar{u}_f^0 + \zeta\, \bar{u}_f^1 + \mathcal{O}(\zeta^2), \quad \bar{s}_f = \bar{s}_f^0 + \zeta\, \bar{s}_f^1 + \mathcal{O}(\zeta^2), \quad \bar{c}_f = \bar{c}_f^0 + \zeta\, \bar{c}_f^1 + \mathcal{O}(\zeta^2). \tag{19}$$

At leading order, Eq. (18) constrains $\bar{s}_f(z)$ to the constant value $\bar{s}_f^0 = \bar{B}_0 + \bar{B}_1$, and Eq. (17) then reduces to a scalar front problem (see Appendix C). The corresponding heteroclinic orbit is

$$\bar{u}_f^0(z) = -\tanh(\lambda_f^0 z), \tag{20}$$

where

$$\lambda_f^0 = \Big(\tfrac{1}{2}(\bar{A}_0 + \bar{s}_f^0) + (\bar{s}_f^0 - \bar{A}_1)^2\, \delta^{-2}\Big)^{1/2}, \tag{21}$$

is the leading-order inverse width, determined by the cubic nonlinearity evaluated at the asymptotic states.

The corresponding leading-order wave speed $\bar{c}_f^0$ is fixed by the traveling-wave balance (see Appendix C) and satisfies $0 < \bar{c}_f^0 < 1$:

$$\bar{c}_f^0 = \Big(1 + \tfrac{1}{2}\delta^2(\bar{A}_0 + \bar{s}_f^0)(\bar{s}_f^0 - \bar{A}_1)^{-2}\Big)^{-1/2}. \tag{22}$$

At order $\mathcal{O}(\zeta)$, integrating Eq. (18) with $\bar{u}_f^0$ given in Eq. (20) and determining the constant by boundary matching rule (see Appendix C) yields the inner correction for the stiffness field:

$$\bar{s}_f^1(z) = -\bar{B}_1(\bar{c}_f^0\lambda_f^0)^{-1}\big(\ln(\cosh(\lambda_f^0 z)) - \lambda_f^0 z + \ln 2\big). \tag{23}$$

To select the wave speed, we multiply Eq. (17) by $\mathrm{d}\bar{u}_f/\mathrm{d}z$ and integrate across the entire domain (see Appendix D). Using a localized front ansatz in the evaluation then produces the inner balance:

$$12\delta(\bar{c}_f\lambda_f)^2 - 12(\bar{s}_f^0 - \bar{A}_1)\bar{c}_f\lambda_f + (3\delta + 10)\bar{B}_1\zeta = 0. \tag{24}$$

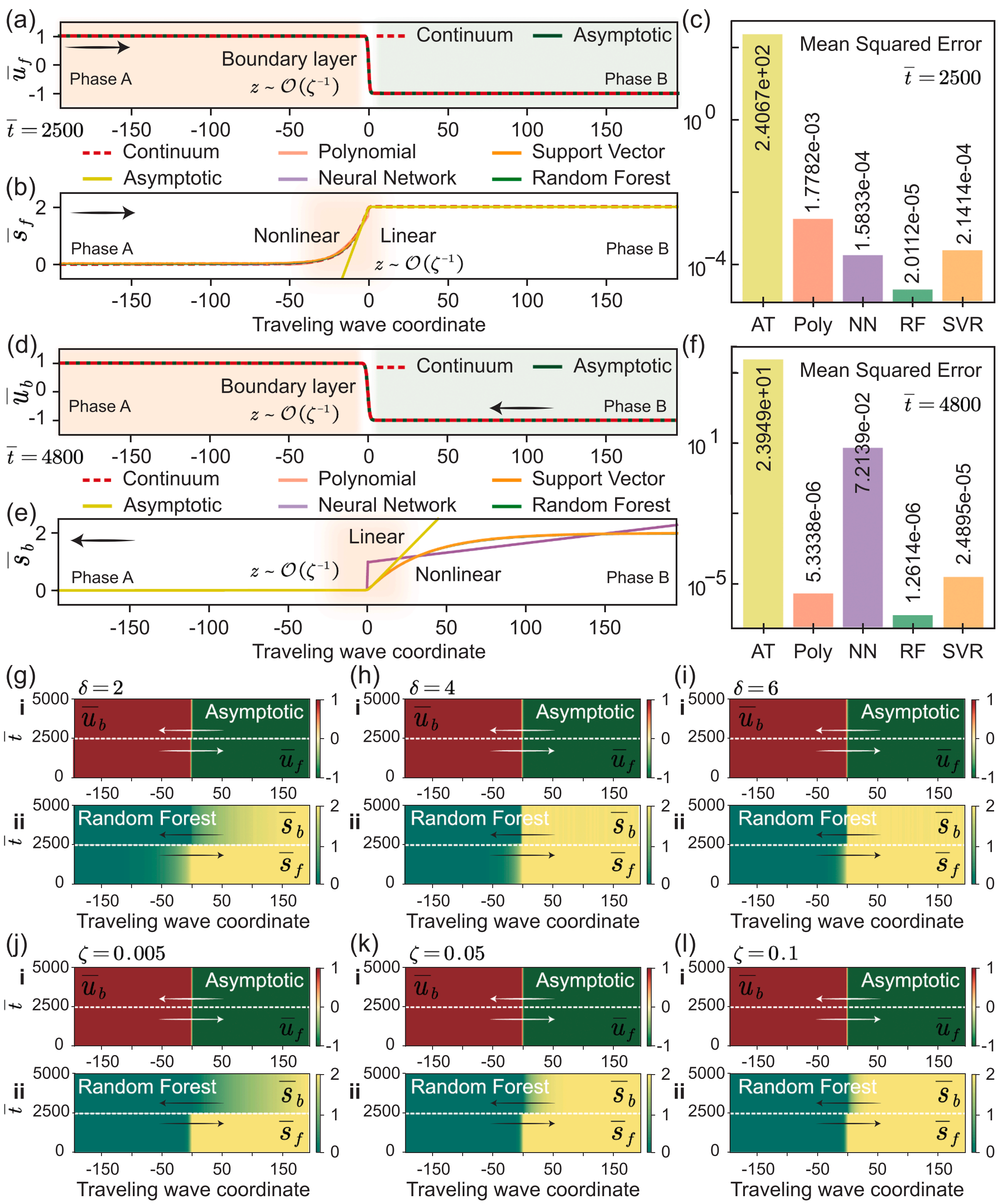

Fig. 4. Perturbation solutions of the forward and backward waves coupled with machine learning, and the spatiotemporal evolution of the traveling-wave variables $\bar{u}_f, \bar{u}_b, \bar{s}_f\ \bar{s}_b$. (a)Asymptotic expansion solution of the forward mechanical wave $\bar{u}_f$ at $\bar{t} = 2500$. (b)-(c) Standalone asymptotic expansion solution of the forward active wave $\bar{s}_f$ and asymptotic expansion solutions (b) coupled with Random Forest, Neural Networks, Support Vector Regression, and Polynomial Regression, along with their mean squared errors (c). (d) Perturbation expansion solution of the backward mechanical wave $\bar{u}_b$ at $\bar{t} = 4800$. (e)-(f) Standalone perturbation solution of the backward active wave $\bar{s}_b$ and perturbation solutions (e) coupled with Random Forest, Neural Networks, Support Vector Regression, and Polynomial Regression, along with their mean squared errors (f). Random forest best captures active wave details with minimum error (c, f) when combined with asymptotic solutions. (g)-(i) Spatiotemporal evolution of forward and backward waves coupled with random forest for $\delta = 2$ (g), $\delta = 4$ (h), and $\delta = 6$ (i). (j)-(l) Spatiotemporal evolution for $\zeta = 0.005$ (j), $\zeta = 0.05$ (k), and $\zeta = 0.1$ (l). The hybrid method accurately reproduces continuous model results and captures intermediate active stiffness states.

Independently, a linearization of Eq. (17) about the far field with the leading exponential $\phi_f = \exp(-\lambda_f z)$ (see Appendix D) furnishes a dispersion-like constraint:

$$2\delta\lambda_f^2 - 2\delta\lambda_f^2\bar{c}_f^2 - \delta\bar{c}_f\lambda_f - (\delta-1)\bar{s}_f^0 - \delta\bar{A}_0 - \bar{A}_1 = 0. \tag{25}$$

Solving Eqs. (24) and (25) perturbatively with $\bar{c}_f = \bar{c}_f^0 + \zeta\,\bar{c}_f^1 + \mathcal{O}(\zeta^2)$ and $\lambda_f = \lambda_f^0 + \zeta\,\lambda_f^1 + \mathcal{O}(\zeta^2)$, and eliminating λ_f^1, we obtain the first-order speed correction:

$$\bar{c}_f = \bar{c}_f^0 + (3\delta+10)\,\bar{B}_1\,(\lambda_f^0)^{-2}\,\Theta_f\,\Phi_f^{-1}\,\zeta + \mathcal{O}(\zeta^2), \tag{26}$$

where $\Theta_f = 4(\bar{c}_f^0)^2\lambda_f^0 + \bar{c}_f^0 - 4\lambda_f^0$ denotes the inner balance contribution arising from the front profile, and $\Phi_f = 48(2\delta\,\bar{c}_f^0\lambda_f^0 - \bar{s}_f^0 + \bar{A}_1)$ represents the far-field constraint associated with the stiffness-field coupling. For the derivation associated with Eq. (26), refer to Appendix D. In summary, Eqs. (20)-(22) provide an exact heteroclinic front at $\zeta = 0$, characterized by width $(\lambda_f^0)^{-1}$ and speed $\bar{c}_f^0 \in (0,1)$. The inner correction Eq. (23) captures the $\mathcal{O}(\zeta)$ modulation of the active stiffness across the interface, while the coupled constraints Eqs. (24) and (25) uniquely determine the perturbed speed Eq. (26) in the singular limit $\zeta \ll 1$.

5.2. Singular perturbation method of backward waves

We consider a backward-propagating front with coordinate $z = -\bar{x} + |\bar{c}_b|\bar{t}$, where $\bar{c}_b < 0$. The traveling-wave fields are defined as $\bar{u}_b(z) = \bar{u}(\bar{x},\bar{t})$ and $\bar{s}_b(z) = \bar{s}(\bar{x},\bar{t})$. The displacement field evolves according to

$$(\bar{c}_b^2 - 1)\bar{u}_b'' + |\bar{c}_b|\bar{u}_b' + (\bar{u}_b^2 - 1)((\bar{s}_b + \bar{A}_0)\bar{u}_b + (\bar{s}_b - \bar{A}_1)\delta^{-1}) = 0, \tag{27}$$

while the active stiffness satisfies

$$|\bar{c}_b|\bar{s}_b' - \zeta(\bar{B}_0 - \bar{B}_1\bar{u}_b - \bar{s}_b) = 0, \tag{28}$$

with boundary conditions $\bar{u}_b(\mp\infty) = \pm 1$ and $\bar{s}_b(-\infty) = \bar{s}_b^0$. The derivation related to Eqs. (27) amd (28) can be found in Appendix E.

To analyze the singular perturbation structure, we introduce regular expansions: the displacement field is written as $\bar{u}_b = \bar{u}_b^0 + \zeta\,\bar{u}_b^1 + \mathcal{O}(\zeta^2)$, the active stiffness as $\bar{s}_b = \bar{s}_b^0 + \zeta\,\bar{s}_b^1 + \mathcal{O}(\zeta^2)$, and the wave speed as $|\bar{c}_b| = |\bar{c}_b^0| + |\bar{c}_b^1|\zeta + \mathcal{O}(\zeta^2)$. At leading order, Eq. (28) gives $\bar{s}_b^0 = \bar{B}_0 - \bar{B}_1$. Substituting this into Eq. (27) reduces the problem to a scalar front with heteroclinic orbit $\bar{u}_b^0(z) = -\tanh(\lambda_b^0 z)$ (see Appendix E). The corresponding inverse width is

$$\lambda_b^0 = \left(\tfrac{1}{2}(\bar{A}_0 + \bar{s}_b^0) + \left(\bar{A}_1 - \bar{s}_b^0\right)^2\delta^{-2}\right)^{1/2}, \tag{29}$$

and the leading-order speed is

$$|\bar{c}_b^0| = \left(1 + \tfrac{1}{2}\delta^2(\bar{A}_0 + \bar{s}_b^0)\left(\bar{A}_1 - \bar{s}_b^0\right)^{-2}\right)^{-1/2}. \tag{30}$$

At $\mathcal{O}(\zeta)$, integration of Eq. (28) with the profile $\bar{u}_b^0$ given yields the stiffness correction (see Appendix E)

$$\bar{s}_b^1(z) = (\bar{B}_1\left(|\bar{c}_b^0|\lambda_b^0\right)^{-1})(\ln(\cosh(\lambda_b^0 z)) + \lambda_b^0 z + \ln 2). \tag{31}$$

Finally, combining the inner and outer balances determines the backward speed as

$$\bar{c}_b = -|\bar{c}_b^0| - (3\delta - 10)\bar{B}_1(\lambda_b^0)^{-2}\,\Theta_b\,\Phi_b^{-1}\,\zeta + \mathcal{O}(\zeta^2), \tag{32}$$

where $\Theta_b = 4\lambda_b^0 - 4(\bar{c}_f^0)^2\lambda_b^0 - |\bar{c}_b^0|$ represents the inner balance contribution arising from the front profile, and $\Phi_b = 48\,(2\delta|\bar{c}_b^0|\lambda_b^0 - \bar{A}_1 + \bar{s}_b^0)$ encodes the far-field constraint associated with the stiffness-field coupling. For the derivation associated with Eq. (32), refer to Appendix F, while the explicit expressions for $\bar{u}_f^1$ and $\bar{u}_b^1$ are lengthy and deferred to the Appendix G.

Fig. 4 presents the perturbation solutions of the forward and backward mechanical waves, as well as the perturbation solutions of the active waves coupled with machine learning. It also shows the spatiotemporal evolution of the forward and backward traveling-wave variables for $\delta = 2, 4$ and 6 as well as $\zeta = 0.005, 0.05$ and 0.1. Specifically, Fig. 4(a) shows that, at $\bar{t} = 2500$, the forward mechanical-wave profile $\bar{u}_f$ obtained by the asymptotic expansion method agrees closely with the numerical solution of the dimensionless continuum model. This agreement demonstrates that the asymptotic expansion solution accurately captures the key features of the forward mechanical wave. In contrast, the asymptotic expansion for the forward active wave accurately resolves only the inner region of the profile $\bar{s}_f$, namely the vicinity of the wave front. Its accuracy deteriorates in the outer region. Details are provided in Appendix C. Fig. 4(b) shows the forward active wave profile $\bar{s}_f$ obtained from the asymptotic expansion method coupled with four machine learning algorithms: Random Forest, Neural Networks, Support Vector Regression, and Polynomial Regression. In Fig. 4(c), we present the mean squared errors of the four algorithms and the asymptotic expansion solution alone. The results show that Random Forest yields the smallest mean squared error, which is 2.0112e-5.

Next, in Fig. 4(d), we present the singular perturbation solution of the backward wave at $\bar{t} = 4800$ and compare it with the backward wave profile $\bar{u}_b$ captured from the continuum model at the same time. The result shows that the perturbation solution is accurate across the entire domain. At the same time, we find that the perturbation solution of the backward active wave also exhibits insufficient accuracy in the outer region. Fig. 4(e) similarly presents the backward active wave profile $\bar{s}_b$ obtained from the singular perturbation method coupled with four machine learning algorithms: Random Forest, Neural Networks, Support Vector Regression, and Polynomial Regression. The results indicate that solving the backward active wave is more challenging than the forward wave.

In Fig. 4(f), we present the mean squared errors of the four algorithms. The results show that Neural Networks yields larger mean squared errors than that for the forward active wave, whereas Random Forest, Support Vector Regression and Polynomial Regression yield smaller errors. Among them, Random Forest remains the algorithm producing the smallest mean squared error 1.2614e-6 for solving the backward active wave $\bar{s}_b$. Therefore, in the following analysis, we employ the perturbation solution coupled with Random Forest to resolve the forward and backward active waves $\bar{s}_f$ and $\bar{s}_b$. Notably, the front of the active wave always coincides with the front of the mechanical wavein the perturbation solution. This behavior is in strong agreement with the numerical results (see Fig. 3(d)-(f)). This result indicates that, within the active bistable lattice, the mechanical and active transitional waves occur and propagate synchronously. The perturbation solution further reveals that both the mechanical wave and the active wave exhibit an intermediate phase. The transition details between phase A and phase B are accurately captured in both waves. The difference in the spatial scale of the intermediate phase between the two waves is also in strong agreement with the numerical results (see Fig. 3(d)-(f)). Specifically, the intermediate state of $\bar{u}$ (representing $\bar{u}_f$ and $\bar{u}_b$) scales as $z \sim \mathcal{O}((\lambda^0)^{-1})$, where λ^0 denotes λ_f^0 and λ_b^0, and the corresponding region of $\bar{s}$ (representing $\bar{s}_f$ and $\bar{s}_b$) scales as $z \sim \mathcal{O}(\zeta^{-1})$.

In Fig. 4(g)-(i), we show the temporal evolution of $\bar{u}_f$, $\bar{s}_f$, $\bar{u}_b$ and $\bar{s}_b$ in the traveling-wave coordinate z for $\delta = 2, 4$ and 6, respectively. As shown in Fig. 4(g)-(i)i, we find that variations in δ have little effect on the width of the mechanical wave, that is, the range of the intermediate state of $\bar{u}_f$ and $\bar{u}_b$. This is consistent with the designation of $\bar{u}_f$ and $\bar{u}_b$ as fast variables. It indicates that the energy landscape of the active bistable unit exerts only a weak influence on the switching speed between the stable states. As shown in Fig. 4(g)-(i)ii, as δ increases from 2 to 6, the intermediate state of $\bar{s}_f$ and $\bar{s}_b$ progressively diminish. This trend indicates that in the two-variable coupled model, the dimensionless slow recovery variables $\bar{s}_f$ and $\bar{s}_b$ are strongly influenced by the energy landscape. In particular, δ determines u^M and thereby affects the energy structure of the active bistable unit, as defined in Eq. (4).

Fig. 4(j)-(l) presents the temporal evolution of $\bar{u}_f$, $\bar{s}_f$, $\bar{u}_b$ and $\bar{s}_b$ in the traveling-wave coordinate for $\zeta = 0.005$, 0.05, and 0.1, respectively. In the two-variable coupled model, the intermediate states of $\bar{u}_f$ and $\bar{u}_b$ are insensitive to the injected energy. This behavior is illustrated in Fig. 4(j)-(l)i, where ζ, as the dimensionless recovery rate, also characterizes the rate of energy injection. In Fig. 4(j)-(l)ii, the intermediate states of $\bar{s}_f$ and $\bar{s}_b$ decrease markedly as ζ increases from 0.005 to 0.1. This effect is more pronounced than that associated with δ. A larger intermediate phase corresponds to a stronger hysteretic response induced by energy input, which is clearly evident in the spatiotemporal diagrams. Moreover, as is shown in the Fig. 4(g)ii-(l)ii, the intermediate phase of the backward wave is significantly larger than that of the forward wave. This asymmetry primarily arises from the potential energy function and initiation conditions specified in Section 2. In this section, unless otherwise specified, the following dimensionless parameter values are used by default: $\zeta = 0.02$, $\delta = 2$ and $\bar{A}_n = \bar{B}_n = 1$ $(n = 0, 1)$.

Finally, by employing asymptotic expansion, perturbation analysis, and machine learning, we derive analytical expressions that accurately capture the dynamics of forward and backward transition waves. The validity of these results is verified against numerical solutions. This framework provides a theoretical basis for the subsequent analysis of the nonreciprocal energy transmission in active bistable lattices.

6. Energy flux asymmetry in nonreciprocal active waves

In the preceding analysis, we noted that the primary nonreciprocal features of forward and backward transitional waves arise from differences in wave speed and width. The nonreciprocal wave speed represents the most direct characteristic, while the width nonreciprocity not only serves as a measure of the nonreciprocity of the system but also fundamentally influences the coupling within the bivariate system. Therefore, we define the nonreciprocity $N_{\text{rel}}(\zeta, \delta)$ and the width nonreciprocity $N_{\text{width}}(\zeta, \delta)$ as follows

$$N_{\text{rel}}(\zeta,\delta) = ||\bar{c}_f| - |\bar{c}_b||(|\bar{c}_f| + |\bar{c}_b|)^{-1}, \qquad N_{\text{width}}(\zeta,\delta) = |\lambda_f^{-1} - \lambda_b^{-1}|(\lambda_f^{-1} + \lambda_b^{-1})^{-1}, \tag{33}$$

where $\bar{c}_f$, $\bar{c}_b$, $\bar{\lambda}_f$ and $\bar{\lambda}_b$ are defined by Eqs. (26), (32), (21) and (29), respectively.

During the propagation of transition waves, the energy released by the phase transformation is transported through the lattice. Nonreciprocal energy transfer underlies the asymmetry of wave speeds in the forward and backward directions. To elucidate this mechanism in the active bistable lattice, we introduce a formal definition of the nonreciprocal energy difference given by

$$\Delta \bar{E} = \Big| |\bar{E}_f| - |\bar{E}_b| \Big|. \tag{34}$$

The asymmetry of kinetic flux carried by transition fronts originates from the fast-slow coupling between the configurational displacement $\bar{u}$ and the recovery variable $\bar{s}$. A propagating front converts a potential drop into kinetic transport while dissipating through viscous drag. The kinetic energy per density transported at the transition wave front consistently follows the following scaling relationship (Nadkarni et al., 2016b)

$$E_k = \tfrac{1}{2}\, c\, \eta^{-1} \Delta \mathcal{U}. \tag{35}$$

From the quartic on-site potential, and using the previously defined far-field stiffnesses $\bar{s}_f^0$ and $\bar{s}_b^0$, the initial energy gaps are (according to Eq. (5))

$$\Delta \bar{\mathcal{U}}^f = -\tfrac{4}{3\delta}(\bar{s}_f^0 - \bar{A}_1) < 0, \qquad \Delta \bar{\mathcal{U}}^b = -\tfrac{4}{3\delta}(\bar{s}_b^0 - \bar{A}_1) > 0, \tag{36}$$

so the forward front is energetically downhill whereas the backward front must overcome an active uphill barrier. Moreover, since $\partial|\Delta\bar{\mathcal{U}}|/\partial\bar{s} < 0$, the magnitudes $|\Delta\bar{\mathcal{U}}^f|$ and $\Delta\bar{\mathcal{U}}^b$ both decrease as the active stiffness increases. For $0 < \zeta \ll 1$, the effective kinetic energy is therefore bounded by the initial gaps. Consequently, $\bar{c}_f < \bar{c}_f^0 < 1$ and $|\bar{c}_b| < |\bar{c}_b^0| < 1$.

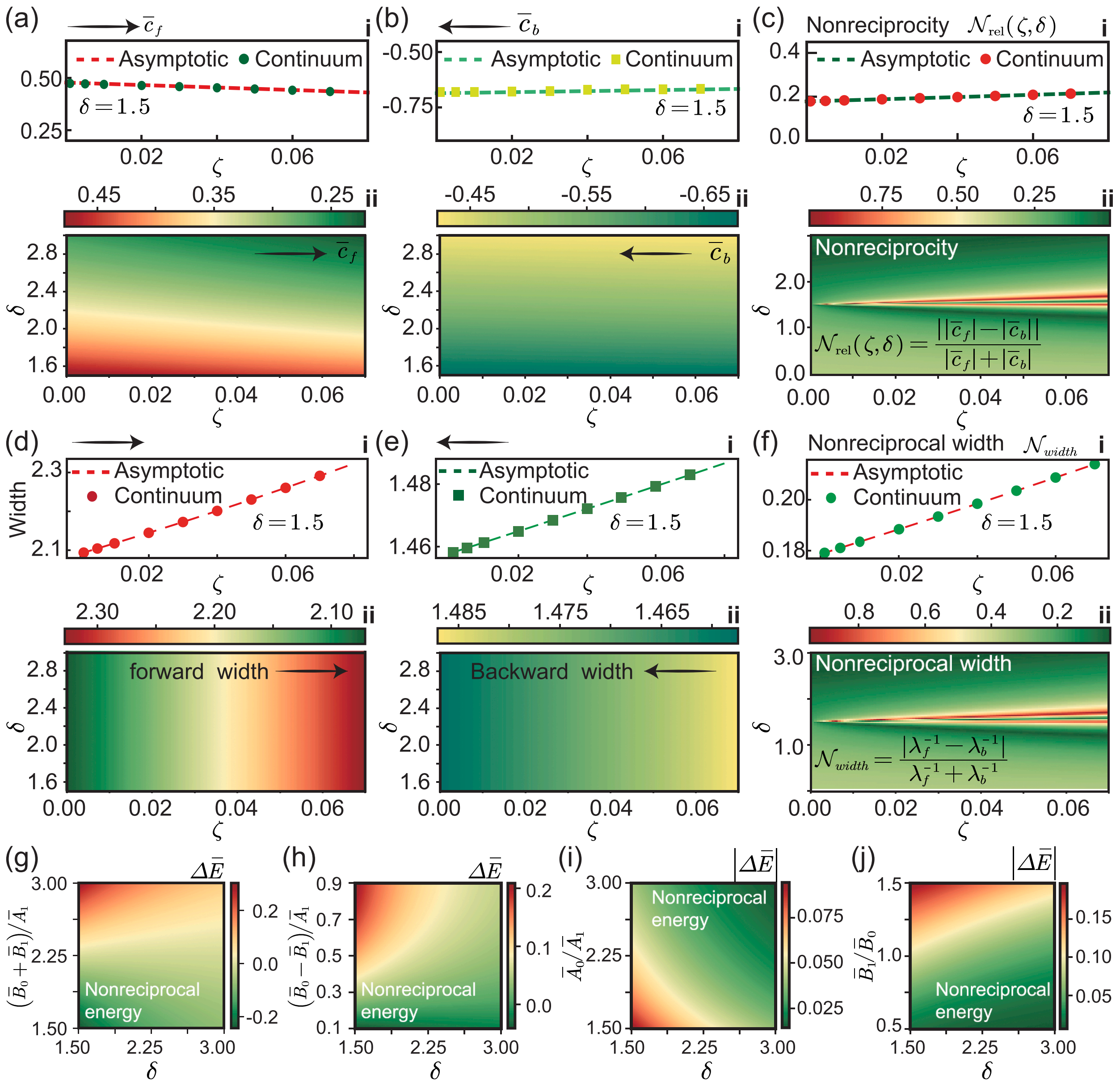

Fig. 5. Dynamic nonreciprocity and nonreciprocal energy transmission in active self-resetting lattices. (a)-(c) Forward dimensionless wave speed (a), backward dimensionless wave speed (b) and the nonreciprocity (c) in the active bistable lattice over the parameter domain of ζ and δ. (d)-(f) Forward wave width (d), backward wave width (e) and the width nonreciprocity (f) in the active bistable lattice over the parameter domain of ζ and δ. The perturbation solution was found to accurately describe both the forward and backward wave speeds and widths, as well as the nonreciprocity of the system with respect to wave speed and width. The nonreciprocity N_{rel} and the width nonreciprocity N_{width} of the active bistable lattice exhibit a complex nonlinear distribution over the parameter domain (ζ, δ). The region of strongest nonreciprocity is concentrated near $\delta = 1.5$ (excluding $\delta = 1.5$ itself), and the wave speed is much less sensitive to ζ than to δ, while the width shows the opposite behavior. (g)-(j) Variation of nonreciprocal energy transmission with δ and with $(\bar{B}_0 + \bar{B}_1)/\bar{A}_1$ (g), $(\bar{B}_0 - \bar{B}_1)/\bar{A}_1$ (h), $\bar{A}_0/\bar{A}_1$ (i) and $\bar{B}_0/\bar{B}_1$ (j), respectively. The nonreciprocity of energy transmission in active bistable lattices exhibits a localized distribution within the parameter domain and is concentrated at the boundary regions of the parameter space.

Substituting the perturbative speeds and the initial gaps into Eq. (35) yields the nonreciprocal energy difference

$$\Delta\bar{E} \approx \frac{1}{2}\left|\bar{c}_f|\Delta\bar{\mathcal{U}}^f| - |\bar{c}_b^0|\Delta\bar{\mathcal{U}}^b|\right|, \tag{37}$$

where all symbols in Eq. (37) are already determined by the perturbation analysis. This expression offers not only a mechanistic explanation of flux asymmetry but also a quantitative handle for designing nonreciprocal metamaterials with tunable energy transport properties.

Fig. 5 first presents the perturbation solutions for the speeds and widths of the forward and backward transition waves. Based on these results, the variations of the nonreciprocity $N_{\mathrm{rel}}(\zeta, \delta)$ and the width nonreciprocity $N_{\mathrm{width}}(\zeta, \delta)$ with respect to δ and ζ are obtained. We further provide the dependence of the nonreciprocal energy difference on the combinations of active-passive stiffness parameters $\bar{A}_0/\bar{A}_1$, $\bar{B}_1/\bar{B}_0$, $(\bar{B}_0+\bar{B}_1)/\bar{A}_1$ and $(\bar{B}_0-\bar{B}_1)/\bar{A}_1$ as well as on δ. Specifically, as shown in Fig. 5(a)i-(c)i, for $\delta = 1.5$, both the forward and backward dimensionless wave speeds, $\bar{c}_f$ and $\bar{c}_b$, decrease as ζ increases to 0.08. The forward wave speed $\bar{c}_f$ lies in the range 0.375-0.5, whereas the magnitude of the backward wave speed $\bar{c}_b$ ranges from 0.625 to 0.75. Meanwhile, the nonreciprocity $N_{\mathrm{rel}}(\zeta, \delta)$ increases gradually. In Fig. 5(a)ii-(b)ii, we examine the variations of $\bar{c}_f$ and $\bar{c}_b$ in the parameter space (ζ, δ). The results indicate that the forward wave speed changes more rapidly with respect to ζ and δ than the backward wave. In contrast, the backward wave speed is more sensitive to δ than to ζ. This behavior suggests that $\bar{c}_b$ is governed primarily by the passive stiffness parameter $\bar{A}_0$ and $\bar{A}_1$. Consequently, it is only weakly influenced by the recovery rate of the active stiffness $\bar{s}_b$. When δ decreases to 1.5 and ζ approaches zero, the forward wave speed reaches its maximum 0.475 nonlinearly; when δ decreases to 1.5, the absolute value of the backward wave speed attains its maximum 0.675 approximately linearly.

As shown in Fig. 5(c)ii, the nonreciprocity of the active bistable lattice exhibits a complex nonlinear distribution over the parameter domain (ζ, δ). The region of the strongest nonreciprocity is concentrated near $\delta = 1.5$, excluding $\delta = 1.5$ itself. As ζ increases toward 0.07, the range of δ corresponding to the high-nonreciprocity regime broadens. This regime develops into ray-like structures that extend asymmetrically on both sides of $\delta = 1.5$. In Fig. 5(d)i-(f)i, the widths of both the forward and backward transition waves increase with ζ. Consequently, the width nonreciprocity $N_{\mathrm{width}}(\zeta, \delta)$ also increases. This trend arises because the forward and backward wave widths grow at different rates as ζ gradually increases from near zero. As shown in Fig. 5(d)ii-(e)ii, within the parameter domain (ζ, δ), the widths of both the forward and backward waves are essentially insensitive to δ. In contrast, as ζ increases to 0.07, the widths of the forward and backward waves grow approximately linearly, reaching maximum values of 2.325 and 1.4875, respectively. In Fig. 5(f)ii, the variation of the width nonreciprocity over the parameter domain (ζ, δ) is qualitatively similar to that of the nonreciprocity. This correspondence enables the simultaneous tuning of wave speed and width in the bistable lattice. The above results therefore provide a parameter map for controlling dynamic nonreciprocity in active bistable lattices.

Note that, although the forward and backward wave speeds defined by Eqs. (26) and (32), as well as the nonreciprocal energy difference defined by Eq. (36), involve complex parameter dependencies, they are effectively governed by a limited set of parameter combinations $\bar{A}_0/\bar{A}_1$, $\bar{B}_1/\bar{B}_0$, $(\bar{B}_0+\bar{B}_1)/\bar{A}_1$ and $(\bar{B}_0-\bar{B}_1)/\bar{A}_1$. As shown in Fig. 5(g) and (h), for $\bar{A}_0 = \bar{A}_1$, the nonreciprocal energy difference value reaches its extremum nonlinearly when the ratio of the initial active stiffness to the passive stiffness for the forward or backward wave is at its minimum or maximum. This result indicates that the nonreciprocity of the bistable lattice is strongest under these conditions. In addition, this regime requires δ to be minimal. The above variations reflect the influence of the relationship between active and passive stiffness on the system. In Fig. 5(i) and (j), the nonreciprocal energy difference values reach their extrema nonlinearly when the ratios $\bar{A}_0/\bar{A}_1$ and $\bar{B}_1/\bar{B}_0$ attain their minimum and maximum, respectively. This behavior indicates that the nonreciprocity of the bistable lattice is strongest under these conditions when $\bar{B}_0 \neq \bar{B}_1$ and $\bar{A}_0 \neq \bar{A}_1$. Unlike the previous two cases, when the nonreciprocal energy difference reaches its extremum, δ must also attain either its minimum or maximum value, consistent with the other two ratios. Notably, the observed variations in wave speed align closely with the predictions from the numerical results. Consequently, the maximum of the nonreciprocal energy difference $\Delta\bar{E}$ in the active bistable lattice exhibits a localized distribution within the parameter space defined by $\bar{A}_0/\bar{A}_1$, $\bar{B}_1/\bar{B}_0$, $(\bar{B}_0+\bar{B}_1)/\bar{A}_1$, $(\bar{B}_0-\bar{B}_1)/\bar{A}_1$ and δ, and is concentrated near the edges of the domain. To maximize the system nonreciprocity while ensuring successful initiation and propagation of both forward and backward transition waves, $\bar{B}_1/\bar{B}_0$, $(\bar{B}_0+\bar{B}_1)/\bar{A}_1$, $(\bar{B}_0-\bar{B}_1)/\bar{A}_1$ should be increased as much as $\bar{A}_0/\bar{A}_1$ and δ should be minimized as far as practicable. The analysis of the initial time is provided in Appendix H. In this section, unless otherwise specified, the following dimensionless parameter values are used by default: $\bar{A}_n = \bar{B}_n = 1$ $(n = 0, 1)$.

In summary, by employing analytical expressions for the wave speeds and widths, we characterize both the nonreciprocity and nonreciprocal energy transmission in the active bistable lattice. This analysis provides a parameter map for the controlled tuning of nonreciprocity in active bistable systems.

7. Conclusions and discussions

Insights into how biological systems achieve nonreciprocal energy transport and reversible state transitions through coupled fast-slow dynamics have long informed the design of intelligent synthetic materials. Passive bistable metamaterials are limited by irreversibility and a lack of tunability after fabrication. This study addresses the need for a unified analytical framework to describe the reversible tunable nonreciprocal transition waves in self-resetting active bistable lattices. To this end, we construct a two-variable coupled model that integrates a slow, energy-injection-modulated signal with intrinsic mechanical bistability. The resulting framework emulates the dynamics of biological excitable systems while remaining analytically tractable.

First, we establish the mathematical foundation by introducing a slow recovery variable governed by displacement-dependent dynamics. This mechanism encodes a memory wake that modulates the energy landscape in a history-dependent manner. The on-site potential comprises passive and active components in parallel, with active stiffness dynamically resetting the double-well structure. This absence of spatiotemporal reversal symmetry constitutes the fundamental origin of nonreciprocity and enables direction-dependent energy barriers. Second, we perform numerical simulations to visualize spatiotemporal dynamics of reversible nonreciprocal transition waves. Three distinct phases are identified during propagation. The intermediate phase forms a refractory zone that selectively suppresses returning waves. The numerical results reveal pronounced nonreciprocity, with forward and backward wave speeds differing significantly despite perfect geometric symmetry. The wave width also exhibits strong nonreciprocity, with forward and backward waves displaying distinct dependencies on the dimensionless recovery rate. Third, we derive the continuum description by taking the long-wavelength limit and introducing dimensionless variables. Validation against discrete simulations confirm excellent agreement across wide parameter ranges. The continuum framework enables systematic investigation revealing that recovery rate and active stiffness targets jointly control nonreciprocal response. We demonstrate position-controllable transition waves and multiple round-trip propagation cycles, showcasing programmable reversible operation without external resetting forces. Fourth, we develop a unified matched-asymptotics framework for forward and backward propagating waves by exploiting singular perturbation structure. At leading order, active stiffness freezes and displacement admits a heteroclinic orbit connecting two stable states. And the final solutions are coupled with machine learning which provide accurate descriptions of both forward and backward waves. Speed selection emerges from coupled constraints including inner balance and far-field dispersion relation. Asymptotic solutions accurately reproduce numerical wave profiles and speeds, demonstrating that the recovery rate exhibits a nonlinear relationship with nonreciprocity. Fifth, we establish rigorous metrics to quantify nonreciprocal energy transport based on wave speed and width. Parameter space exploration reveals that nonreciprocal energy difference attains extrema when ratios of active to passive stiffness and potential-shape parameters reach their boundary values. These results provide explicit design maps that link microscopic parameters to macroscopic directional transport.

In summary, we have developed a comprehensive analytical framework for reversible nonreciprocal transition waves in active bistable lattices. The two-variable coupled model uncovers a fundamentally new mechanism for nonreciprocity arising from time-reversal symmetry breaking rather than spatial asymmetry. The slow recovery variable leaves a history-dependent memory wake that reshapes the energy landscape, enabling tunable nonreciprocal transition waves and transport in geometrically symmetric structures. Singular perturbation analysis coupling with machine learning yields analytical expressions for wave speed, width, and profiles, together with rigorous metrics for nonreciprocal energy flux.

The analytical tools developed here provide a powerful foundation for investigating more complex scenarios. The singular perturbation framework can be extended to systems with nonlinear recovery kinetics, multistable potentials, and higher-dimensional lattices (Schaeffer and Ruzzene, 2015; Shan et al., 2015). We envision that the theoretical principles established here will elucidate reversible wave propagation in active mechanical metamaterials for adaptive structures and soft robotics, phase-change materials where phase transitions induce macroscopic volumetric changes, and multifunctional materials subjected to coupled fields (Zheng et al., 2024; Shi et al., 2025; Shan et al., 2025; Sun et al., 2011; Wang et al., 2024b). Future directions include experimental realization using shape-memory alloys (Kellaris et al., 2018; Liang et al., 2022; Ni et al., 2023), electroactive polymers (Terzic et al., 2019; Xu et al., 2025), or magneto-rheological elastomers (Lou et al., 2025; Yan et al., 2021) with feedback control, exploration of wave interactions in the presence of refractory zones, and extension to stochastic and spatially heterogeneous active media. From an experimental perspective, the idealized lumped mass-spring chain considered here could be realized as a planar or additively manufactured lattice. In such a system, rigid blocks or reinforced nodes serve as the masses, while slender curved or pre-buckled beams function as the passive bistable springs. Active stiffness modulation can be incorporated by integrating shape-memory alloy wires, electroactive polymer bands, or magneto-responsive elastomer segments in parallel with these ligaments. Their activation can then be controlled using electrical or magnetic stimuli. A table-top prototype comprising a finite number of units would enable direct measurement of forward and backward transition waves and allow experimental quantification of nonreciprocal energy transport. Such a setup would directly link the present theoretical framework to practical active mechanical metamaterial devices. The integration of activity, reversibility, and nonreciprocity provides a pathway toward next-generation intelligent materials that bridge biological principles with engineered systems.

CRediT authorship contribution statement

Yao Zhang: Writing – review & editing, Writing – original draft, Visualization, Validation, Software, Methodology, Investigation, Formal analysis, Data curation, Conceptualization; **Chengxuan Zhai:** Writing – original draft, Validation, Investigation, Formal analysis, Data curation; **Zhanfeng Li:** Writing – original draft, Methodology, Investigation; **Jiahao Li:** Writing – original draft, Investigation, Formal analysis; **Guangjin Mou:** Writing – original draft, Software, Investigation, Formal analysis; **Lizichen Chen:** Writing – original draft, Investigation; **Yangkun Du:** Writing – original draft, Investigation, Funding acquisition, Formal analysis; **Michel Destrade:** Writing – original draft, Methodology, Investigation; **Changguo Wang:** Writing – original draft, Supervision, Resources, Project administration, Methodology, Funding acquisition; **Yafei Wang:** Writing – review & editing, Writing – original draft, Visualization, Validation, Supervision, Software, Resources, Project administration, Methodology, Investigation, Funding acquisition, Formal analysis, Conceptualization.

Data availability

Data will be made available on request.

Declaration of competing interest

The authors declare that they have no known competing financial interests or personal relationships that could have appeared to influence the work reported in this paper.

Acknowledgments

This work was supported by the National Natural Science Foundation of China (Grant Nos. 12202105 and 12572074), the Shenzhen Basic Research Program (Grant No. JCYJ20240813094159001), and the Shenzhou Young Scholars Fund of Harbin Institute of Technology. The authors sincerely thank Michel Destrade for his careful linguistic revision of the manuscript and for many constructive discussions.

Supplementary material

Supplementary material associated with this article can be found in the online version at 10.1016/j.jmps.2026.106697.

Appendix A. Discrete model

To establish the mathematical foundation for the analytical results, we present the detailed formulation of the discrete model. The restoring force model of the active bistable unit is given by Eq. (1) as follows

$$\begin{aligned} f_i(u_i;s_i) &= \partial_{u_i}\mathscr{U}_i(u_i;s_i) \\ &= \left(u_i^2-L^2\right)\left(s_i+A_0\right)u_i + L\delta^{-1}\left(u_i^2-L^2\right)\left(s_i-A_1\right) \\ &= \left(u_i^2-L^2\right)\left(\left(s_i+A_0\right)u_i + L\delta^{-1}\left(s_i-A_1\right)\right), \end{aligned} \tag{A.1}$$

where $A_0>0$, $A_1>0$, $L>0$ and $\delta>0$. The benchmark passive stiffness, A_0, characterizes the symmetric component of the bistable energy potential well. It represents the energetic contribution of passive material components that are independent of activity in active structures such as sarcomeres. The reference passive stiffness, A_1, controls the symmetry of the bistable energy potential well. It corresponds to the asymmetric energy contribution of passive materials in active structures. The bistable displacement scale, L, is defined as the distance between two stable equilibrium points. It measures the actual bistable displacement difference of the coarse-grained sarcomere unit. The shape parameter, δ, controls the degree of asymmetry of the bistable potential energy and the location of the potential barrier. It is used to fine-tune the accuracy of the phenomenological model. The restoring dynamics model of the active stiffness is defined by Eq. (2) as follows

$$\dot{s}_i = \xi\left(B_0 - s_i - B_1L^{-1}u_i\right) = -\xi\left(s_i - B_0 + B_1L^{-1}u_i\right), \tag{A.2}$$

where ξ denotes the energy input rate, while B_0 and B_1 are constants. The parameter ξ sets the time scale of energy injection into the system. It characterizes the rate of external energy uptake by active structures, such as muscles. The constants B_0 and B_1 govern respectively the baseline recovery level and the sensitivity to fast deformation.

Eqs. (A.1) and (A.2) together constitute the key restoring force equations of the bivariate coupled system. Next, through detailed derivations, we progressively establish the governing equations of the discrete system. First, the generalized Euler-Lagrange equation (see Eqs. (6)-(8)) of the discrete system is expressed as follows

$$\frac{\mathrm{d}}{\mathrm{d}t}\left(\partial_{\dot{u}_i}\mathscr{L}\right) - \partial_{u_i}\mathscr{L} = -\partial_{\dot{u}_i}\mathscr{R}, \tag{A.3}$$

where the Lagrangian is

$$\mathscr{L} = T - V_{\text{total}} = T - V_{\text{spr}} - V_{\text{on}} = \sum_{i=1}^{N}\frac{m}{2}\dot{u}_i^2 - \sum_{i=1}^{N-1}\frac{k}{2}(\nabla_d u)_i^2 - \sum_{i=1}^{N}\mathscr{U}_i(u_i;s_i), \tag{A.4}$$

T denotes the kinetic energy, V_{spr} is the nearest neighbor spring interaction, V_{on} is the on-site bistable contribution and V_{total} represents the total potential energy. Define the forward difference $(\nabla_d u)_i = u_{i+1}-u_i$ and the discrete Laplacian $(\Delta_d u)_i = u_{i+1}-2u_i+u_{i-1}$. The Rayleigh dissipation is defined as

$$\mathscr{R} = \sum_{i=1}^{N}\frac{\eta}{2}\dot{u}_i^2, \qquad \eta>0. \tag{A.5}$$

We find that only the kinetic energy and the Rayleigh dissipation are functions of $\dot{u}_i$, while V_{spr} and V_{on} are functions of u_i, with V_{on} not involved in the specific partial derivative simplifications. Substituting Eqs. (A.4) and (A.5) into Eq. (A.3), we obtain

$$m\ddot{u}_i - k(\Delta_d u)_i + f_i(u_i;s_i) = -\eta\dot{u}_i, \qquad i=1,2,\ldots,N, \tag{A.6}$$

where $\partial_{u_i}(\nabla_d u)_i = -(\Delta_d u)_i$, $f_i(u_i;s_i) = \partial_{u_i}\mathscr{U}_i(u_i;s_i)$ and $\partial_{\dot{u}_i}\mathscr{R} = \eta\dot{u}_i$. By further performing simple rearrangements on Eq. (A.7), one of the governing equations of the discrete system can be obtained, as shown in Eq. (9).

$$m\ddot{u}_i + \eta\dot{u}_i = k(\Delta_d u)_i - f_i(u_i;s_i), \qquad i=1,2,\ldots,N. \tag{A.7}$$

Substituting Eq. (A.1) into Eq. (A.7), we obtain

$$m\ddot{u}_i + \eta\dot{u}_i + (u_i^2-L^2)(s_i+A_0)u_i + L\delta^{-1}(u_i^2-L^2)(s_i-A_1) - k(\Delta_d u)_i = 0, \qquad i=1,2,\ldots,N, \tag{A.8}$$

and we keep Eq. (A.2) unchanged. Eqs. (A.2) and (A.8) together constitute the governing equations of the discrete system.

The parameters in the model can be correlated through common mechanical tests, thereby enabling our model to be directly applied to quantitatively predict the dynamical characteristics of relevant biological systems. The positions of bistability can be determined by measuring the force-displacement curve of the bistable unit (Raney et al., 2016). Therefore, for the coarse-grained sarcomere model we constructed, this method can also be used to measure the distance $2L$ between the two coarse-grained stable configurations. The equation $A_0 + s_i = (k_+ + k_-)/4L^2$ is obtained by the local tangent stiffness according to Eq. (A.1) (i.e., Eq. (1)): $k_+ = (\partial^2 \mathcal{U}_i/\partial u_i^2)|_{u_i=L} = 2L^2(A_0 + s_i + \delta^{-1}(s_i - A_1))$ and $k_- = (\partial^2 \mathcal{U}_i/\partial u_i^2)|_{u_i=-L} = 2L^2(A_0 + s_i - \delta^{-1}(s_i - A_1))$. To obtain the local target stiffness, we need to measure the Young's modulus. And the Young's modulus of single muscle fibers can be measured by atomic force microscopy (AFM) (Ogneva et al., 2010). In this way, the associated measured value of A_0 can be obtained under the condition of temporary deactivation by $k_\pm = (A_c/l)E_\pm$, where A_c is the cross-sectional area of the coarse-grained unit, l is the unit length and $E_\pm$ are the Young's modulus.

A_1 can be calculated through Eq. (36) , that is, the magnitude of A_1 is equal to the magnitude of the active stiffness when the energy difference between the two steady states is zero (Pal and Sitti, 2023). According to Eq. (4) in the manuscript, the unstable point of the bistable potential energy is located at $u^M = (A_1 - s_i)(A_0 + s_i)^{-1} L\delta^{-1}$. Therefore, on the basis of experimentally measured L, A_0, and A_1, it is necessary to measure the force-displacement curve of the sarcomere and determine the position of the unstable point. This procedure then yields the measured value of δ (Pal and Sitti, 2023).

When u_i does not change temporarily, according to Eq. (3), we can obtain: $s_i(t) = B_0 - B_1 L^{-1} u_i + [s_i(0) - B_0 + B_1 L^{-1} u_i]e^{-\xi t}$. ξ can be directly obtained by fitting the exponential recovery curve (Buonfiglio et al., 2024). When the displacement is equal to L and $-L$, respectively, the target values of the active stiffness are $B_0 - B_1$ and $B_0 + B_1$, respectively. B_0 is the average value of the target active stiffness , while B_1 is half of the difference between the two target values. Therefore, the measured value of B_0 and B_1 can be obtained by measuring the active stiffness at the two steady states (Song et al., 2021).

The previous study has shown that the thin filament in the half-sarcomere contains 90 nodes, with each minimal unit accounting for 1.108% of the total length (Fenwick et al., 2021). This provides a reliable basis for selecting model parameters when similar active systems, such as muscles, are considered. Specifically, the mass spacing and total system length can be prescribed according to the physical characteristics of the system under study, thereby determining the number of masses N.

To extend the applicability of the discrete model, we nondimensionalize it as follows:

Substituting $(\Delta_d u)_i = u_{i+1} - 2u_i + u_{i-1}$ into Eq. (A.8) yields:

$$m\ddot{u}_i + \eta\dot{u}_i + (u_i^2 - L^2)((s_i + A_0)u_i + L\delta^{-1}(s_i - A_1)) - k(u_{i+1} - 2u_i + u_{i-1}) = 0. \tag{A.9}$$

By setting $u_{i+1} = U_D U_{i+1}$, $u_i = U_D U_i$, $u_{i-1} = U_D U_{i-1}$ and $s_i = S_D S_i$, we obtain

$$\begin{aligned} &mU_D\ddot{U}_i + \eta U_D\dot{U}_i + ((U_D U_i)^2 - L^2)((S_D S_i + A_0)U_D U_i + L\delta^{-1}(S_D S_i - A_1)) \\ &- k(U_D U_{i+1} - 2U_D U_i + U_D U_{i-1}) = 0, \end{aligned} \tag{A.10}$$

and Eq. (A.2) becomes

$$S_D\dot{S}_i + \xi(S_D S_i - B_0 + B_1 L^{-1} U_D U_i) = 0. \tag{A.11}$$

Let $U_D = L$ and divide both sides of Eq. (A.10) by U_D, we have

$$\begin{aligned} &m\ddot{U}_i + \eta\dot{U}_i + U_D^2(U_i^2 - 1)((S_D S_i + A_0)U_i + \delta^{-1}(S_D S_i - A_1)) \\ &- k\left(U_{i+1} - 2U_i + U_{i-1}\right) = 0, \end{aligned} \tag{A.12}$$

and

$$S_D\dot{S}_i + \xi(S_D S_i - B_0 + B_1 U_i) = 0. \tag{A.13}$$

Next, by normalizing the parameters $\hat{A}_n = A_n/S_D$ and $\hat{B}_n = B_n/S_D$, where $n = 0, 1$, we obtain:

$$\begin{aligned} &m\ddot{U}_i + \eta\dot{U}_i + U_D^2(U_i^2 - 1)((S_D S_i + S_D\hat{A}_0)U_i + \delta^{-1}(S_D S_i - S_D\hat{A}_1)) \\ &- k(U_{i+1} - 2U_i + U_{i-1}) = 0, \end{aligned} \tag{A.14}$$

and

$$S_D\dot{S}_i + \xi(S_D S_i - S_D\hat{B}_0 + S_D\hat{B}_1 U_i) = 0. \tag{A.15}$$

Eqs. (A.14) and (A.15) simplify to

$$\begin{aligned} &m\ddot{U}_i + \eta\dot{U}_i + U_D^2 S_D(U_i^2 - 1)((S_i + \hat{A}_0)U_i + \delta^{-1}(S_i - \hat{A}_1)) \\ &- k\left(U_{i+1} - 2U_i + U_{i-1}\right) = 0, \end{aligned} \tag{A.16}$$

and

$$\dot{S}_i + \xi(S_i - \hat{B}_0 + \hat{B}_1 U_i) = 0. \tag{A.17}$$

By setting $\hat{t} = t/\hat{T}$, we have

$$\begin{aligned} &m\hat{T}^{-2}\ddot{U}_i + \eta\hat{T}^{-1}\dot{U}_i + U_D^2 S_D(U_i^2 - 1)((S_i + \hat{A}_0)U_i + \delta^{-1}(S_i - \hat{A}_1)) \\ &- k(U_{i+1} - 2U_i + U_{i-1}) = 0, \end{aligned} \tag{A.18}$$

and

$$\hat{T}^{-1}\dot{S}_i + \xi(S_i - \hat{B}_0 + \hat{B}_1 U_i) = 0. \tag{A.19}$$

Setting $\hat{T} = m/\eta$, $k = m/\hat{T}^2$ and $S_D = \eta^2/(U_D^2 m)$, yields

$$\ddot{U}_i + \dot{U}_i + (U_i^2 - 1)((S_i + \hat{A}_0)U_i + \delta^{-1}(S_i - \hat{A}_1)) - (U_{i+1} - 2U_i + U_{i-1}) = 0, \tag{A.20}$$

and

$$\dot{S}_i + \hat{\xi}(S_i - \hat{B}_0 + \hat{B}_1 U_i) = 0. \tag{A.21}$$

Eqs. (A.20) and (A.21) are the dimensionless discrete model with two-variable coupling.

Appendix B. Continuous model

We take the limit $N \to \infty$, and therefore we have $a \to \mathrm{d}x$, $u_i(t) \to u(x,t)$ and $s_i(t) \to s(x,t)$. We then substitute the above transformation into the following expansion (see Eq. (10)) :

$$u\Big|_{x=(i\pm1)a} = u(x = ia) \pm a\,u_x\Big|_{x=ia} + \frac{a^2}{2}\,u_{xx}\Big|_{x=ia} + \mathcal{O}(a^3), \tag{B.1}$$

and obtain (see Eq. (11))

$$u_{i\pm1} \;\to\; u(x,t) \pm a\,u_x(x,t) + \frac{a^2}{2}\,u_{xx}(x,t), \tag{B.2}$$

where $u_{i\pm1} = u(x_i \pm a, t)$ and we neglect higher-order infinitesimal terms. Substituting these parameter transformations together with Eq. (B.2) into Eq. (A.8), we obtain

$$m\ddot{u} - ka^2 u_{xx} + \eta\dot{u} + (u^2 - L^2)\big((s + A_0)u + (s - A_1)L\delta^{-1}\big) = 0. \tag{B.3}$$

Next, to improve the accuracy of the continuous model, we perform parameter scalings as $\rho = m/a$, $k' = ka$, and $\eta' = \eta/a$ such that the macroscopic parameters of the system remain $\mathcal{O}(1)$. Dividing both sides of Eq. (B.3) by a, we obtain

$$ma^{-1}\ddot{u} - kau_{xx} + \eta a^{-1}\dot{u} + a^{-1}(u^2 - L^2)\big((s + A_0)u + (s - A_1)L\delta^{-1}\big) = 0. \tag{B.4}$$

We find that the parameters in Eq. (1) can be replaced by the new parameter combinations introduced above, then we have (see Eq. (12))

$$\rho\,\ddot{u} - k'\,u_{xx} + \eta'\,\dot{u} + a^{-1}(u^2 - L^2)\big((s + A_0)u + (s - A_1)L\delta^{-1}\big) = 0, \tag{B.5}$$

and Eq. (A.2) becomes (see Eq. (13))

$$\dot{s} + \xi\,(s - B_0 + B_1 L^{-1} u) = 0. \tag{B.6}$$

To simplify the governing equations, we introduce dimensionless variables by setting $\bar{x} = x/X$, $\bar{t} = t/T$, $\bar{u} = u/U$, and $\bar{s} = s/S$, and normalize the stiffness parameters as $\bar{A}_n = A_n/S$ and $\bar{B}_n = B_n/S$, where $n = 0, 1$. Substituting all the transformations into Eqs. (B.5) and (B.6), we have

$$\rho\,UT^{-2}\ddot{\bar{u}} - k'\,UX^{-2}\bar{u}_{xx} + \eta'\,UT^{-1}\dot{\bar{u}} + a^{-1}(U^2\bar{u}^2 - L^2)\big((S\bar{s} + S\bar{A}_0)U\bar{u} + (S\bar{s} - S\bar{A}_1)L\delta^{-1}\big) = 0, \tag{B.7}$$

and

$$ST^{-1}\dot{\bar{s}} + \xi\,(S\bar{s} - S\bar{B}_0 + S\bar{B}_1 L^{-1} U\bar{u}) = 0. \tag{B.8}$$

Setting $U = L$, Eqs. (B.7) and (B.8) simplify to

$$\rho\,T^{-2}\ddot{\bar{u}} - k'\,X^{-2}\bar{u}_{xx} + \eta'\,T^{-1}\dot{\bar{u}} + a^{-1}U^2 S(\bar{u}^2 - 1)\big((\bar{s} + \bar{A}_0)\bar{u} + (\bar{s} - \bar{A}_1)\delta^{-1}\big) = 0, \tag{B.9}$$

and

$$\dot{\bar{s}} + \xi\,T(\bar{s} - \bar{B}_0 + \bar{B}_1\bar{u}) = 0, \tag{B.10}$$

then setting $X^2 = k'T^2/\rho$, $T = \rho/\eta'$, $S = a\eta'^2/(\rho U^2)$ and $\zeta = \xi T$, we have (see Eqs. (14) and (15))

$$\ddot{\bar{u}} - \bar{u}_{\bar{x}\bar{x}} + \dot{\bar{u}} + (\bar{u}^2 - 1)\big((\bar{s} + \bar{A}_0)\bar{u} + (\bar{s} - \bar{A}_1)\delta^{-1}\big) = 0, \tag{B.11}$$

and

$$\dot{\bar{s}} + \zeta\,(\bar{s} - \bar{B}_0 + \bar{B}_1\bar{u}) = 0. \tag{B.12}$$

Eqs. (B.11) and (B.12) constitute the nondimensional governing equations of the active bistable continuum system.

Appendix C. Boundary-layer matching theory

We introduce the traveling wave coordinate (see Eq. (16))

$$\begin{aligned} z &= \begin{cases} z = \bar{x} - \bar{c}_f \bar{t}, & \bar{x} \in \mathbb{R}^+ \text{ and } \bar{c}_f > 0, \\ z = |\bar{c}_b|\bar{t} - \bar{x}, & \bar{x} \in \mathbb{R}^- \text{ and } \bar{c}_b < 0, \end{cases} \\ &= H(\bar{x})\big(\bar{x} - \bar{c}_f \bar{t}\big) + \big(1 - H(\bar{x})\big)\big(|\bar{c}_b|\bar{t} - \bar{x}\big). \end{aligned} \tag{C.1}$$

where $H(\cdot)$ denotes the Heaviside step function, i.e. $H(x) = 1$ for $x > 0$ and $H(x) = 0$ for $x < 0$. Substituting the forward traveling-wave coordinate into Eqs. (B.11) and (B.12), we obtain

$$\begin{aligned} &\bar{u}_{\bar{t}\bar{t}} - \bar{u}_{\bar{x}\bar{x}} + \bar{u}_{\bar{t}} + (\bar{u}^2 - 1)((\bar{s} + \bar{A}_0)\bar{u} + (\bar{s} - \bar{A}_1)\delta^{-1}) = 0 \\ \Leftrightarrow &(\bar{c}_f)^2 \bar{u}_f'' - \bar{u}_f'' - \bar{c}_f \bar{u}_f' + (\bar{u}_f^2 - 1)((\bar{s}_f + \bar{A}_0)\bar{u}_f + (\bar{s}_f - \bar{A}_1)\delta^{-1}) = 0 \\ \Leftrightarrow &((\bar{c}_f)^2 - 1)\bar{u}_f'' - \bar{c}_f \bar{u}_f' + (\bar{u}_f^2 - 1)((\bar{s}_f + \bar{A}_0)\bar{u}_f + (\bar{s}_f - \bar{A}_1)\delta^{-1}) = 0, \end{aligned} \tag{C.2}$$

and

$$\begin{aligned} &\bar{s}_{\bar{t}} + \zeta(\bar{s} - \bar{B}_0 + \bar{B}_1 \bar{u}) = 0, \\ \Leftrightarrow &- \bar{c}_f \bar{s}_f' + \zeta(\bar{s}_f - \bar{B}_0 + \bar{B}_1 \bar{u}_f) = 0, \\ \Leftrightarrow &\bar{c}_f \bar{s}_f' + \zeta(\bar{B}_0 - \bar{B}_1 \bar{u}_f - \bar{s}_f) = 0. \end{aligned} \tag{C.3}$$

Meanwhile, considering $0 < \bar{c}_f < 1$, the equation can be further simplified as (see Eqs. (17) and (18))

$$\bar{u}_f'' - \bar{c}_f(\bar{c}_f^2 - 1)^{-1}\,\bar{u}_f' + (\bar{c}_f^2 - 1)^{-1}(\bar{u}_f^2 - 1)((\bar{s}_f + \bar{A}_0)\,\bar{u}_f + (\bar{s}_f - \bar{A}_1)\delta^{-1}) = 0, \tag{C.4}$$

and

$$\bar{s}_f' + \zeta \bar{c}_f^{-1}(\bar{B}_0 - \bar{B}_1 \bar{u}_f - \bar{s}_f) = 0, \tag{C.5}$$

where $\bar{u}_f(z) = \bar{u}(\bar{x}, \bar{t})$ and $\bar{s}_f(z) = \bar{s}(\bar{x}, \bar{t})$. The first-order expansions of the field and wave speed are given by (see Eq. (19))

$$\bar{u}_f = \bar{u}_f^0 + \zeta\,\bar{u}_f^1 + \mathcal{O}(\zeta^2), \quad \bar{s}_f = \bar{s}_f^0 + \zeta\,\bar{s}_f^1 + \mathcal{O}(\zeta^2), \quad \bar{c}_f = \bar{c}_f^0 + \zeta\,\bar{c}_f^1 + \mathcal{O}(\zeta^2), \tag{C.6}$$

To obtain the zeroth-order solution, we substitute Eq. (C.6) ($\zeta = 0$) into Eqs. (C.4) and (C.5) and obtain

$$(\bar{u}_f^0)'' - \bar{c}_f^0((\bar{c}_f^0)^2 - 1)^{-1}\,(\bar{u}_f^0)' + ((\bar{c}_f^0)^2 - 1)^{-1}((\bar{u}_f^0)^2 - 1)((\bar{s}_f^0 + \bar{A}_0)\,\bar{u}_f^0 + (\bar{s}_f^0 - \bar{A}_1)\delta^{-1}) = 0 \tag{C.7}$$

and

$$(\bar{s}_f^0)' = 0. \tag{C.8}$$

The solution of this system of equations (see Eqs. (20)-(22)) is

$$\bar{u}_f^0(z) = -\tanh(\lambda_f^0 z), \qquad \lambda_f^0 = \Big(\tfrac{1}{2}(\bar{A}_0 + \bar{s}_f^0) + (\bar{s}_f^0 - \bar{A}_1)^2\,\delta^{-2}\Big)^{1/2}, \qquad \bar{c}_f^0 = \Big(1 + \tfrac{1}{2}\delta^2(\bar{A}_0 + \bar{s}_f^0)(\bar{s}_f^0 - \bar{A}_1)^{-2}\Big)^{-1/2}, \tag{C.9}$$

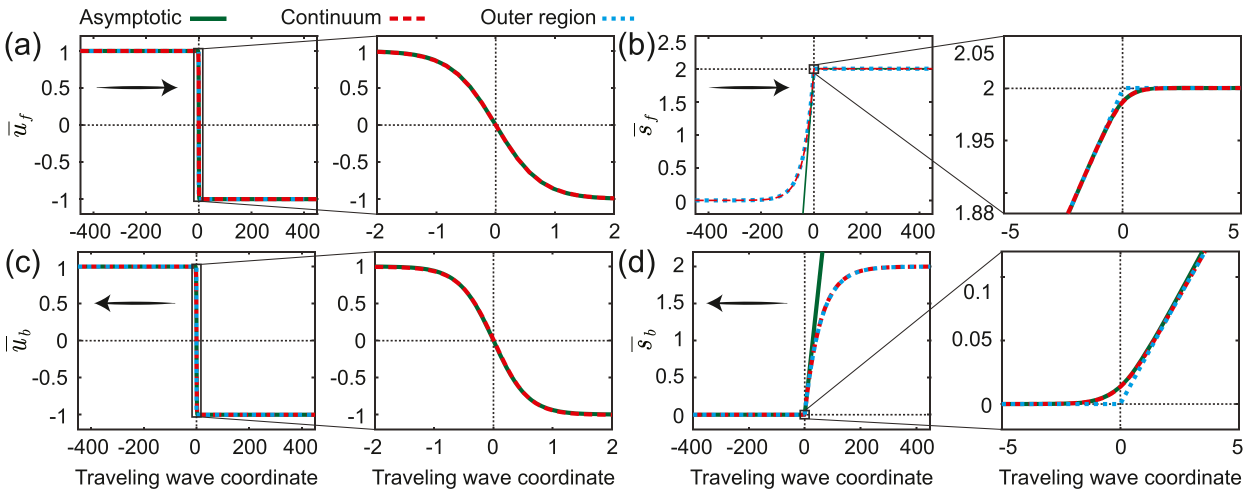

Fig. C.1. Asymptotic solutions for the inner and outer regions of mechanical and active waves. (a) Waveform of $\bar{u}_f$. (b)Waveform of $\bar{s}_f$. (c) Waveform of $\bar{u}_b$. (d) Waveform of $\bar{s}_b$. The green line represents the asymptotic solution in the inner region, the red dashed line represents the numerical solution of the dimensionless continuum model, and the blue line represents the solution in the outer region. The parameters: $\bar{A}_n = \bar{B}_n = 1$ ($n = 0, 1$), $\delta = 2$ and $\zeta = 0.01$.

where $\bar{s}_f^0 = \bar{B}_0 + \bar{B}_1$ which is determined by the initial condition. To further solve the first-order term, we substitute Eq. (C.6) into Eq. (C.5) to get

$$\begin{aligned}
&(\bar{s}_f^0)' + \zeta(\bar{s}_f^1)' + \zeta(\bar{B}_0 - \bar{B}_1\bar{u}_f^0 - \bar{B}_1\bar{u}_f^1\zeta - \bar{s}_f^0 - \bar{s}_f^1\zeta)(\left(\bar{c}_f^0\right)^{-1} - \bar{c}_f^1\left(\bar{c}_f^0\right)^{-2}\zeta) + \mathcal{O}(\zeta^2) = 0, \\
\Leftrightarrow &(\bar{s}_f^0)' + \zeta(\bar{s}_f^1)' + \zeta\left(\bar{c}_f^0\right)^{-1}(\bar{B}_0 - \bar{B}_1\bar{u}_f^0 - \bar{s}_f^0) + \mathcal{O}(\zeta^2) = 0, \\
\Leftrightarrow &(\bar{s}_f^0)' + \zeta((\bar{s}_f^1)' + \left(\bar{c}_f^0\right)^{-1}(\bar{B}_0 - \bar{B}_1\bar{u}_f^0 - \bar{s}_f^0)) + \mathcal{O}(\zeta^2) = 0.
\end{aligned} \tag{C.10}$$

The $\mathcal{O}(\zeta)$ term in Eq. (C.10) can be directly integrated. We thus consider

$$(\bar{s}_f^1)' + \left(\bar{c}_f^0\right)^{-1}(\bar{B}_0 - \bar{B}_1\bar{u}_f^0 - \bar{s}_f^0) = 0, \tag{C.11}$$

which yields (see Eq. (23))

$$\bar{s}_f^1(z) = -\bar{B}_1(\bar{c}_f^0\lambda_f^0)^{-1}\left(\ln(\cosh(\lambda_f^0 z)) - \lambda_f^0 z + \alpha_1\right), \tag{C.12}$$

where α_1 is to be determined by matching solutions in the intermediate and the outer regions on both sides to $\mathcal{O}(\zeta)$. In Fig. C.1, the waveform solutions in the traveling-wave coordinate exhibit distinct profiles between the two scales $z \sim \mathcal{O}(\zeta^{-1})$ and $z \sim \mathcal{O}((\lambda_f^0)^{-1})$, which originate from the difference in time scales induced by the fast-slow dynamics. Therefore, we define the coordinate $Z = \zeta z,\ z \sim \mathcal{O}(\zeta^{-1})$ corresponding to the outer region. Meanwhile, Eqs. (C.4) and (C.5) are transformed as follows

$$\zeta^2\ \bar{U}_f'' - \zeta\bar{c}_f((\bar{c}_f)^2 - 1)^{-1}\ \bar{U}_f' + ((\bar{c}_f)^2 - 1)^{-1}((\bar{U}_f)^2 - 1)((\bar{S}_f + \bar{A}_0)\bar{U}_f + (\bar{S}_f - \bar{A}_1)\delta^{-1}) = 0, \tag{C.13}$$

and

$$\begin{aligned}
&\zeta\bar{S}_f' + \zeta\bar{c}_f^{-1}(\bar{B}_0 - \bar{B}_1\bar{U}_f - \bar{S}_f) = 0, \\
\Leftrightarrow &\bar{S}_f' + \bar{c}_f^{-1}(\bar{B}_0 - \bar{B}_1\bar{U}_f - \bar{S}_f) = 0,
\end{aligned} \tag{C.14}$$

where $\bar{U}_f(Z)$ and $\bar{S}_f(Z)$ are the solutions in these outer regions for $Z \sim \mathcal{O}(1)$. Evidently, for $\bar{U}_f(Z)$, we have

$$\bar{U}_f(Z) = \bar{u}_f^0(z) = -\tanh(\lambda_f^0 z) = -\tanh(\lambda_f^0\zeta^{-1}Z) \approx -\text{sign}(Z) = \begin{cases} \bar{U}_{f,L}(Z) = 1, & Z < 0, \\ \bar{U}_{f,R}(Z) = -1, & Z > 0, \end{cases} \tag{C.15}$$

where the subscript L denotes the left outer region, and R denotes the right outer region (the same applies below). Furthermore, we expand $\bar{S}_{f,L}(Z)$ as follows

$$\bar{S}_{f,L}(Z) = \bar{S}_{f,L}^0 + \bar{S}_{f,L}^1\zeta + \mathcal{O}(\zeta^2), \tag{C.16}$$

while $\bar{S}_{f,R}(Z) = \bar{B}_0 + \bar{B}_1, Z > 0$, which is defined by initial condition. Substituting Eqs. (C.15) and (C.16) into Eq. (C.14) yields

$$\begin{aligned}
&(\bar{S}_{f,L}^0)' + \zeta(\bar{S}_{f,L}^1)' \\
&\quad + ((\bar{c}_f^0)^{-1} - \zeta\bar{c}_f^1(\bar{c}_f^0)^{-2} + \mathcal{O}(\zeta^2))(\bar{B}_0 - \bar{B}_1 - \bar{S}_{f,L}^0 - \bar{S}_{f,L}^1\zeta + \mathcal{O}(\zeta^2)) = 0, \\
\Leftrightarrow &(\bar{S}_{f,L}^0)' + (\bar{c}_f^0)^{-1}(\bar{B}_0 - \bar{B}_1 - \bar{S}_{f,L}^0) \\
&\quad + \zeta((\bar{S}_{f,L}^1)' - (\bar{c}_f^0)^{-1}\bar{S}_{f,L}^1 - \bar{c}_f^1(\bar{c}_f^0)^{-2}(\bar{B}_0 - \bar{B}_1 - \bar{S}_{f,L}^0)) + \mathcal{O}(\zeta^2) = 0.
\end{aligned} \tag{C.17}$$

We first solve for the $\mathcal{O}(1)$ term of Eq. (17) as follows

$$(\bar{S}_{f,L}^0)' + (\bar{c}_f^0)^{-1}(\bar{B}_0 - \bar{B}_1 - \bar{S}_{f,L}^0) = 0, \quad \bar{S}_{f,L}^0(-\infty) = \bar{B}_0 - \bar{B}_1, \tag{C.18}$$

which yields

$$\bar{S}_{f,L}^0(Z) = \bar{B}_0 - \bar{B}_1 + \alpha_2\exp((\bar{c}_f^0)^{-1}Z), \tag{C.19}$$

where α_2 is the integration constant. Substituting Eq. (C.19) into the $\mathcal{O}(\zeta)$ term of Eq. (C.17) yields

$$(\bar{S}_{f,L}^1)' - (\bar{c}_f^0)^{-1}\bar{S}_{f,L}^1 - \bar{c}_f^1(\bar{c}_f^0)^{-2}(\bar{B}_0 - \bar{B}_1 - \bar{S}_{f,L}^0) = 0, \quad \bar{S}_{f,L}^1(-\infty) = 0, \tag{C.20}$$

which yields

$$\bar{S}_{f,L}^1(Z) = -\bar{c}_f^1(\bar{c}_f^0)^{-2}\alpha_2 Z\exp((\bar{c}_f^0)^{-1}Z) + \alpha_3\exp((\bar{c}_f^0)^{-1}Z), \tag{C.21}$$

where α_3 is the integration constant. Next, we apply boundary matching rules to match the inner and outer regions and determine the integration constants as follows

$$\begin{aligned}
&\lim_{\zeta\to 0}\bar{S}_{f,R} = \lim_{\zeta\to\infty}(\bar{s}_f^0(\zeta^{-1}Z) + \bar{s}_f^1(\zeta^{-1}Z)\zeta),\ \lim_{\zeta\to 0}\bar{S}_{f,L}^0 = \lim_{\zeta\to\infty}\bar{s}_f^0(\zeta^{-1}Z),\ \lim_{\zeta\to 0}\bar{S}_{f,L}^1\zeta = \lim_{\zeta\to\infty}\bar{s}_f^1(\zeta^{-1}Z)\zeta, \\
\Rightarrow &\alpha_1 = \ln 2,\ \alpha_2 = 2\bar{B}_1,\ \alpha_3 = 0, \\
\Rightarrow &\bar{S}_{f,L}(Z) = \bar{B}_0 - \bar{B}_1 + 2\bar{B}_1\exp((\bar{c}_f^0)^{-1}Z) + (-\bar{c}_f^1(\bar{c}_f^0)^{-2}2\bar{B}_1 Z\exp((\bar{c}_f^0)^{-1}Z))\zeta + \mathcal{O}(\zeta^2),
\end{aligned} \tag{C.22}$$

Meanwhile, owing to $\alpha_1 = \ln 2$, we obtain

$$\bar{s}_f = \bar{B}_0 + \bar{B}_1 - \zeta \bar{B}_1 (\bar{c}_f^0 \lambda_f^0)^{-1} \left(\ln(\cosh(\lambda_f^0 z)) - \lambda_f^0 z + \ln 2 \right) + \mathcal{O}(\zeta^2). \tag{C.23}$$

From this point, the expression of field $\bar{u}_f(z)$ and $\bar{s}_f(z)$ is obtained through a multiscale asymptotic expansion. We present the asymptotic matching results of the inner and outer regions for the forward and backward waves in Fig. C.1. The results indicate that the asymptotic solutions in both regions match well with the dimensionless continuum model within their respective ranges, but the matching performance is unsatisfactory in the transition region.

Appendix D. The integral condition and far-field theory

Based on Eq. (C.6) , we further expand the other parameter λ_f as follows

$$\lambda_f = \lambda_f^0 + \lambda_f^1 \zeta + \mathcal{O}(\zeta^2), \tag{D.1}$$

First, to obtain the integral condition as the first equation for solving the wave speed, we multiply both sides of Eq. (C.4) by $\bar{u}'_f$ and integrate over the entire domain as follows

$$\begin{aligned}
&\int_{-\infty}^{\infty} (\bar{u}''_f - \bar{c}_f(\bar{c}_f^2 - 1)^{-1}\bar{u}'_f + (\bar{c}_f^2 - 1)^{-1}(\bar{u}_f^2 - 1)((\bar{s}_f + \bar{A}_0)\,\bar{u}_f + (\bar{s}_f - \bar{A}_1)\delta^{-1}))\bar{u}'_f \mathrm{d}z = 0, \\
\Leftrightarrow &\int_{-\infty}^{\infty} \bar{u}''_f \bar{u}'_f \mathrm{d}z - \int_{-\infty}^{\infty} \bar{c}_f(\bar{c}_f^2 - 1)^{-1} \left(\bar{u}'_f\right)^2 \mathrm{d}z \\
&+ \left(\bar{c}_f^2 - 1\right)^{-1} \int_{-\infty}^{\infty} (\bar{u}_f^2 - 1)((\bar{s}_f + \bar{A}_0)\,\bar{u}_f + (\bar{s}_f - \bar{A}_1)\delta^{-1})\bar{u}'_f \mathrm{d}z = 0,
\end{aligned} \tag{D.2}$$

where

$$\int_{-\infty}^{\infty} \bar{u}''_f \bar{u}'_f \mathrm{d}z = \frac{1}{2}(\bar{u}'_f)^2 \mid_{-\infty}^{\infty} = 0, \tag{D.3}$$

and

$$\int_{-\infty}^{\infty} ((\bar{u}_f)^2 - 1)(\bar{A}_0 \bar{u}_f - \bar{A}_1 \delta^{-1})\bar{u}'_f \mathrm{d}z = -\bar{A}_1 \delta^{-1} \int_{-\infty}^{\infty} ((\bar{u}_f)^2 - 1)\bar{u}'_f \mathrm{d}z, \tag{D.4}$$

Substituting Eqs. (D.3) and (D.4) into Eq. (D.2) gives

$$\begin{aligned}
&\int_{-\infty}^{\infty} \bar{u}''_f \bar{u}'_f \mathrm{d}z - \int_{-\infty}^{\infty} \bar{c}_f(\bar{c}_f^2 - 1)^{-1} \left(\bar{u}'_f\right)^2 \mathrm{d}z \\
&+ \left(\bar{c}_f^2 - 1\right)^{-1} \left(\int_{-\infty}^{\infty} (\bar{u}_f^2 - 1)\bar{s}_f(\bar{u}_f + \delta^{-1})\bar{u}'_f \mathrm{d}z + \int_{-\infty}^{\infty} (\bar{u}_f^2 - 1)(\bar{A}_0 \bar{u}_f - \bar{A}_1 \delta^{-1})\bar{u}'_f \mathrm{d}z\right) = 0, \\
\Leftrightarrow &\frac{1}{2}(\bar{u}'_f)^2 \mid_{-\infty}^{\infty} - \int_{-\infty}^{\infty} \bar{c}_f(\bar{c}_f^2 - 1)^{-1} \left(\bar{u}'_f\right)^2 \mathrm{d}z \\
&+ \left(\bar{c}_f^2 - 1\right)^{-1} \left(\int_{-\infty}^{\infty} (\bar{u}_f^2 - 1)\bar{s}_f(\bar{u}_f + \delta^{-1})\bar{u}'_f \mathrm{d}z - \bar{A}_1 \delta^{-1} \int_{-\infty}^{\infty} ((\bar{u}_f)^2 - 1)\bar{u}'_f \mathrm{d}z\right) = 0, \\
\Leftrightarrow &\bar{c}_f \int_{-\infty}^{\infty} \left(\bar{u}'_f\right)^2 \mathrm{d}z + \bar{A}_1 \delta^{-1} \int_{-\infty}^{\infty} ((\bar{u}_f)^2 - 1)\bar{u}'_f \mathrm{d}z = \int_{-\infty}^{\infty} \bar{s}_f((\bar{u}_f)^2 - 1)(\bar{u}_f + \delta^{-1})\bar{u}'_f \mathrm{d}z.
\end{aligned} \tag{D.5}$$

According to Eqs. (C.6) and (C.9), we set $\bar{u}_f(z) \approx -\tanh(\lambda_f z)$; then Eq. (D.5) becomes

$$\begin{aligned}
&\bar{c}_f \int_{-\infty}^{\infty} \left(-\tanh'(\lambda_f z)\right)^2 \mathrm{d}z + \bar{A}_1 \delta^{-1} \int_{-\infty}^{\infty} ((-\tanh(\lambda_f z))^2 - 1)(-\tanh'(\lambda_f z))\mathrm{d}z \\
&= \int_{-\infty}^{\infty} \bar{s}_f((-\tanh(\lambda_f z))^2 - 1)(-\tanh(\lambda_f z) + \delta^{-1})(-\tanh'(\lambda_f z))\mathrm{d}z,
\end{aligned} \tag{D.6}$$

where $\bar{s}_f$ is defined by Eq. (C.23). Also, $-\tanh(\lambda_f z) = -\lambda_f \mathrm{sech}^2(\lambda_f z)$, $(-\tanh(\lambda_f z))^2 = \lambda_f^2 \mathrm{sech}^4(\lambda_f z)$ and $1 - \tanh^2(\lambda_f z) = \mathrm{sech}^2(\lambda_f z)$. Therefore, Eq. (D.6) simplifies to (see Eq. (24))

$$12\delta\left(\bar{c}_f \lambda_f\right)^2 - 12(\bar{s}_f^0 - \bar{A}_1)\bar{c}_f \lambda_f + (3\delta + 10)\bar{B}_1 \zeta = 0. \tag{D.7}$$

Next, in order to determine the wave speed, we require an additional equation. Here we propose the far-field expansion of the forward traveling wave solution as follows

$$\begin{aligned}
\bar{u}_f(z) &= -1 + 2\exp(-2\lambda_f z) + \mathcal{O}(\exp(-4\lambda_f z)) \\
&\approx -1 + 2\exp(-2\lambda_f z), \quad |z|^{-1} \ll 1,
\end{aligned} \tag{D.8}$$

which is found from setting $\bar{u}_f(z) = -\tanh(\lambda_f z) = (\exp(-2\lambda_f z) - 1)/(\exp(-2\lambda_f z) + 1)$. Substituting Eq. (D.8) into Eq. (C.5) yields

$$\begin{aligned}
&\bar{s}'_f + \zeta \bar{c}_f^{-1}(\bar{B}_0 - \bar{B}_1(-1 + 2\exp(-2\lambda_f z)) - \bar{s}_f) = 0, \\
\Leftrightarrow &\bar{s}'_f - \zeta \bar{c}_f^{-1}\bar{s}_f = -\zeta \bar{c}_f^{-1}(\bar{B}_0 + \bar{B}_1 - 2\bar{B}_1 \exp(-2\lambda_f z)),
\end{aligned} \tag{D.9}$$

which, subject to $\bar{s}_f(+\infty) = \bar{B}_0 + \bar{B}_1$, yields

$$\bar{s}_f(z) = \bar{B}_0 + \bar{B}_1 - (2\bar{B}_1\zeta(2\bar{c}_f\lambda + \zeta)^{-1})\exp(-2\lambda_f z). \tag{D.10}$$

Substituting Eq. (D.8) into Eq. (C.4) yields

$$\begin{aligned}&(-1+2\exp(-2\lambda_f z))'' - \bar{c}_f(\bar{c}_f^2-1)^{-1}(-1+2\exp(-2\lambda_f z))'\\&+(\bar{c}_f^2-1)^{-1}\left(\left(-1+2\exp(-2\lambda_f z)\right)^2-1\right)((\bar{s}_f+\bar{A}_0)(-1+2\exp(-2\lambda_f z))+(\bar{s}_f-\bar{A}_1)\delta^{-1})=0,\\ \Leftrightarrow&8\lambda_f^2\exp(-2\lambda_f z)+4\bar{c}_f\lambda_f(\bar{c}_f^2-1)^{-1}\exp(-2\lambda_f z)\\&+4(\bar{c}_f^2-1)^{-1}(\exp(-4\lambda_f z)-\exp(-2\lambda_f z))((\bar{s}_f+\bar{A}_0)(-1+2\exp(-2\lambda_f z))+(\bar{s}_f-\bar{A}_1)\delta^{-1})=0.\end{aligned} \tag{D.11}$$

Next, substituting Eq. (D.10) into Eq. (D.11) and omitting $\mathcal{O}(\exp(-4\lambda_f z))$, we obtain (see Eq. (25))

$$\begin{aligned}&4(2\lambda_f^2((\bar{c}_f)^2-1)+\bar{c}_f\lambda_f-(-(\bar{B}_0+\bar{B}_1+\bar{A}_0)+\delta^{-1}(\bar{B}_0+\bar{B}_1-\bar{A}_1)))\exp(-2\lambda_f z)=0,\\ \Leftrightarrow&2\lambda_f^2((\bar{c}_f)^2-1)+\bar{c}_f\lambda_f+\left[(\bar{B}_0+\bar{B}_1+\bar{A}_0)-\delta^{-1}(\bar{B}_0+\bar{B}_1-\bar{A}_1)\right]=0,\\ \Leftrightarrow&2\delta\lambda_f^2-2\delta\lambda_f^2\bar{c}_f^2-\delta\bar{c}_f\lambda_f-(\delta-1)\bar{s}_f^0-\delta\bar{A}_0-\bar{A}_1=0.\end{aligned} \tag{D.12}$$

Finally, substituting the expansions of $\bar{c}_f$ and λ_f into Eqs. (D.7) and (D.12) gives

$$\begin{aligned}&12\delta\left(\bar{c}_f^0+\zeta\,\bar{c}_f^1+\mathcal{O}(\zeta^2)\right)^2\left(\lambda_f^0+\lambda_f^1\zeta+\mathcal{O}(\zeta^2)\right)^2-12(\bar{s}_f^0-\bar{A}_1)(\bar{c}_f^0+\zeta\,\bar{c}_f^1+\mathcal{O}(\zeta^2))(\lambda_f^0+\lambda_f^1\zeta+\mathcal{O}(\zeta^2))\\&+(3\delta+10)\bar{B}_1\zeta=0,\\ \Leftrightarrow&(12\delta(\bar{c}_f^0\lambda_f^0)^2-12(\bar{B}_0+\bar{B}_1-\bar{A}_1)\bar{c}_f^0\lambda_f^0)\\&+\zeta(24\delta(\bar{c}_f^0)^2\lambda_f^0\lambda_f^1+24\delta\bar{c}_f^0\bar{c}_f^1(\lambda_f^0)^2-12(\bar{B}_0+\bar{B}_1-\bar{A}_1)(\bar{c}_f^0\lambda_f^1+\bar{c}_f^1\lambda_f^0)+(3\delta+10)\bar{B}_1)=0,\end{aligned} \tag{D.13}$$

and

$$\begin{aligned}&2\delta\left(\lambda_f^0+\lambda_f^1\zeta+\mathcal{O}(\zeta^2)\right)^2-2\delta\left(\bar{c}_f^0+\zeta\,\bar{c}_f^1+\mathcal{O}(\zeta^2)\right)^2\left(\lambda_f^0+\lambda_f^1\zeta+\mathcal{O}(\zeta^2)\right)^2\\&-\delta(\bar{c}_f^0+\zeta\,\bar{c}_f^1+\mathcal{O}(\zeta^2))(\lambda_f^0+\lambda_f^1\zeta+\mathcal{O}(\zeta^2))-(\delta-1)\bar{s}_f^0-\delta\bar{A}_0-\bar{A}_1=0,\\ \Leftrightarrow&(2\delta(\lambda_f^0)^2-2\delta(\bar{c}_f^0\lambda_f^0)^2-\delta\bar{c}_f^0\lambda_f^0-(\delta-1)\bar{s}_f^0-\delta\bar{A}_0-\bar{A}_1)\\&+\zeta\delta(-4\bar{c}_f^0\bar{c}_f^1(\lambda_f^0)^2+4\lambda_f^0\lambda_f^1-4\lambda_f^0\lambda_f^1(\bar{c}_f^0)^2-\bar{c}_f^0\lambda_f^1-\bar{c}_f^1\lambda_f^0)=0.\end{aligned} \tag{D.14}$$

By combining Eqs. (D.13) and (D.14), we obtain (see Eq. (26))

$$\bar{c}_f=\bar{c}_f^0+(3\delta+10)\,\bar{B}_1\left(\lambda_f^0\right)^{-2}\Theta_f\,\Phi_f^{-1}\,\zeta+\mathcal{O}(\zeta^2). \tag{D.15}$$

where $\Theta_f = 4\left(\bar{c}_f^0\right)^2\lambda_f^0+\bar{c}_f^0-4\lambda_f^0$ and $\Phi_f = 48(\delta\,\bar{c}_f^0\lambda_f^0-\bar{s}_f^0+\bar{A}_1)$.

Appendix E. Asymptotic multiscale theory

First, we perform a first-order expansion of the forward wave speed $\bar{c}_b$, displacement $\bar{u}_b(z)=\bar{u}(\bar{x},\bar{t})$ and active stiffness $\bar{s}_b(z)=\bar{s}(\bar{x},\bar{t})$ with respect to the small parameter ζ in the backward traveling-wave coordinate, as follows

$$\begin{cases}\bar{u}_b(z)=\bar{u}_b^0(z)+\bar{u}_b^1(z)\zeta+\mathcal{O}(\zeta^2), & z\sim\mathcal{O}((\lambda_b^0)^{-1}),\\ \bar{s}_b(z)=\bar{s}_b^0(z)+\bar{s}_b^1(z)\zeta+\mathcal{O}(\zeta^2), & z\sim\mathcal{O}((\lambda_b^0)^{-1}),\\ |\bar{c}_b|=|\bar{c}_b^0|+|\bar{c}_b^1|\zeta+\mathcal{O}(\zeta^2),\end{cases} \tag{E.1}$$

where the backward traveling-wave coordinate (see Eq. (16)) is defined as $z=-\bar{x}+|\bar{c}_b|\bar{t}$, $\bar{c}_b<0$. Note that the initial condition for the backward wave is given by

$$\bar{u}_b(\mp\infty)=\pm1,\qquad \bar{s}_b(-\infty)=\bar{s}_b^0=\bar{B}_0-\bar{B}_1. \tag{E.2}$$

which arises from the use of the original spatial coordinate that endows the system with time-reversal characteristics. Similarly, by substituting the backward traveling-wave coordinate into the dimensionless continuum model (see Eqs. (14) and (15)), we obtain (see Eqs. (27) and (28))

$$\begin{cases}(\bar{c}_b^2-1)\bar{u}_b''+|\bar{c}_b|\bar{u}_b'+(\bar{u}_b^2-1)((\bar{s}_b+\bar{A}_0)\bar{u}_b+(\bar{s}_b-\bar{A}_1)\delta^{-1})=0,\\ |\bar{c}_b|\bar{s}_b'-\zeta(\bar{B}_0-\bar{B}_1\bar{u}_b-\bar{s}_b)=0,\end{cases} \tag{E.3}$$

Next, we sequentially solve each term in the asymptotic expansion. By setting $\zeta=0$ and substituting Eq. (E.1) into Eq. (E.3), we obtain an equation that admits an analytical solution for $\bar{u}_b^0(z)=-\tanh(\lambda_b^0 z)$, $\lambda_b^0=\left(\frac{1}{2}(\bar{A}_0+\bar{s}_b^0)+\left(\bar{A}_1-\bar{s}_b^0\right)^2\delta^{-2}\right)^{1/2}$ (see Eq. (29)), which can be expressed as follows

$$\begin{cases} ((\bar{c}_b^0)^2-1)(\bar{u}_b^0)''+|\bar{c}_b^0|(\bar{u}_b^0)'+((\bar{u}_b^0)^2-1)((\bar{s}_b^0+\bar{A}_0)\bar{u}_b^0+(\bar{s}_b^0-\bar{A}_1)\delta^{-1})=0,\\ \bar{s}_b^0=\bar{s}_b(-\infty)=\bar{B}_0-\bar{B}_1, \end{cases}$$
$$\Leftrightarrow((\bar{c}_b^0)^2-1)(\bar{u}_b^0)''+|\bar{c}_b^0|(\bar{u}_b^0)'+((\bar{u}_b^0)^2-1)((\bar{B}_0-\bar{B}_1+\bar{A}_0)\bar{u}_b^0+(\bar{B}_0-\bar{B}_1-\bar{A}_1)\delta^{-1})=0, \tag{E.4}$$

from which we can also obtain a key solution corresponding to the asymptotic expansion (see Eq. (30)) of the backward wave speed as follows

$$|\bar{c}_b^0|=\left(1+\tfrac{1}{2}\delta^2(\bar{A}_0+\bar{s}_b^0)\left(\bar{A}_1-\bar{s}_b^0\right)^{-2}\right)^{-1/2}. \tag{E.5}$$

To solve the remaining terms in the expansion, we further expand the reciprocal of the wave speed and substitute it into the second equation of Eq. (E.3), yielding

$$\begin{cases} \bar{s}_b'-\zeta|\bar{c}_b|^{-1}(\bar{B}_0-\bar{B}_1\bar{u}_b-\bar{s}_b)=0,\\ |\bar{c}_b|^{-1}=|\bar{c}_b^0|^{-1}-|\bar{c}_b^1|(\bar{c}_b^0)^{-2}\zeta+\mathcal{O}(\zeta^2), \end{cases}$$
$$\Rightarrow\bar{s}_b'-\zeta(|\bar{c}_b^0|^{-1}-|\bar{c}_b^1|(\bar{c}_b^0)^{-2}\zeta+\mathcal{O}(\zeta^2))(\bar{B}_0-\bar{B}_1\bar{u}_b-\bar{s}_b)=0. \tag{E.6}$$

Substituting Eq. (E.1) into Eq. (E.6) and simplifying, we obtain

$$\begin{cases} \bar{u}_b(z)=\bar{u}_b^0(z)+\bar{u}_b^1(z)\zeta+\mathcal{O}(\zeta^2),\\ \bar{s}_b(z)=\bar{s}_b^0(z)+\bar{s}_b^1(z)\zeta+\mathcal{O}(\zeta^2),\\ \bar{s}_b'-\zeta(|\bar{c}_b^0|^{-1}-|\bar{c}_b^1|(\bar{c}_b^0)^{-2}\zeta+\mathcal{O}(\zeta^2))(\bar{B}_0-\bar{B}_1\bar{u}_b-\bar{s}_b)=0 \end{cases}$$
$$\Rightarrow(\bar{s}_b^0)'+\zeta((\bar{s}_b^1)'-|\bar{c}_b^0|^{-1}(\bar{B}_0-\bar{B}_1\bar{u}_b^0-\bar{s}_b^0))+\mathcal{O}(\zeta^2)=0, \tag{E.7}$$

from which we obtain the following system of equations (see Eq. (31))

$$(\bar{s}_b^0)'=0,\qquad (\bar{s}_b^1)'-|\bar{c}_b^0|^{-1}(\bar{B}_0-\bar{B}_1\bar{u}_b^0-\bar{s}_b^0)=0,$$
$$\Rightarrow\bar{s}_b^0=\bar{s}_b(-\infty)=\bar{B}_0-\bar{B}_1,\qquad \bar{s}_b^1(z)=\bar{B}_1(|\bar{c}_b^0|\lambda_b^0)^{-1}(\ln(\cosh(\lambda_b^0 z))+\lambda_b^0 z+\ln 2). \tag{E.8}$$

Appendix F. Singular perturbation method

In the preceding analysis, we have demonstrated the integral condition and far-field relations satisfied by the active bistable lattice, which indicates that the backward-wave dynamics model is applicable to singular perturbation theory. Therefore, we introduce a two-parameter expansion with respect to $0<\zeta\ll 1$ as follows

$$\lambda_b=\lambda_b^0+\lambda_b^1\zeta+\mathcal{O}(\zeta^2),\qquad |\bar{c}_b|=|\bar{c}_b^0|+|\bar{c}_b^1|\zeta+\mathcal{O}(\zeta^2). \tag{F.1}$$

We first derive the far-field relations for the backward-wave system.

$$\bar{u}_b(z)=-\tanh(\lambda_b z)=(1-\exp(2\lambda_b z))/(1+\exp(2\lambda_b z))$$
$$=1-2\exp(2\lambda_b z)+\mathcal{O}(\exp(4\lambda_b z))\approx 1-2\exp(2\lambda_b z),\quad |z|^{-1}\ll 1, \tag{F.2}$$

substituting Eq. (F.2) into Eq. (E.3) yields

$$\begin{cases} |\bar{c}_b|\bar{s}_b'-\zeta(\bar{B}_0-\bar{B}_1 1-2\exp(2\lambda_b z)-\bar{s}_b)=0,\ \Rightarrow\bar{s}_b=\bar{s}_b^0+2\bar{B}_1\zeta(2\bar{c}_b\lambda+\zeta)^{-1}\exp(2\lambda_b z),\\ (\bar{c}_b^2-1)\bar{u}_b''+|\bar{c}_b|\bar{u}_b'+(\bar{u}_b^2-1)((\bar{s}_b+\bar{A}_0)\bar{u}_b+(\bar{s}_b-\bar{A}_1)\delta^{-1})=0, \end{cases}$$
$$\Rightarrow 2\delta\lambda_b^2(1-(\bar{c}_b)^2)-\delta|\bar{c}_b|\lambda_b-(\delta+1)\bar{s}_b^0-(\delta\bar{A}_0-\bar{A}_1)=0. \tag{F.3}$$

Substituting the expansion (see Eq. (F.1)) into the first equation yields (see Eq. (F.3))

$$(2\delta(\lambda_b^0)^2-2\delta(\bar{c}_b^0\lambda_b^0)^2-\delta|\bar{c}_b^0|\lambda_b^0-(\delta+1)\bar{s}_b^0-\delta\bar{A}_0+\bar{A}_1)$$
$$+\zeta\delta(-4|\bar{c}_b^0\bar{c}_b^1|(\lambda_b^0)^2+4\lambda_b^0\lambda_b^1-4(\bar{c}_b^0)^2\lambda_b^0\lambda_b^1-|\bar{c}_b^0\lambda_b^1|-|\bar{c}_b^1|\lambda_b^0)=0.$$
$$\Leftrightarrow\begin{cases} 2\delta(\lambda_b^0)^2-2\delta(\bar{c}_b^0\lambda_b^0)^2-\delta|\bar{c}_b^0|\lambda_b^0-(\delta+1)\bar{s}_b^0-\delta\bar{A}_0+\bar{A}_1=0,\\ -4|\bar{c}_b^0\bar{c}_b^1|(\lambda_b^0)^2+4\lambda_b^0\lambda_b^1-4(\bar{c}_b^0)^2\lambda_b^0\lambda_b^1-|\bar{c}_b^0\lambda_b^1|-|\bar{c}_b^1|\lambda_b^0=0. \end{cases} \tag{F.4}$$

Next, we derive the integral condition (according to Eq. (E.3)) for the backward-wave system to obtain the second equation of the singular perturbation problem.

$$\begin{cases} (\bar{c}_b^2-1)\int_{-\infty}^{\infty}\bar{u}_b''\bar{u}_b'\mathrm{d}z-\int_{-\infty}^{\infty}|\bar{c}_b|\left(\bar{u}_b'\right)^2\mathrm{d}z+\int_{-\infty}^{\infty}(\bar{u}_b^2-1)((\bar{s}_b+\bar{A}_0)\,\bar{u}_b+(\bar{s}_b-\bar{A}_1)\delta^{-1})\bar{u}_b'\mathrm{d}z=0,\\ \int_{-\infty}^{\infty}\bar{u}_b''\bar{u}_b'\mathrm{d}z=\tfrac{1}{2}(\bar{u}_b')^2\,|_{-\infty}^{\infty}=0,\\ \int_{-\infty}^{\infty}((\bar{u}_b)^2-1)(\bar{A}_0\bar{u}_b-\bar{A}_1\delta^{-1})\bar{u}_b'\mathrm{d}z=-\bar{A}_1\delta^{-1}\int_{-\infty}^{\infty}((\bar{u}_b)^2-1)\bar{u}_b'\mathrm{d}z. \end{cases} \tag{F.5}$$

It follows from Eq. (E.5) that

$$\begin{cases} \int_{-\infty}^{\infty}\bar{s}_b((\bar{u}_b)^2-1)(\bar{u}_b+\delta^{-1})\bar{u}_b'\mathrm{d}z=\bar{A}_1\delta^{-1}\int_{-\infty}^{\infty}\left((\bar{u}_b)^2-1\right)\bar{u}_b'\mathrm{d}z-\bar{c}_b\int_{-\infty}^{\infty}\left(\bar{u}_b'\right)^2\mathrm{d}z,\\ \bar{u}_b(z)\approx-\tanh(\lambda_b z), \end{cases}$$
$$\Rightarrow 12\delta\left(|\bar{c}_b|\lambda_b\right)^2=12(\bar{A}_1-\bar{s}_b^0)|\bar{c}_b|\lambda_b+(3\delta-10)\bar{B}_1\zeta, \tag{F.6}$$

Substituting Eq. (F.1) into the second equation (see Eq. (F.6)) yields

$$\begin{aligned}&(12\delta(\bar{c}_b^0\lambda_b^0)^2-12(\bar{A}_1+\bar{B}_1-\bar{B}_0)|\bar{c}_b^0|\lambda_b^0)\\&+\zeta(24\delta(\bar{c}_b^0)^2\lambda_b^0\lambda_b^1+24\delta|\bar{c}_b^0\bar{c}_b^1|(\lambda_b^0)^2-12(\bar{A}_1+\bar{B}_1-\bar{B}_0)(|\bar{c}_b^0|\lambda_b^1+|\bar{c}_b^1|\lambda_b^0)-(3\delta-10)\bar{B}_1)=0,\\&\Leftrightarrow\begin{cases}\delta(\bar{c}_b^0\lambda_b^0)^2-(\bar{A}_1+\bar{B}_1-\bar{B}_0)|\bar{c}_b^0|\lambda_b^0=0,\\24\delta(\bar{c}_b^0)^2\lambda_b^0\lambda_b^1+24\delta|\bar{c}_b^0\bar{c}_b^1|(\lambda_b^0)^2-12(\bar{A}_1+\bar{B}_1-\bar{B}_0)(|\bar{c}_b^0|\lambda_b^1+|\bar{c}_b^1|\lambda_b^0)-(3\delta-10)\bar{B}_1=0.\end{cases}\end{aligned}\tag{F.7}$$

By combining Eq. (F.4) and Eq. (F.7) as follows

$$\begin{cases}2\delta(\lambda_b^0)^2-2\delta(\bar{c}_b^0\lambda_b^0)^2-\delta|\bar{c}_b^0|\lambda_b^0-(\delta+1)\bar{s}_b^0-\delta\bar{A}_0+\bar{A}_1=0,\ \delta(\bar{c}_b^0\lambda_b^0)^2-(\bar{A}_1+\bar{B}_1-\bar{B}_0)|\bar{c}_b^0|\lambda_b^0=0,\\-4|\bar{c}_b^0\bar{c}_b^1|(\lambda_b^0)^2+4\lambda_b^0\lambda_b^1-4(\bar{c}_b^0)^2\lambda_b^0\lambda_b^1-|\bar{c}_b^0\lambda_b^1|-|\bar{c}_b^1|\lambda_b^0=0,\\24\delta(\bar{c}_b^0)^2\lambda_b^0\lambda_b^1+24\delta|\bar{c}_b^0\bar{c}_b^1|(\lambda_b^0)^2-12(\bar{A}_1+\bar{B}_1-\bar{B}_0)(|\bar{c}_b^0|\lambda_b^1+|\bar{c}_b^1|\lambda_b^0)-(3\delta-10)\bar{B}_1=0,\end{cases}\tag{F.8}$$

we finally obtain the expression of the backward-wave speed (see Eq. (32)):

$$\bar{c}_b=-|\bar{c}_b^0|-(3\delta-10)\bar{B}_1\left(\lambda_b^0\right)^{-2}\Theta_b\,\Phi_b^{-1}\,\zeta+\mathcal{O}(\zeta^2),\tag{F.9}$$

where $\Theta_b=4\lambda_b^0-4\left(\bar{c}_b^0\right)^2\lambda_b^0-|\bar{c}_b^0|$ and $\Phi_b=48\,(2\delta|\bar{c}_b^0|\lambda_b^0-\bar{A}_1+\bar{s}_b^0)$.

Appendix G. Numerical solution for the first-order term

According to the asymptotic expansion method, we consider the following system of equations (see Eqs. (19) and Eq. (17))

$$\begin{cases}\bar{u}_f''-\bar{c}_f\left(\bar{c}_f^2-1\right)^{-1}\bar{u}_f'+(\bar{c}_f^2-1)^{-1}(\bar{u}_f^2-1)\left((\bar{s}_f+\bar{A}_0)\bar{u}_f+(\bar{s}_f-\bar{A}_1)\delta^{-1}\right)=0,\\\bar{u}_f=\bar{u}_f^0+\zeta\,\bar{u}_f^1+\mathcal{O}(\zeta^2),\quad\bar{s}_f=\bar{s}_f^0+\zeta\,\bar{s}_f^1+\mathcal{O}(\zeta^2),\quad\bar{c}_f=\bar{c}_f^0+\zeta\,\bar{c}_f^1+\mathcal{O}(\zeta^2),\end{cases}\tag{G.1}$$

To solve for $\bar{u}_f^1$ and $\bar{s}_f^1$, we simplify Eq. (G.1) as follows

$$\begin{aligned}&(\bar{u}_f^0)''+\bar{c}_f^0(1-(\bar{c}_f^0t)^2)^{-1}(\bar{u}_f^0)'-(1-(\bar{c}_f^0)^2)^{-1}((\bar{u}_f^0)^2-1)((\bar{s}_f^0+\bar{A}_0)\bar{u}_f^0+(\bar{s}_f^0-\bar{A}_1)\delta^{-1})\\&-\zeta(1-(\bar{c}_f^0)^2)^{-1}((\bar{u}_f^0)^2-1)(\bar{u}_f^0+\delta^{-1})\bar{s}_f^1+\zeta((\bar{u}_f^1)''+\bar{c}_f^0(1-(\bar{c}_f^0)^2)^{-1}(\bar{u}_f^1)')\\&-(1-(\bar{c}_f^0)^2)^{-1}\zeta(2\bar{u}_f^0((\bar{s}_f^0+\bar{A}_0)\bar{u}_f^0+(\bar{s}_f^0-\bar{A}_1)\delta^{-1})\bar{u}_f^1+((\bar{u}_f^0)^2-1)(\bar{s}_f^0+\bar{A}_0))\\&+\zeta(\bar{u}_f^0)'(\bar{c}_f^1(1-(\bar{c}_f^0)^2)^{-1}+2(\bar{c}_f^0)^2\bar{c}_f^1(1-(\bar{c}_f^0)^2)^{-2})\\&-2\zeta\bar{c}_f^0\bar{c}_f^1(1-(\bar{c}_f^0)^2)^{-2}((\bar{u}_f^0)^2-1)((\bar{s}_f^0+\bar{A}_0)\bar{u}_f^0+(\bar{s}_f^0-\bar{A}_1)\delta^{-1})+\mathcal{O}(\zeta^2)=0.\end{aligned}\tag{G.2}$$

Similarly, for the backward wave (see Eq. (27)), we also have the following

$$\begin{aligned}&\begin{cases}(\bar{c}_b^2-1)\bar{u}_b''+|\bar{c}_b|\bar{u}_b'+(\bar{u}_b^2-1)((\bar{s}_b+\bar{A}_0)\bar{u}_b+(\bar{s}_b-\bar{A}_1)\delta^{-1})=0,\\\bar{u}_b=\bar{u}_b^0+\bar{u}_b^1\zeta+\mathcal{O}(\zeta^2),\quad\bar{s}_b=\bar{s}_b^0+\bar{s}_b^1\zeta+\mathcal{O}(\zeta^2),\quad|\bar{c}_b|=|\bar{c}_b^0|+|\bar{c}_b^1|\zeta+\mathcal{O}(\zeta^2),\end{cases}\\&\Rightarrow(1-(\bar{c}_b^0)^2)(\bar{u}_b^0)''-|\bar{c}_b^0|(\bar{u}_b^0)'-((\bar{u}_b^0)^2-1)((\bar{s}_b^0+\bar{A}_0)\bar{u}_b^0+(\bar{s}_b^0-\bar{A}_1)\delta^{-1})\\&-((\bar{u}_b^0)^2-1)(\bar{u}_b^0+\delta^{-1})\zeta\bar{s}_b^1+\zeta(1-(\bar{c}_b^0)^2)(\bar{u}_b^1)''-\zeta|\bar{c}_b^0|(\bar{u}_b^1)'\\&-\zeta\bar{u}_b^1(2\bar{u}_b^0((\bar{s}_b^0+\bar{A}_0)\bar{u}_b^0+(\bar{s}_b^0-\bar{A}_1)\delta^{-1})+((\bar{u}_b^0)^2-1)(\bar{s}_b^0+\bar{A}_0))\\&-(|\bar{c}_b^1|+2(\bar{c}_b^0)^2|\bar{c}_b^1|(1-(\bar{c}_b^0)^2)^{-1})\zeta(\bar{u}_b^0)'\\&-2\zeta|\bar{c}_b^0\bar{c}_b^1|(1-(\bar{c}_b^0)^2)^{-1}((\bar{u}_b^0)^2-1)((\bar{s}_b^0+\bar{A}_0)\bar{u}_b^0+(\bar{s}_b^0-\bar{A}_1)\delta^{-1})+\mathcal{O}(\zeta^2)=0.\end{aligned}\tag{G.3}$$

Since the zeroth-order terms are known, we find that Eqs. (G.2) and (G.3) actually represent the following two boundary value problems

$$(\bar{u}_f^1)''+h_f(z)(\bar{u}_f^1)'+l_f(z)\bar{u}_f^1+p_f(z)\bar{c}_f^1+q_f(z)=0,\quad\lim_{z\to\pm\infty}\bar{u}_f^1=0,\tag{G.4}$$

and

$$(\bar{u}_b^1)''+h_b(z)(\bar{u}_b^1)'+l_b(z)\bar{u}_b^1+p_b(z)|\bar{c}_b^1|+q_b(z)=0,\quad\lim_{z\to\mp\infty}\bar{u}_b^1=0.\tag{G.5}$$

where

$$\begin{aligned}h_f=&\bar{c}_f^0(1-(\bar{c}_f^0)^2)^{-1},\ q_f=-(1-(\bar{c}_f^0)^2)^{-1}((\bar{u}_f^0)^2-1)(\bar{u}_f^0+\delta^{-1})\bar{s}_f^1,\\l_f=&-(1-(\bar{c}_f^0)^2)^{-1}(2\bar{u}_f^0((\bar{s}_f^0+\bar{A}_0)\bar{u}_f^0+(\bar{s}_f^0-\bar{A}_1)\delta^{-1})+((\bar{u}_f^0)^2-1)(\bar{s}_f^0+\bar{A}_0)),\\p_f=&(\bar{u}_f^0)'(1-(\bar{c}_f^0)^2)^{-1}\\&+2\bar{c}_f^0(1-(\bar{c}_f^0)^2)^{-2}((\bar{u}_f^0)'\bar{c}_f^0-((\bar{u}_f^0)^2-1)((\bar{s}_f^0+\bar{A}_0)\bar{u}_f^0+(\bar{s}_f^0-\bar{A}_1)\delta^{-1})).\end{aligned}\tag{G.6}$$

and

$$\begin{aligned} h_b &= -|\bar{c}_b^0|(1-(\bar{c}_b^0)^2)^{-1}, \ q_b = -(1-(\bar{c}_b^0)^2)^{-1}((\bar{u}_b^0)^2-1)(\bar{u}_b^0+\delta^{-1})\bar{s}_b^1, \\ l_b &= -(1-(\bar{c}_b^0)^2)^{-1}(2\bar{u}_b^0((\bar{s}_b^0+\bar{A}_0)\bar{u}_b^0+(\bar{s}_b^0-\bar{A}_1)\delta^{-1})+((\bar{u}_b^0)^2-1)(\bar{s}_b^0+\bar{A}_0)), \\ p_b &= -(1-(\bar{c}_b^0)^2)^{-1}(\bar{u}_b^0)' \\ &\quad -2|\bar{c}_b^0|(1-(\bar{c}_b^0)^2)^{-2}((\bar{u}_b^0)'|\bar{c}_b^0|+((\bar{u}_b^0)^2-1)((\bar{s}_b^0+\bar{A}_0)\bar{u}_b^0+(\bar{s}_b^0-\bar{A}_1)\delta^{-1})). \end{aligned} \tag{G.7}$$

For better tractability, the boundary value problems defined over an infinite domain are transformed into those on a finite domain, while maintaining the desired level of accuracy, as follows

$$(\bar{u}^1)'' + h(\bar{u}^1)' + l\bar{u}^1 + p\bar{c}^1 + q = 0, \qquad \bar{u}^1(z=\pm 10) = 0 \tag{G.8}$$

where we find that setting the nondimensional finite-domain length to 10 is sufficient to maintain the accuracy of the results. Note that $\bar{u}^1$ represents both $\bar{u}_f^1$ and $\bar{u}_b^1$.

Next, we employ the central difference method to perform the discretization. First, the domain is divided into uniformly spaced subintervals with a width of d, and the boundary of each subinterval is denoted by $n = 0, 1, 2, \dots, N'$. The central difference scheme is then applied as follows

$$(\bar{u}^1)'' \approx (\bar{u}_{n-1}^1 - 2\bar{u}_n^1 + \bar{u}_{n+1}^1)/d^2, \qquad (\bar{u}^1)' = (\bar{u}_{n+1}^1 - \bar{u}_{n-1}^1)/2d. \tag{G.9}$$

Substituting Eq. (G.9) into Eq. (G.8) yields

$$\begin{aligned} &(\bar{u}_{n-1}^1 - 2\bar{u}_n^1 + \bar{u}_{n+1}^1)d^{-2} + \frac{h}{2}(\bar{u}_{n+1}^1 - \bar{u}_{n-1}^1)d^{-1} + l\bar{u}^1 + p\bar{c}^1 + q = 0, \\ \Leftrightarrow &(d^{-2} + \frac{1}{2}hd^{-1})\bar{u}_{n+1}^1 + (-2d^{-2}+l)\bar{u}_n^1 + (d^{-2} - \frac{1}{2}hd^{-1})\bar{u}_{n-1}^1 + p\bar{c}^1 + q = 0, \\ \Leftrightarrow &(d^{-2} + \frac{1}{2}hd^{-1})\bar{u}_{n+1}^1 + (-2d^{-2}+l)\bar{u}_n^1 + (d^{-2} - \frac{1}{2}hd^{-1})\bar{u}_{n-1}^1 + p\bar{c}^1 = -q, \end{aligned} \tag{G.10}$$

where $\bar{u}_n^1 = \bar{u}^1(nd),\ 1 \le n \le N'-1$. Thus, Eq. (G.10) is equivalent to the following underdetermined matrix system

$$AU = B, \quad U = \left[\bar{u}_1^1, \dots, \bar{u}_{N'-1}^1, \bar{c}^1\right]^T, \ A \in \mathbb{R}^{(N'-1)\times N'}, \ B = \left[-\bar{q}_1, -\bar{q}_2 \dots, -\bar{q}_{N'-1}\right]^T \tag{G.11}$$

We solve the above underdetermined system using our in-house Python code, which computes the Moore-Penrose pseudoinverse based on singular value decomposition and yields the solution with the minimum norm among all possible solutions. We find that, in the normalized null space, the component associated with the free parameter $\bar{c}^1$ is merely $\mathcal{O}(10^{-5})$, indicating that the influence of this free parameter on the solution is negligible. Consequently, all solutions of the system corresponding to small $\bar{u}^1$ values have very similar $\bar{c}^1$ values. This suggests that, in our system, fluctuations in $\bar{c}^1$ have little effect on the nonreciprocity associated with the wave speed.

Appendix H. Backward wave initiation

In Fig. H.1, we show the critical initiation times of the returning wave under different energy injection rates $\xi = 0.005$ s^{-1}, 0.01 s^{-1}, 0.02 s^{-1} and 0.04 s^{-1} , beyond which the backward wave can be successfully initiated and propagated (see Movie 4). It can be observed that as ξ increases from 0.005 to 0.04 s^{-1}, the forward wave speed gradually decreases, i.e., the time for the forward wave to reach the end of the bistable lattice increases from 484.4 to 562.25 s. The critical initiation time 599 s in Fig. H.1(d) is later than that 587s in Fig. H.1(c) because of the delayed arrival of the forward wave. But the difference between the forward wave arrival time and the backward wave critical initiation time decreases from 313.6 to 36.75 s, which follows the expected trend. The origin of this anomalous behavior lies in the intermediate phase of $s_i(t)$, which is clearly observed in Fig. H.1. As ξ decreases from 0.005 to 0.04 s^{-1}, the range of the intermediate phase of $s_i(t)$ becomes smaller, which weakens the delayed effect on the critical initiation time of the backward wave. The same intermediate state can be observed in Fig. C.1. These observations collectively demonstrate that the proposed two-variable coupled dynamical model of active bistable lattices accurately and effectively captures the slow recovery variable, with the synchronized recovery of the slow variables illustrated in Movie 4.

It should be noted that the machine-learning approach was chosen instead of conventional numerical methods for the following reason. Although conventional numerical methods are well established and can solve the model for specific parameter sets, our model is a general two-variable coupled framework. Therefore, the relevant parameter combinations may vary across different application scenarios.

In this case, continuing to use conventional numerical methods would greatly increase the computational cost and would be far less efficient than the general solution model established by the machine-learning method. Therefore, once trained, the machine-learning model used in the manuscript provides substantially faster evaluations than conventional numerical methods. It is particularly useful for parameter sweeps, sensitivity analysis, nonreciprocal energy mapping, and inverse design.

In addition, the manuscript provides exact analytical solutions over most regions of interest. The machine-learning approach can incorporate these solutions and preserve their accuracy to the greatest extent possible. Further optimization based on this framework can yield solutions with improved accuracy.

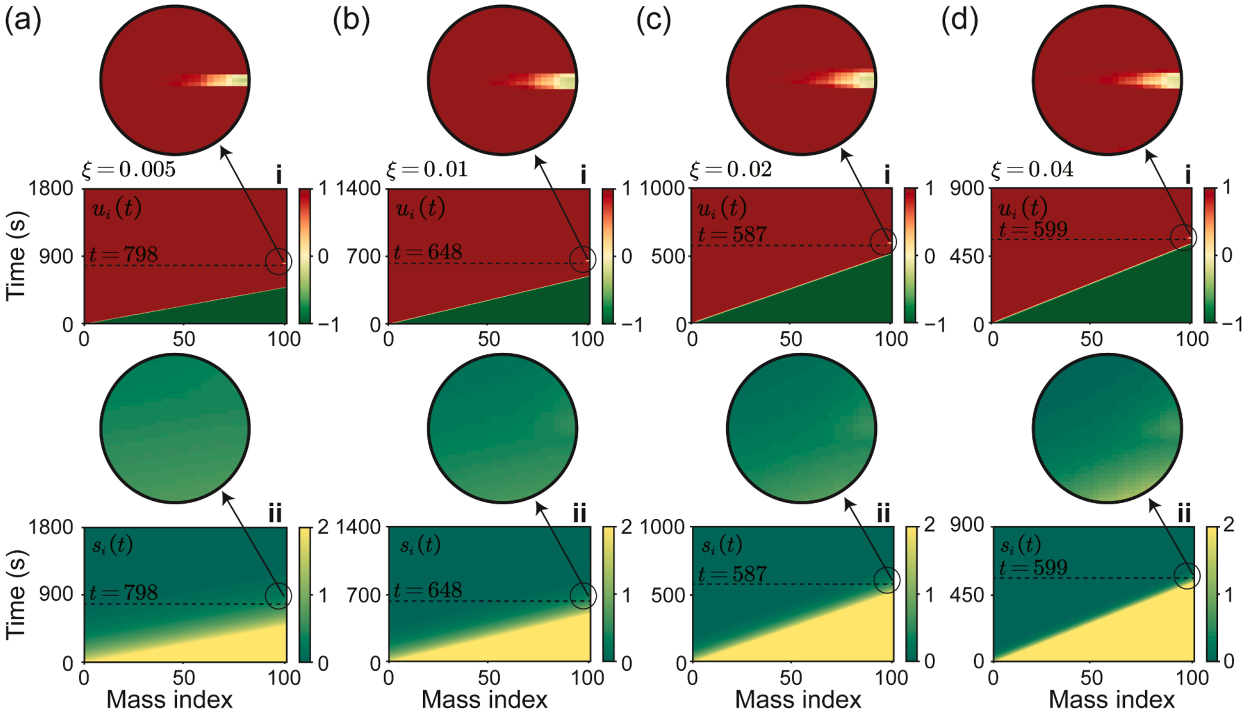

Fig. H.1. Spatiotemporal variations of $u_i(t)$ and $s_i(t)$ corresponding to different critical initiation times of the backward wave. (a) Spatiotemporal variations of $u_i(t)$ and $s_i(t)$ for the critical initiation time of 798 s ($\xi = 0.005$ s^{-1}). (b) Spatiotemporal variations of $u_i(t)$ and $s_i(t)$ for the critical initiation time of 648 s ($\xi = 0.01$ s^{-1}). (c) Spatiotemporal variations of $u_i(t)$ and $s_i(t)$ for the critical initiation time of 587 s ($\xi = 0.02$ s^{-1}). (d) Spatiotemporal variations of $u_i(t)$ and $s_i(t)$ for a critical initiation time of 599 s ($\xi = 0.04$ s^{-1}). The parameters: $A_n = B_n = 1$ g $\cdot$ m^{-2} $\cdot$ s^{-2} ($n = 0, 1$), and $\delta = 2$.

Appendix I. Machine learning algorithm

To accurately reconstruct the full traveling-wave profile of the slow recovery variable $\bar{s}(z)$, four representative machine learning algorithms are employed to correct the residual between the first-order asymptotic solution and the direct numerical simulation in the outer recovery region. The implementation for forward and backward waves follows the same algorithmic structure, with the following key distinctions.

Forward waves: The training interval is chosen in the left-hand outer region of the traveling coordinate. An anchor point located at the inner-layer boundary, where the residual is prescribed to vanish, is added to the training set to enforce smooth matching between the inner and outer solutions.

Backward waves: The training interval is chosen in the right-hand outer region of the traveling coordinate. In the same way, an anchor point at the inner-outer interface with vanishing residual is included to guarantee continuity across the interface. The backward-wave profile is then reconstructed by combining its leading-order asymptotic approximation with the first-order correction obtained from the singular-perturbation analysis.

The four algorithms are implemented as follows.

Polynomial regression expands the input coordinate z into monomials up to degree 5 using PolynomialFeatures, and fits the coefficients via ordinary least squares (LinearRegression). This yields a simple, interpretable correction that captures smooth trends but may lack flexibility for sharper variations.

Neural-network regression is built with a fully connected architecture (input layer, three hidden layers with 64 neurons and tanh activation, and an output layer) using TensorFlow and Keras. The network is trained for 10^4 epochs with the Adam optimizer (learning rate 10^{-5}) on standardized residuals. The trained model is saved and reused to avoid retraining, providing a flexible nonlinear approximator that can capture complex residual patterns.

Support-vector regression (SVR) with a radial-basis-function kernel ($C = 50$, $\gamma = 0.05$, $\varepsilon = 10^{-3}$) is applied to the augmented training set that includes the anchor point at $z = 0$ with $r(0) = 0$. In this case, the anchor is assigned a sample weight 10^3 times larger than the other points to enforce the matching condition at the inner-layer boundary. This kernel-based approach offers strong generalization while explicitly imposing the asymptotic constraint.

Random-forest regression uses an ensemble of 200 decision trees with maximum depth 10 (RandomForestRegressor with the random state fixed at 42). By averaging over many trees grown on bootstrap samples, the method reduces variance and robustly handles local fluctuations without overfitting.

For both forward and backward waves, the performance of the algorithms is evaluated by the mean-squared error (MSE) over their respective training intervals. Among the four candidates, random-forest regression consistently achieves the lowest MSE while maintaining smooth and physically plausible waveforms, and is therefore adopted as the preferred surrogate for completing the outer-region profile within the hybrid asymptotic-data-driven framework described in Section 5.

References

Angeli, D., Ferrell Jr, J.E., Sontag, E.D., 2004. Detection of multistability, bifurcations, and hysteresis in a large class of biological positive-feedback systems. Proc. Natl. Acad. Sci. 101 (7), 1822–1827.

Beck, M., Jones, C.K., Schaeffer, D., Wechselberger, M., 2008. Electrical waves in a one-dimensional model of cardiac tissue. SIAM J. Appl. Dyn. Syst. 7 (4), 1558–1581.

Bernitt, E., Döbereiner, H.-G., Gov, N.S., Yochelis, A., 2017. Fronts and waves of actin polymerization in a bistability-based mechanism of circular dorsal ruffles. Nat. Commun. 8 (1), 15863.

Binysh, J., Wilks, T.R., Souslov, A., 2022. Active elastocapillarity in soft solids with negative surface tension. Sci. Adv. 8 (10), eabk3079.

Buonfiglio, V., Pertici, I., Marcello, M., Morotti, I., Caremani, M., Reconditi, M., Linari, M., Fanelli, D., Lombardi, V., Bianco, P., 2024. Force and kinetics of fast and slow muscle myosin determined with a synthetic sarcomere–like nanomachine. Commun. Biol. 7 (1), 361.

Caruel, M., Allain, J.-M., Truskinovsky, L., 2015. Mechanics of collective unfolding. J. Mech. Phys. Solids 76, 237–259.

Caruel, M., Truskinovsky, L., 2017. Bi-stability resistant to fluctuations. J. Mech. Phys. Solids 109, 117–141.

Choi, W.-Y., Kim, W., Choi, J.-R., Yu, S.Y., Moon, S., Park, Y.-J., Cho, K.-J., 2025. A hyperelastic torque-reversal mechanism for soft joints with compression-responsive transient bistability. Sci. Robot. 10 (98), eado7696.

Comte, J.-C., Marquié, P., Remoissenet, M., 1999. Dissipative lattice model with exact traveling discrete kink-soliton solutions: discrete breather generation and reaction diffusion regime. Phys. Rev. E 60 (6), 7484.

Da Rocha, H.B., Bleyer, J., Turlier, H., 2022. A viscous active shell theory of the cell cortex. J. Mech. Phys. Solids 164, 104876.

Deng, B., Wang, P., Tournat, V., Bertoldi, K., 2020. Nonlinear transition waves in free-standing bistable chains. J. Mech. Phys. Solids 136, 103661.

Deng, Y., Zhao, X., Huang, Z., Li, Y., 2025. Phase transitions perception in nonreciprocal mechanical metamaterials through electromagnetic resonance. Sci. Adv. 11 (37), eady1211.

Fenwick, A.J., Wood, A.M., Tanner, B. C.W., 2021. The spatial distribution of thin filament activation influences force development and myosin activity in computational models of muscle contraction. Arch. Biochem. Biophys. 703, 108855.

FitzHugh, R., 1955. Mathematical models of threshold phenomena in the nerve membrane. Bull. Math. Biophys. 17 (4), 257–278.

FitzHugh, R., 1961. Impulses and physiological states in theoretical models of nerve membrane. Biophys. J. 1 (6), 445–466.

Gao, N., Ma, T., Wang, Y., Zhou, W., Wang, Y.-S., Chen, W., 2024. A brief review of solitary waves in nonlinear metamaterials. Mech. Res. Commun. 137, 104260.

Gerwien, A., Mayer, P., Dube, H., 2019. Green light powered molecular state motor enabling eight-shaped unidirectional rotation. Nat. Commun. 10 (1), 4449.

Givli, S., Bhattacharya, K., 2009. A coarse-grained model of the myofibril: overall dynamics and the evolution of sarcomere non-uniformities. J. Mech. Phys. Solids 57 (2), 221–243.

Göktepe, S., Menzel, A., Kuhl, E., 2014. The generalized hill model: a kinematic approach towards active muscle contraction. J. Mech. Phys. Solids 72, 20–39.

Greilich, A., Kopteva, N.E., Korenev, V.L., Haude, P.A., Bayer, M., 2025. Exploring nonlinear dynamics in periodically driven time crystal from synchronization to chaotic motion. Nat. Commun. 16 (1), 2936.

Jin, L., Khajehtourian, R., Mueller, J., Rafsanjani, A., Tournat, V., Bertoldi, K., Kochmann, D.M., 2020. Guided transition waves in multistable mechanical metamaterials. Proc. Natl. Acad. Sci. 117 (5), 2319–2325.

Kellaris, N., Gopaluni Venkata, V., Smith, G.M., Mitchell, S.K., Keplinger, C., 2018. Peano-HASEL actuators: muscle-mimetic, electrohydraulic transducers that linearly contract on activation. Sci. Robot. 3 (14), eaar3276.

Khajehtourian, R., Kochmann, D.M., 2021. A continuum description of substrate-free dissipative reconfigurable metamaterials. J. Mech. Phys. Solids 147, 104217.

Kulkarni, Y., 2023. Fluctuations of active membranes with nonlinear curvature elasticity. J. Mech. Phys. Solids 173, 105240.

Li, P.Q., Wang, Y.S., Wang, K.F., Wang, B.L., 2025a. An elastic-boundary-controlled framework for on-demand stability switching in bistable curved beam metamaterials. Int. J. Solids Struct. , 113542.

Li, Z., Wang, Y., Wang, Z., Kadapa, C., Hossain, M., Yao, X., Wang, J., 2025b. Coupled magneto-mechanical growth in hyperelastic materials: surface patterns modulation and shape control in bio-inspired structures. J. Mech. Phys. Solids 200, 106089.

Li, Z.-N., Wang, Y.-Z., Wang, Y.-S., 2018. Nonreciprocal phenomenon in nonlinear elastic wave metamaterials with continuous properties. Int. J. Solids Struct. 150, 125–134.

Li, Z.-N., Wang, Y.-Z., Wang, Y.-S., 2020. Tunable nonreciprocal transmission in nonlinear elastic wave metamaterial by initial stresses. Int. J. Solids Struct. 182, 218–235.

Liang, X., Fu, H., Crosby, A.J., 2022. Phase-transforming metamaterial with magnetic interactions. Proc. Natl. Acad. Sci. 119 (1), e2118161119.

Librandi, G., Tubaldi, E., Bertoldi, K., 2021. Programming nonreciprocity and reversibility in multistable mechanical metamaterials. Nat. Commun. 12 (1), 3454.

Liu, K., Tachi, T., Paulino, G.H., 2019. Invariant and smooth limit of discrete geometry folded from bistable origami leading to multistable metasurfaces. Nat. Commun. 10 (1), 4238.

Liu, M., Domino, L., de Dinechin, I.D., Taffetani, M., Vella, D., 2023. Snap-induced morphing: from a single bistable shell to the origin of shape bifurcation in interacting shells. J. Mech. Phys. Solids 170, 105116.

Lou, C., Lian, X., Deng, H., Liu, B., Duan, S., Zhao, Y., Gong, X., 2025. Stiffness reprogrammable magnetorheological metamaterials inspired by spine for multibit visual mechanical information processing. Sci. Adv. 11 (41), eady8430.

Nadkarni, N., Arrieta, A.F., Chong, C., Kochmann, D.M., Daraio, C., 2016a. Unidirectional transition waves in bistable lattices. Phys. Rev. Lett. 116 (24), 244501.

Nadkarni, N., Daraio, C., Abeyaratne, R., Kochmann, D.M., 2016b. Universal energy transport law for dissipative and diffusive phase transitions. Phys. Rev. B 93 (10), 104109.

Nadkarni, N., Daraio, C., Kochmann, D.M., 2014. Dynamics of periodic mechanical structures containing bistable elastic elements: from elastic to solitary wave propagation. Phys. Rev. E 90 (2), 023204.

Nassar, H., Yousefzadeh, B., Fleury, R., Ruzzene, M., Alù, A., Daraio, C., Norris, A.N., Huang, G., Haberman, M.R., 2020. Nonreciprocity in acoustic and elastic materials. Nat. Rev. Mater. 5 (9), 667–685.

Ni, C., Chen, D., Yin, Y., Wen, X., Chen, X., Yang, C., Chen, G., Sun, Z., Wen, J., Jiao, Y., et al., 2023. Shape memory polymer with programmable recovery onset. Nature 622 (7984), 748–753.

Ogneva, I.V., Lebedev, D.V., Shenkman, B.S., 2010. Transversal stiffness and young's modulus of single fibers from rat soleus muscle probed by atomic force microscopy. Biophys. J. 98 (3), 418–424.

Pal, A., Sitti, M., 2023. Programmable mechanical devices through magnetically tunable bistable elements. Proc. Natl. Acad. Sci. 120 (15), e2212489120.

Pierre, S., 2020. Stick–slip model for actin-driven cell protrusions, cell polarization, and crawling. Proc. Natl. Acad. Sci. 117 (40), 24670–24678.

Raney, J.R., Nadkarni, N., Daraio, C., Kochmann, D.M., Lewis, J.A., Bertoldi, K., 2016. Stable propagation of mechanical signals in soft media using stored elastic energy. Proc. Natl. Acad. Sci. 113 (35), 9722–9727.

Remoissenet, M., Peyrard, M., 1984. Soliton dynamics in new models with parametrized periodic double-well and asymmetric substrate potentials. Phys. Rev. B 29 (6), 3153.

Roh, S., Ha, Y., Abbott, N.L., 2025. Biphasic liquids with shape-shifting and bistable microdomains. Nature , 1–7.

Roller, Y., Geron, Y., Givli, S., 2024. A bistable chain on elastic foundation. J. Mech. Phys. Solids 193, 105873.

Rubin, J., Wechselberger, M., 2008. The selection of mixed-mode oscillations in a hodgkin-huxley model with multiple timescales. Chaos: Interdiscip. J. Nonlinear Sci. 18 (1).

Schaeffer, M., Ruzzene, M., 2015. Wave propagation in multistable magneto-elastic lattices. Int. J. Solids Struct. 56, 78–95.

Shaat, M., Park, H.S., 2023. Chiral nonreciprocal elasticity and mechanical activity. J. Mech. Phys. Solids 171, 105163.

Shan, L., Xue, Y., Chen, X., Wang, Y., Feng, Y., Dong, L., Wang, C., Zhang, P., Wang, F., Guo, L., et al., 2025. Mechanically compliant and impedance matching hydrogel bioelectronics for low-voltage peripheral neuromodulation. Adv. Mater. , e11014.

Shan, S., Kang, S.H., Raney, J.R., Wang, P., Fang, L., Candido, F., Lewis, J.A., Bertoldi, K., 2015. Multistable architected materials for trapping elastic strain energy. Adv. Mater. 27 (29), 4296–4301.

Shi, X., Li, Y., Shi, N., Ji, C., Hou, L., Shi, Y., Xu, J., Lan, Y., Wei, Q., Ma, G., et al., 2025. Phase transition driven tough hydrogel ionic thermoelectric cell with giant thermopower. Nat. Commun. 16 (1), 9002.

Silling, S.A., 2016. Solitary waves in a peridynamic elastic solid. J. Mech. Phys. Solids 96, 121–132.

Slepyan, L., Cherkaev, A., Cherkaev, E., 2005. Transition waves in bistable structures. II. analytical solution: wave speed and energy dissipation. J. Mech. Phys. Solids 53 (2), 407–436.

Song, T., McNamara, J.W., Ma, W., Landim-Vieira, M., Lee, K.H., Martin, L.A., Heiny, J.A., Lorenz, J.N., Craig, R., Pinto, J.R., et al., 2021. Fast skeletal myosin-binding protein-c regulates fast skeletal muscle contraction. Proc. Natl. Acad. Sci. 118 (17), e2003596118.

Song, Y., Huang, S., Bono, D., Sadowski, J.T., Ross, C.A., Beach, G. S.D., 2025. Néel domain walls with bistable chirality in a perpendicularly magnetized ferrimagnetic insulator. Nat. Commun. 16 (1), 5201.

Srivastava, V.K., Tamsir, M., 2012. Crank-nicolson semi implicit approach for numerical solutions of two-dimensional coupled nonlinear burgers' equations. Int. J. Appl. Mech. Eng. 17 (2), 571.

Sun, Z., Zhou, J., Pan, Y., Song, Z., Mao, H.-K., Ahuja, R., 2011. Pressure-induced reversible amorphization and an amorphous–amorphous transition in ge2sb2te5 phase-change memory material. Proc. Natl. Acad. Sci. 108 (26), 10410–10414.

Sun, Z.G., Zimmerberg, N., Kelly, P., Floyd, C., Papoian, G., Murrell, M., 2025. Feedback between f-actin organization and active stress governs criticality and energy localization in the cell cytoskeleton. Nat. Phys. , 1–13.

Tang, Z., Ma, T., Chen, H., Gao, Y., 2024. Evolution of static to dynamic mechanical behavior in topological nonreciprocal active metamaterials. J. Mech. Phys. Solids 193, 105865.

Tang, Z., Ma, T., Su, B., Xia, Q., Kang, P., Wu, B., 2025. Anomalous size effects with fixed criticality in bistable flexible mechanical metamaterials. J. Mech. Phys. Solids 204, 106296.

Terzic, I., Meereboer, N.L., Acuautla, M., Portale, G., Loos, K., 2019. Electroactive materials with tunable response based on block copolymer self-assembly. Nat. Commun. 10 (1), 601.

Tian, F., Gong, J.P., 2025. Nonlinearity tunes crack dynamics in soft materials. J. Mech. Phys. Solids 202, 106191.

Vasios, N., Deng, B., Gorissen, B., Bertoldi, K., 2021. Universally bistable shells with nonzero gaussian curvature for two-way transition waves. Nat. Commun. 12 (1), 695.

Veenstra, J., Gamayun, O., Guo, X., Sarvi, A., Meinersen, C.V., Coulais, C., 2024. Non-reciprocal topological solitons in active metamaterials. Nature 627 (8004), 528–533.

Wang, C., Guo, H., Liu, R., Deng, Z., Chen, Y., You, Z., 2024a. Reconfigurable origami-inspired multistable metamorphous structures. Sci. Adv. 10 (22), eadk8662.

Wang, J., Wang, G., Chen, H., Liu, Y., Wang, P., Yuan, D., Ma, X., Xu, X., Cheng, Z., Ji, B., et al., 2024b. Robo-matter towards reconfigurable multifunctional smart materials. Nat. Commun. 15 (1), 8853.

Wang, Y., Li, Z., Chen, X., Tan, Y., Wang, F., Du, Y., Zhang, Y., Su, Y., Xu, F., Wang, C., et al., 2024c. Electroactive differential growth and delayed instability in accelerated healing tissues. J. Mech. Phys. Solids 193, 105867.

Wang, Y., Liu, M., Sareh, P., Liu, J., Huang, W., 2025. Towards ultrastretchability, multimodal instability, and static nonreciprocity in kirigami metamaterials. Soft Sci. 5 (2), N–A.

Wang, Y., Wu, Q., Tian, Y., Huang, G., 2024d. Non-hermitian wave dynamics of odd plates: microstructure design and theoretical modelling. J. Mech. Phys. Solids 182, 105462.

Worrell, B.T., McBride, M.K., Lyon, G.B., Cox, L.M., Wang, C., Mavila, S., Lim, C.-H., Coley, H.M., Musgrave, C.B., Ding, Y., et al., 2018. Bistable and photoswitchable states of matter. Nat. Commun. 9 (1), 2804.

Wu, Q., Wang, S., Qian, H., Wang, Y., Huang, G., 2024. Understanding of topological mode and skin mode morphing in 1d and 2d non-hermitian resonance-based meta-lattices. J. Mech. Phys. Solids 193, 105907.

Xing, J., Sun, F., Lin, Y., Gong, Z., 2024. A chemo-mechanical model for growth and mechanosensing of focal adhesion. J. Mech. Phys. Solids 193, 105863.

Xiu, H., Fancher, R., Frankel, I., Ziemke, P., Fermen-Coker, M., Begley, M., Boechler, N., 2025. Minimizing finite viscosity enhances relative kinetic energy absorption in bistable mechanical metamaterials but only with sufficiently fine discretization: a nonlinear dynamical size effect. J. Mech. Phys. Solids 200, 106105.

Xu, Y., Zhang, F., Rothemund, P., Keplinger, C., Xu, Z., Li, J., Zheng, Q., Zhu, J., 2025. Soft reconfigurable logic gates with high-frequency electrical switching. Sci. Adv. 11 (32), eadx1509.

Yan, D., Pezzulla, M., Cruveiller, L., Abbasi, A., Reis, P.M., 2021. Magneto-active elastic shells with tunable buckling strength. Nat. Commun. 12 (1), 2831.

Yasuda, H., Miyazawa, Y., Charalampidis, E.G., Chong, C., Kevrekidis, P.G., Yang, J., 2019. Origami-based impact mitigation via rarefaction solitary wave creation. Sci. Adv. 5 (5), eaau2835.

Zareei, A., Deng, B., Bertoldi, K., 2020. Harnessing transition waves to realize deployable structures. Proc. Natl. Acad. Sci. 117 (8), 4015–4020.

Zhang, Q., Cherkasov, A.V., Xie, C., Arora, N., Rudykh, S., 2023. Nonlinear elastic vector solitons in hard-magnetic soft mechanical metamaterials. Int. J. Solids Struct. 280, 112396.

Zhang, Q., Rudykh, S., 2024. Propagation of solitary waves in origami-inspired metamaterials. J. Mech. Phys. Solids 187, 105626.

Zhang, Q., Rudykh, S., 2025. Topological state switches in hard-magnetic meta-structures. J. Mech. Phys. Solids 196, 106001.

Zhang, Y., Lin, L., Wang, Y., Wang, S., Tao, Q., Liu, H., Zhang, Q., Wang, C., 2025. Deep learning-driven ultra-stretchable kirigami metamaterials: towards surface texture modulation via buckling. Soft Matter .

Zhang, Y., Wang, Y., Chen, C.Q., 2019. Ordered deformation localization in cellular mechanical metamaterials. J. Mech. Phys. Solids 123, 28–40.

Zhang, Y., Wang, Y., Tao, Q., Liu, Y., Wang, C., 2024. Deep learning of buckling instability in geometrically symmetry-breaking kirigami. Int. J. Mech. Sci. 280, 109331.

Zheng, Z., Chen, X., Wang, Y., Wen, P., Duan, Q., Zhang, P., Shan, L., Ni, Z., Feng, Y., Xue, Y., et al., 2024. Self-growing hydrogel bioadhesives for chronic wound management. Adv. Mater. 36 (41), 2408538.

Zhou, C., Yang, D., Sensale, S., Sharma, P., Wang, D., Yu, L., Arya, G., Ke, Y., Wang, P., 2022. A bistable and reconfigurable molecular system with encodable bonds. Sci. Adv. 8 (46), eade3003.

Zhou, W., Wang, Y.-Z., 2023. Cooperative propagation and directional phase transition of topological solitons in multi-stable mechanical metamaterials. J. Mech. Phys. Solids 175, 105287.

Zhou, W., Wang, Y.-Z., 2024. Nonlinear soliton spiral induces coupled multimode dynamics in multi-stable dissipative metamaterials. J. Mech. Phys. Solids 193, 105920.

Ziv, R., Shmuel, G., 2020. Oscillating vector solitary waves in soft laminates. J. Mech. Phys. Solids 143, 104058.